SYSTEMS TECHNOLOGY, INC.

13766 SOUTH HAWTHORNE BOULEVARD • HAWTHORNE, CALIFORNIA 90250 • PHONE (213) 679-2281

BRANCH OFFICE
194 NASSAU STREET
PRINCETON, NEW JERSEY 08540
PHONE (609) 924-4228

Technical Report No. 1007-1

APPLICATION OF AN APPROACH AND LANDING SYSTEM MODEL TO THE SPACE SHUTTLE ORBITER VEHICLE

Walter A. Johnson
Richard J. DiMarco

February 1972

Contract No. NAS2-6275

National Aeronautics and Space Administration
Ames Research Center
Moffett Field, California

FOREWORD

The research reported here was performed under Contract NAS2-6275 between Systems Technology, Inc., Hawthorne, California, and the National Aeronautics and Space Administration. The NASA Project Monitor was Thomas E. Wempe. The STI Technical Director was Irving L. Ashkenas, and the Project Engineer was Walter A. Johnson.

SUMMARY

An analytic model and procedure are described which can be used to estimate probability distributions of touchdown conditions, without utilizing a Monte Carlo simulation. Example applications are presented, including one-step and two-step flare strategies for the space shuttle orbiter. The computed probability distributions for the two-step flare are compared with the corresponding histograms from an independent Monte Carlo simulation of the same situation. The computed distributions are very good fits to the Monte-Carlo-generated histograms for pertinent longitudinal and lateral variables at three points (including touchdown) along the vehicle's final approach trajectory. The model, thus verified, has more inherent power for assessing the effects of system element changes (e.g., vehicle characteristics, flight control laws, ground guidance, etc.) than conventional Monte Carlo techniques.

CONTENTS

LIST OF FIGURES

TABLES

SECTION I

INTRODUCTION

This report describes an approach and landing system model* that can be used to estimate distributions of touchdown conditions without utilizing a Monte Carlo simulation. The primary purpose of the model is to establish a structure containing the system elements, command inputs, disturbances, and their interactions in an analytical framework so that the effects of changes in the various system elements on control precision and available margins of safety can be estimated. The model is applied to the terminal phase of flight of the space shuttle orbiter, and example calculations are made for the North American Rockwell high cross-range vehicle. These calculations include a limited application of the model to a one-step, and a broader application to a two-step, flare situation. Also included is a comparison of the computed two-step results with Bell Aerospace Corporation's Monte Carlo simulation results for the same situation. Excellent agreement was obtained.

The report is divided into five sections. Section II contains an overview and general description of the analysis technique. Section III presents the one-step flare example application. Section IV contains the two-step flare application and a comparison with Bell's Monte Carlo results. Section V then follows with conclusions and comments.

*The system model described herein is intimately associated with particular systems analysis techniques and procedures. However, the general name, "system model," is used to denote a broader representation of a given situation than implied by an "analysis technique." The authors wish to apologize for any confusion this semantic choice may create; certainly none was intended.

SECTION II

OVERVIEW AND GENERAL DESCRIPTION OF ANALYSIS TECHNIQUE

A. OVERVIEW OF ANALYSIS TECHNIQUE

Rather than using a direct method (such as Monte Carlo) to generate touchdown distributions, the final approach phase of flight is broken down into two distinct flight segments, and calculations for each segment are made separately. The final calculation of touchdown condition distributions is then achieved by appropriately combining the separate results. The analysis is done in this way to make it possible to take advantage of certain mathematical simplifications that can be applied only to individual parts of the approach calculations. The end result is an alternative to a Monte Carlo simulation for estimating distributions of touchdown conditions.

Basically, the technique is to separate a constant glide-slope phase from the flare and touchdown phase. Glide-slope tracking is essentially a stationary process involving small perturbations, wherein linearized equations of motion are applicable, while the flare and touchdown phase involves larger perturbations and significant nonlinear effects due to contacting the ground (e.g., touchdown only occurs when $\dot{h}$ is negative and h is zero).

For the glide-slope tracking phase, linearized equations of motion are used to compute rms values of vehicle dispersions due to random gust and beam noise disturbances. Because these disturbances can be considered to have stationary Gaussian distributions (Ref. 1), and because the vehicle (plus control system) can be represented as a linear system, the resulting vehicle dispersions are stationary and Gaussian. Thus, a set of normally distributed (Gaussian) vehicle dispersions can be computed, which represent the distributions of initial conditions for the flare phase of flight.

For the flare phase a nonlinear simulation is run on an analog (or digital) computer to obtain a mapping of initial conditions (and the effects of wind profiles and shears) onto the ground. The effects of random gusts encountered after the start of flare are accounted for by the inclusion of

the most significant aspects of a random gust environment near the ground. These include a probabilistic ramp wind change during the final few seconds prior to touchdown (which will be discussed further later). One more point regarding gusts will be mentioned here. This is that (in our computations) the random gusts are effectively "turned off" at the start of flare, which is the exact point in the approach that the beam-following part of the flight control system is turned off. This coincidence was intentional. If beam-following control were allowed to remain on after the (simulated) gust environment was discontinued, then the computed gust-induced dispersions would go to zero. Clearly, such a procedure should not be adopted.

A digital computer was used to combine the results of the initial condition calculations and the mapping of initial conditions onto the ground. The computational procedure involves integrations of conditional probabilities over appropriate variables (which will be explained in detail later). The result is a probability density distribution at touchdown for each important variable. To compute the probability of exceeding a given touchdown window is then straightforward because areas under tails of probability density plots represent exceedance probabilities.

B. GENERAL DESCRIPTION OF ANALYSIS TECHNIQUE

Here, it was intended to present a step-by-step list of tasks comprising the analysis technique. However, because there are a number of alternative groups of steps to be followed at various points in the analysis (depending on the particular situation), the step-by-step list gets quite complicated if all contingencies are included. To avoid this, we will sacrifice some generality in favor of clarity and conciseness. It is unrealistic to imagine that we could anticipate all contingencies anyway. Accordingly, we present what might be called a "typical" set of steps for the longitudinal situation (similar "typical" steps are also required for lateral calculations) as follows:

1. Simulate complete vehicle, guidance, and control system on an analog or digital computer.

2. Adjust system parameters and initial conditions to obtain a nominal trajectory from equilibrium glide through to touchdown.

3. Compute maximum expected values of dispersions at <u>start</u> of final flare.

- Use linearized, perturbation equations of motion for vehicle just prior to final flare.
- Use guidance and control system definitions for glide phase.
- From nominal trajectory, determine nominal conditions just prior to final flare.
- Use spectral descriptions of gusts, beam noise, and any other random disturbances.
- Compute closed-loop transfer functions for gust (etc.) inputs.
- The following steps are suggested to select "maximum" gust level.

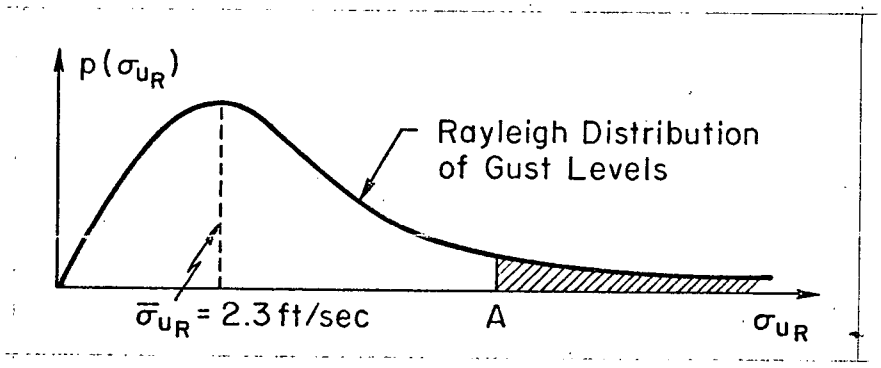

$$\sigma_{u_g} = \sigma_{u_R} \times f(\text{altitude})$$

a. Pick $A = 3.5\ \sigma_{u_R} \doteq 8$ ft/sec [this gives $P(\sigma_{u_R} > A) \doteq 0.0021$].

b. This gives a gust level ($\sigma_{u_R} = A$) to be used to compute σ_{u_g} and σ_{w_g} at altitude.

- Use gust (etc.) power spectra and closed-loop vehicle transfer functions to compute power spectra for vehicle dispersions, η ($\eta = h_\epsilon$, $\dot{h}_\epsilon$, etc.).
- Integrate power spectra to compute rms values.
- Pick $\eta_{MAX} \doteq 3\ \sigma_\eta$ for initial conditions at the start of final flare.

[$\eta_{MAX}/\sigma_\eta = 3.1$ gives $P(\underbrace{\eta > \eta_{MAX}}_{\text{one tail only}}) \doteq \underbrace{0.00097}_{\doteq 1/2\ P(\sigma_{u_R} > A)}$]

- Combine the effects of gusts, beam noise, etc., via an RSS calculation to get ranges of all initial conditions at start of final flare.

4. Map initial conditions (at start of final flare) onto the ground.

   - Use complete simulation (from 1) and apply initial conditions one at a time (using values up to maximums determined from 3), recording touchdown conditions each time.
   - Apply ramp wind change (representing short-time approximation to random gust environment during flare) just prior to touchdown. Ramp is a horizontal wind change,,of magnitude Δu_g during time T. With a constant Δu_g, use various durations, T, to determine maximum sensitivities for $\dot{Z}_{TD}$, X_{TD}, etc. Then record touchdown conditions for various Δu_g magnitudes (using times for maximum sensitivities).
   - Apply mean wind profiles of various magnitudes, u_w, (up to maximum winds) from an altitude of 1000 ft to touchdown (not just during flare) and record touchdown conditions.

5. Establish touchdown mapping relationships.

   - Plot touchdown conditions (e.g., X_{TD}) vs initial conditions, mean wind, and Δu_g.
   - Determine best-fit linear equations to plotted individual relationships.
   - Combine above equations to get overall equations (e.g., $X_{TD} = X_{TD_o} + A\Delta u_w + Bh_\epsilon + \ldots$).

6. Determine important variables.

   - Define "successful" touchdown window.
   - For a worst-case input, determine which variables remain well within their respective successful ranges. Those that do are most likely not important; those that do not are the important ones.

7. Compute means and rms values (μ and σ) for the conditional distribution of each important variable (X_{TD} is used as an example here).

   - Group the terms in the touchdown equations as follows:

$$X_{TD} = \underbrace{X_{TD_o} + A\Delta u_w}_{\equiv X_{TD_1}} + \underbrace{Bh_\epsilon + Cu_\epsilon + D\dot{h}_\epsilon}_{\equiv h_1} + E\Delta u_g$$

For a given wind profile, X_{TD_1} is a constant. For a given rms gust level, h_1 and $E\Delta u_g$ are independent, zero-mean, Gaussian random variables.

- Use perturbation equations of motion to compute transfer functions for h_1 to u_g, w_g, beam noise, and equipment error (etc.) inputs.
- Use these transfer functions, along with power spectra of the disturbances, to compute rms values of h_1 due to each input.
- Combine these separate sources of dispersion to define a "total" σ_{h_1}.

$$\sigma_{h_1} = \sqrt{\sigma^2_{h_{1_{u_g}}}\sigma^2_{u_g} + \sigma^2_{h_{1_{w_g}}}\sigma^2_{w_g} + \sigma^2_{h_{1_{\text{beam noise}}}} + \cdots}$$

or

$$\sigma_{h_1} = \sqrt{[\sigma^2_{h_{1_{u_g}}} + \underbrace{(\sigma^2_{w_g}/\sigma^2_{u_g})}_{\text{known from gust model}}\sigma^2_{h_{1_{w_g}}}]\sigma^2_{u_g} + \sigma^2_{h_{1_{\text{beam noise}}}} + \cdots}$$

- Compute the ratio of $\sigma_{\Delta u_g}$ to σ_{u_g} corresponding to the best linear fit (using a least square error criterion) to a short-time gust history as follows:

$$\frac{\sigma_{\Delta u_g}}{\sigma_{u_g}} = \frac{1}{\omega_o^2 T^2}\sqrt{24\,\omega_o^3 T^3 + 72(2+\omega_o T)(2-\omega_o T) - 72(2+\omega_o T)^2 e^{-\omega_o T}}$$

where: ω_o is the break point of the u_g spectrum and T is the duration of Δu_g determined in step 4

For times less than 10 sec this expression gives values which are about 13 percent larger than the equivalent values obtained by fitting a short-time gust history with a linear fit through the initial and end points. The expression obtained via this end point technique is given in Ref. 3 as:

$$\sigma_{\Delta u_g}/\sigma_{u_g} = \sqrt{2\left(1 - e^{-\omega_o T}\right)}$$

- Compute conditional mean and rms values.

$$\mu_{X_{TD}} = X_{TD_1}$$

$$\sigma_{X_{TD}} = \sqrt{\sigma_{h_1}^2 + E^2\sigma_{\Delta u_g}^2}$$

$$= \sqrt{\left(\sigma_{h_{1_{u_g}}}^2 + \frac{\sigma_{w_g}^2}{\sigma_{u_g}^2}\,\sigma_{h_{1_w}}^2 + \frac{\sigma_{\Delta u_g}^2}{\sigma_{u_g}^2}\right)\sigma_{u_g}^2 + \sigma_{h_{1_{\text{beam noise}}}}^2 + \ldots}$$

8. Integrate conditional distributions over all values of mean wind and gust magnitude to obtain "overall" probability density distributions at touchdown for each important variable.

9. Integrate probability density distributions up to the "successful" window limits to determine the probability of a successful touchdown for each variable.

10. Combine the individual success probabilities to obtain an overall probability of a successful touchdown.

SECTION III

EXAMPLE APPLICATION TO ONE-STEP FLARE

A. VEHICLE AND TASK DESCRIPTION

1. Vehicle Definition

The example vehicle is the 134C version of the North American Rockwell high cross-range orbiter (Ref. 5). For the example calculations, only the longitudinal situation is considered.

2. Successful Touchdown Window

Table 1 lists the limiting values of longitudinal variables for a successful landing (as used in the example calculations). Note that no airspeed requirement is needed because the vehicle is flyable at speeds well below the speed that will result in tail scrape. However, excess airspeed will affect the stopping distance, X_{stop}, which is a function of the inertial (ground) speed, U.

TABLE 1

"SUCCESSFUL" LONGITUDINAL TOUCHDOWN WINDOW

WINDOW DEFINITION	COMMENTS
$800 < X_{TD} < 2300$ ft	1550 ft ±750 ft (insures touchdown on runway)
$0 < \dot{Z}_{TD} < 6$ ft/sec	3 ft/sec ±3 ft/sec (insures acceptable impact at touchdown)
$X_{stop} < 9200$ ft ($X_{stop} \doteq 7000$ ft + ΔX_{TD} + $20U_{TD}$ ft/kt)	X_{stop} is computed stopping distance. U_{TD} is perturbation in ground speed at touchdown (insures stopping on 10,000 ft runway and leaves same 800 ft margin as does X_{TD})

3. Basic Flare Logic

For the one-step flare an exponential flare path was selected. This is accomplished by making commanded sink rate proportional to altitude. Details of the selected flare logic will be presented later.

4. Inputs

a. Steady Wind

The steady wind profile of Ref. 2 was used in the example calculations. This results in a profile whose magnitude and direction are determined by random selections from given distributions. Thus, for any given approach and landing, the profile is fixed, but from one approach to the next the profile changes. A sample profile is shown in Fig. 1. To obtain any other profile it is only necessary to scale up (or down) the wind magnitude. Conveniently, any particular profile can be completely determined by specifying the magnitude at a given reference altitude. For our purposes a wind reference altitude of 10 ft was selected. At this altitude the wind magnitude varies from a 10 kt tail wind to a 25 kt head wind.

By combining the distributions of magnitude and direction given in Ref. 2, a distribution of the wind component parallel to the runway can be determined. A rough plot of this distribution is shown in Fig. 2. It is presented to give a feel for relative likelihoods of the head and tail winds that are used. From the plot it is seen that the most likely longitudinal wind condition is a head wind of about 8 kt. As a consequence, a "nominal" flight condition will be defined that includes an 8 kt head wind (measured at an altitude of 10 ft).

b. Random Gusts

In addition to the steady wind profile, a turbulent wind environment is also considered. The model for this turbulent wind is given in Ref. 2. Basically, the model provides for random gusts whose rms level has a Rayleigh distribution (with a characteristic speed of 2.3 ft/sec), and whose frequency content is a function of altitude.

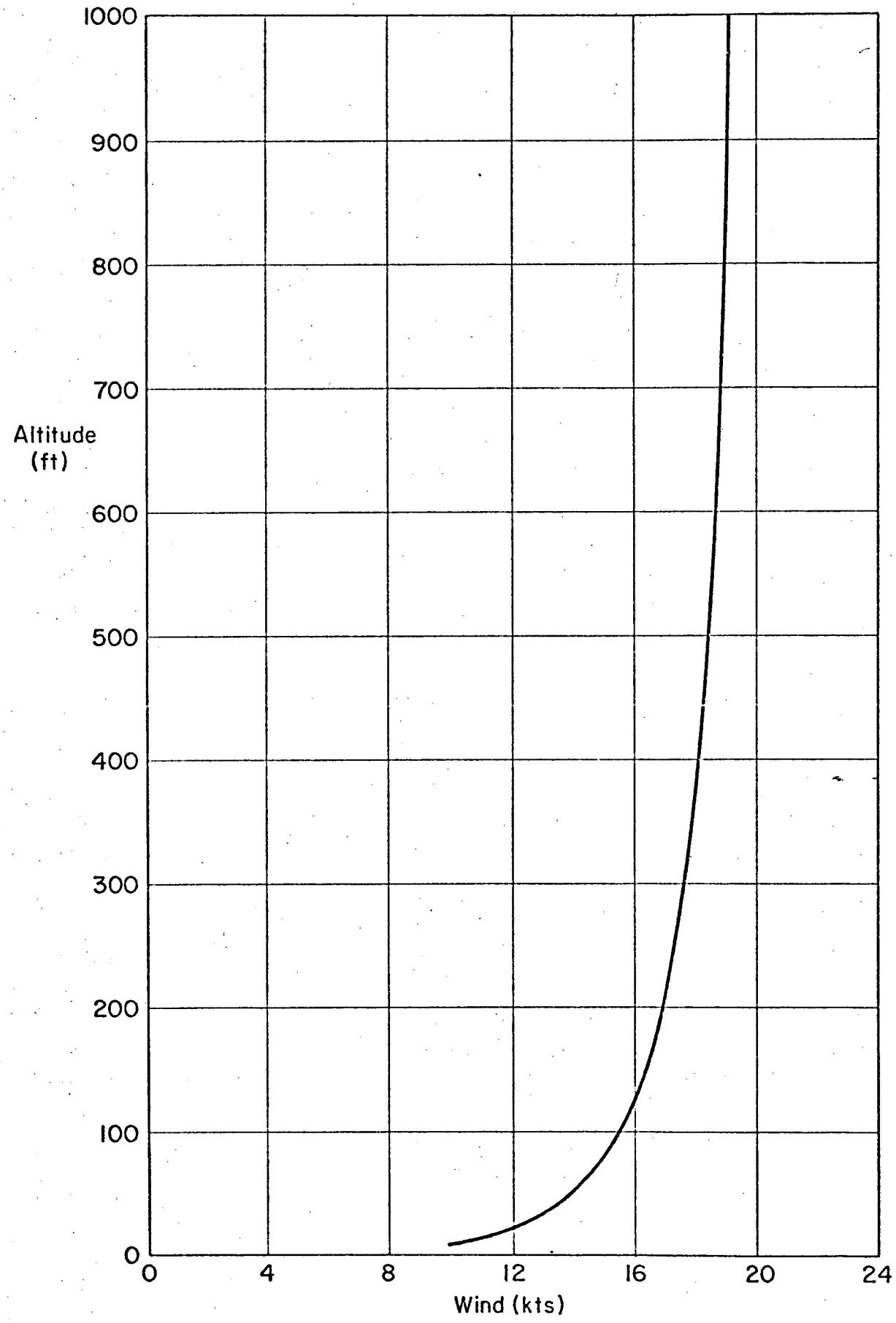

Figure 1. Wind Profile Associated with
10 Kt Wind at 10 Ft Altitude

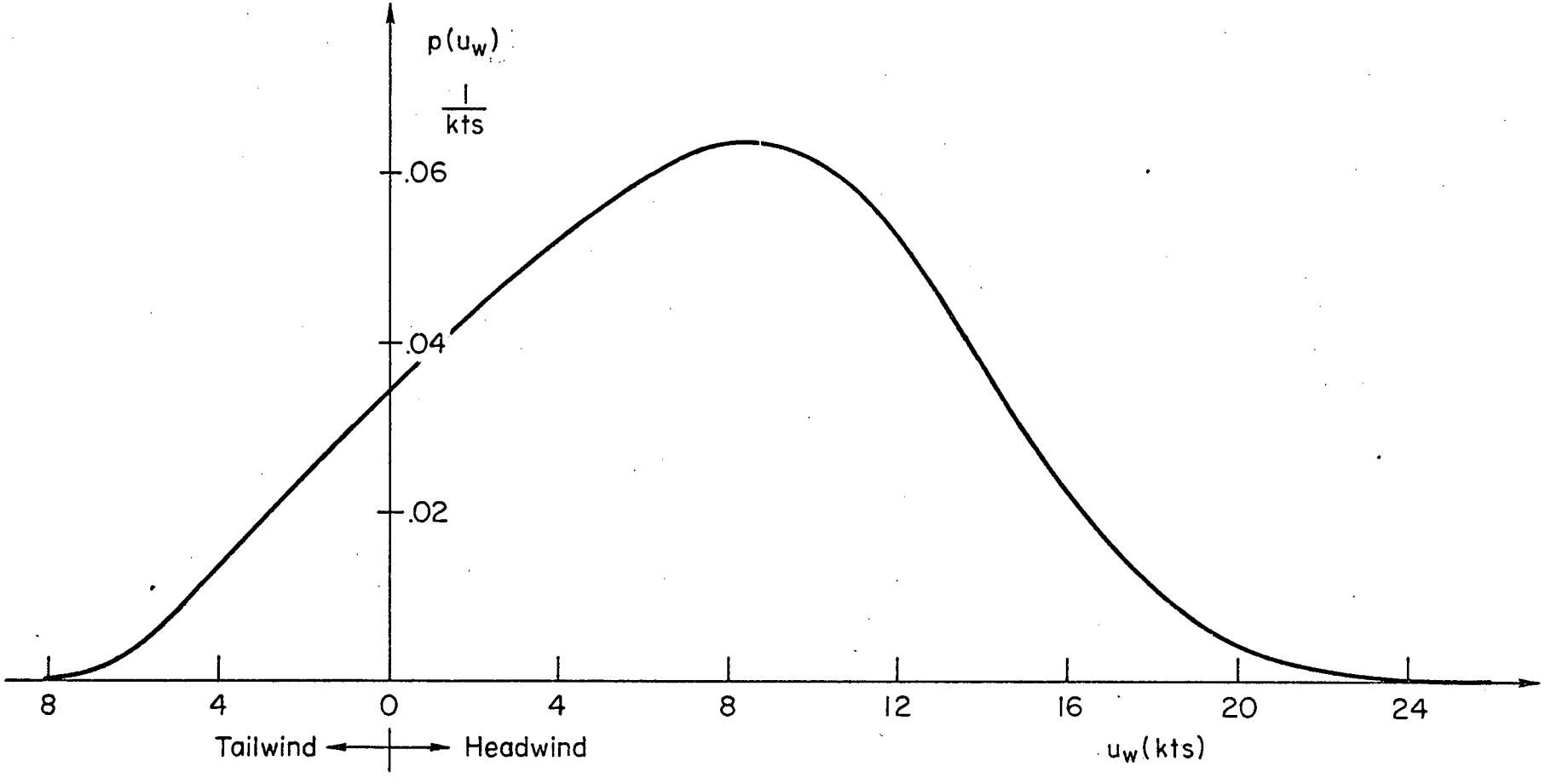

Figure 2. Approximate Distribution of Head and Tailwinds (Measured at an Altitude of 10 Ft)

(Table 2 gives the gust spectral shapes for an altitude of 1200 ft.) Further, the model provides for the ratio of the rms level of vertical gusts to the rms level of longitudinal gusts to also be a function of altitude (although the individual gust components are not correlated). At 1200 ft the ratio is 0.88.

TABLE 2

GUST POWER SPECTRA FOR AN ALTITUDE OF 1200 FT*

u_g	$\Phi_{u_g u_g} = \dfrac{K_u}{\omega^2 + 0.11}$
w_g	$\Phi_{w_g w_g} = \dfrac{K_w^2(\omega^2 + 0.66)}{(\omega^2 + 0.18)^2}$

*Values of K_u, K_w are selected from a Rayleigh distribution

For our calculations, these random gusts are applied to the vehicle only prior to the start of flare. However, because a random gust environment exists all the way to touchdown it is necessary to account for any significant gust effects during flare by adding back the most important gust effect, which is a ramp change in horizontal wind during the last few seconds prior to touchdown. The rest of the random gust environment (during flare) has very little effect on the touchdown conditions. This gust-produced ramp change in wind is actually a random wind shear, as discussed in the next paragraph.

c. Random Wind Shear

As mentioned above, the random wind shear is the most significant aspect of the random gusts during flare. Although its primary effect is to produce hard landings, the effects on other touchdown variables were not neglected. A hard landing generally arises because an unanticipated large decrease in vehicle airspeed (due to a tailwind gust or a decrease in headwind) occurs when the vehicle is close to

the ground. The decrement in airspeed produces a decrement in lift (even though the angle of attack may be increasing), which in turn produces an increased sink rate, which then results in an almost immediate touchdown. If the random shear is of the opposite sign (i.e., an increase in airspeed) then the flight path is shallowed out somewhat, but nothing "interesting" happens.

The random shear is simulated as a ramp change in horizontal wind (superimposed on the shear due to the steady-wind profile) starting at an altitude of approximately 10 ft. This results in about 3 sec of shear duration prior to touchdown, which is consistent with the results of Ref. 3 (for conditions leading to hard landings). The magnitude of this wind change is given in Ref. 3 as a zero-mean, Gaussian random variable with an rms value defined as

$$\sigma_{\Delta u_g} = \sigma_{u_g} \sqrt{2\left(1 - e^{-r/L_u}\right)} \qquad (1)$$

where r is the distance flown (during the Δu_g), and L_u is the scale length for longitudinal gusts. However, this representation is one in which a linear fit merely connects the initial and final points of a sample time history of u_g. As noted above, in the listed analysis "steps," a better representation of a short-time gust history is obtained by fitting the entire sample, rather than just connecting the end points. The corresponding expression for $\sigma_{\Delta u_g}$ using a least squares fit is:

$$\sigma_{\Delta u_g} = \frac{\sigma_{u_g}}{\omega_o^2 T^2} \sqrt{24\omega_o^3 T^3 + 72(2 + \omega_o T)(2 - \omega_o T) - 72(2 + \omega_o T)^2 e^{-\omega_o T}} \qquad (2)$$

where ω_o is the breakpoint of the u_g spectrum and T is the duration of the sample. (Note that r/L_u used earlier is identical to $\omega_o T$ used here.) This preferred representation results in $\sigma_{\Delta u_g}$ being about 13 percent larger than the value obtained for the end point fit (for times up to 10 sec).

d. Other Error Sources

Glide slope beam noise, measurement errors, pilot remnant (for manual control), and other sources of errors applicable in general, have not been included in these first simple illustrative example calculations. However, they are included, as appropriate, in the later two-step flare calculations.

5. Preflare Flight Condition

The steady-state flight condition prior to flare is defined in Table 3.

TABLE 3

PREFLARE FLIGHT CONDITION

Flight path angle	−10 deg
Airspeed	302 kt
Angle of attack	5.3 deg
Nominal wind at 800 ft altitude	−16.5 kt (headwind)

6. Preflare Flight Control System

Figure 3 shows the inner- and outer-loop control system block diagrams for preflare glide slope tracking. Table 4 contains a list of the dimensional stability derivatives that are appropriate for the preflare steady-state flight condition. The associated closed-loop Bode plots are presented in Figs. 4 and 5.

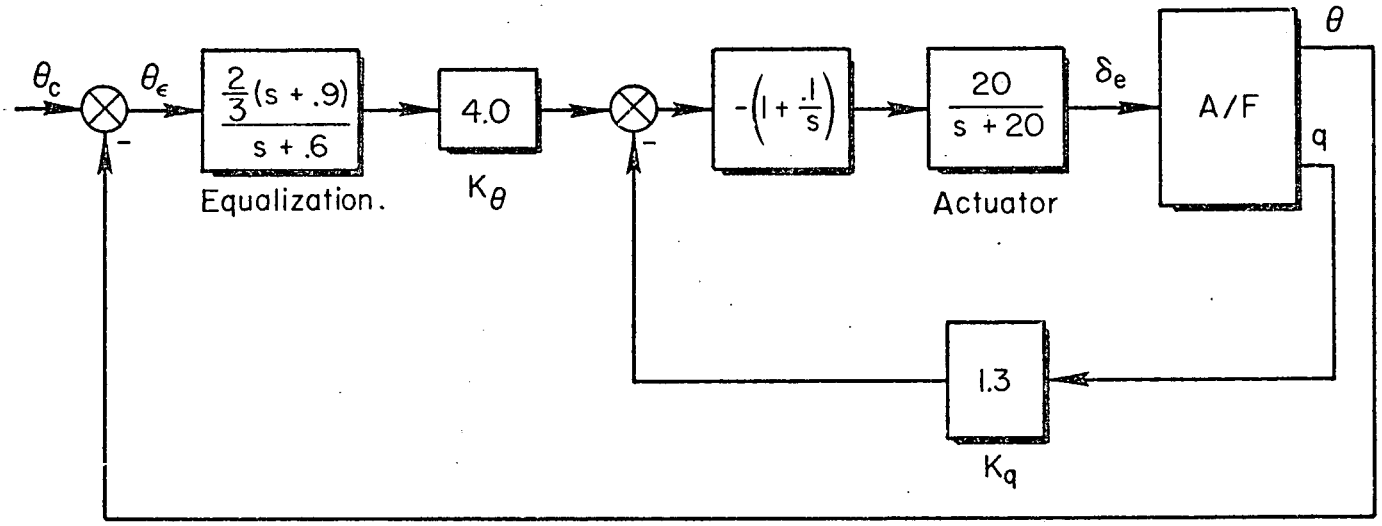

a) Inner Loop SAS Gives Augmented Vehicle

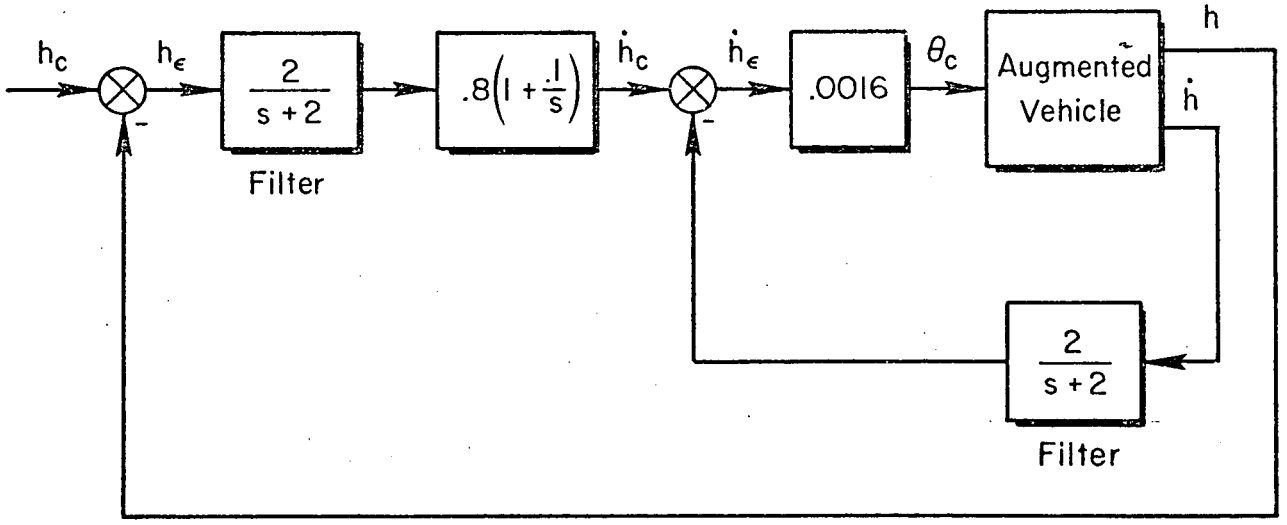

b) Outer Loop Control System

Figure 3. Closed-Loop Block Diagrams for Preflare Flight Control System

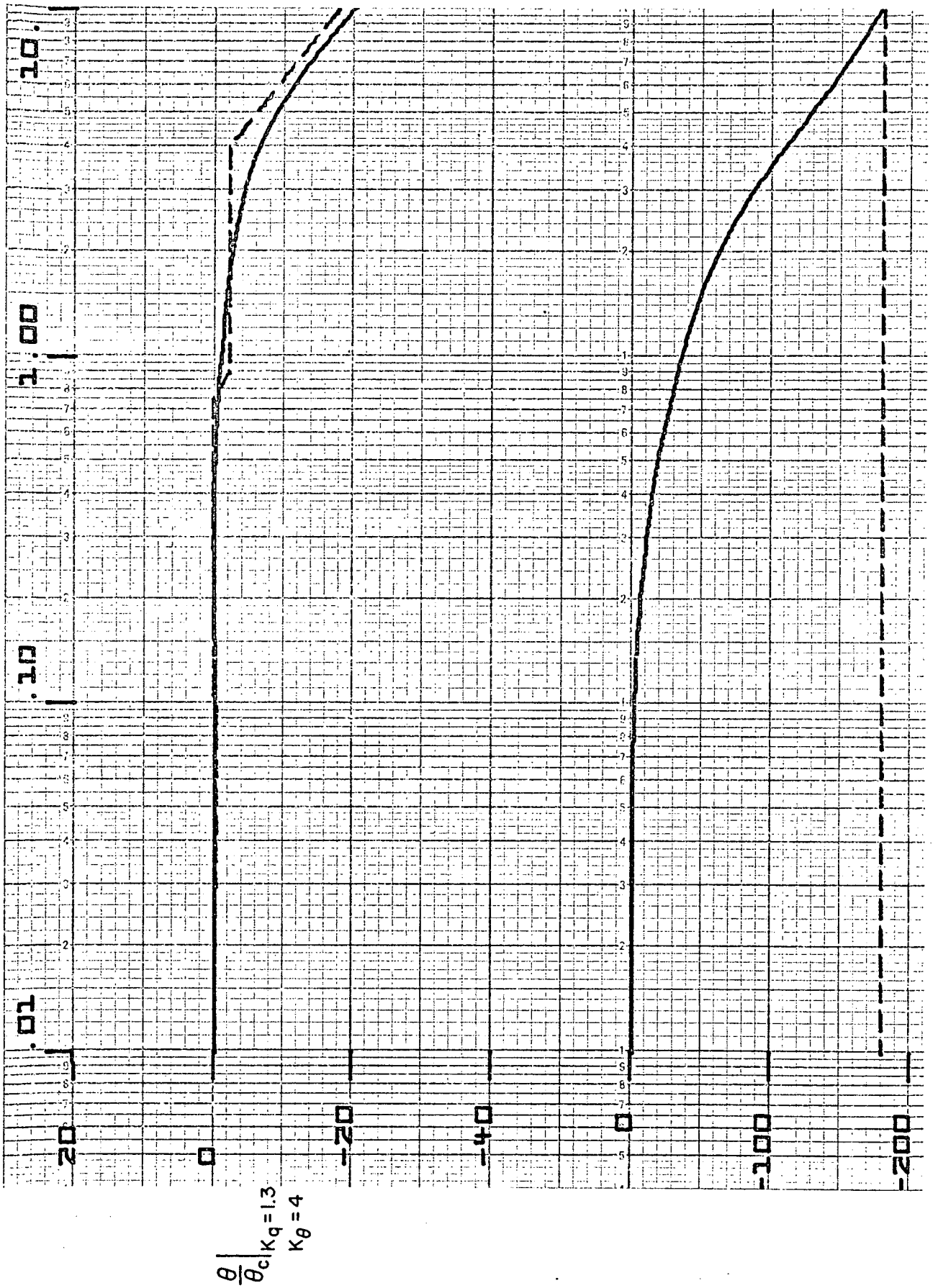

Figure 4. θ/θ_c for Augmented Vehicle

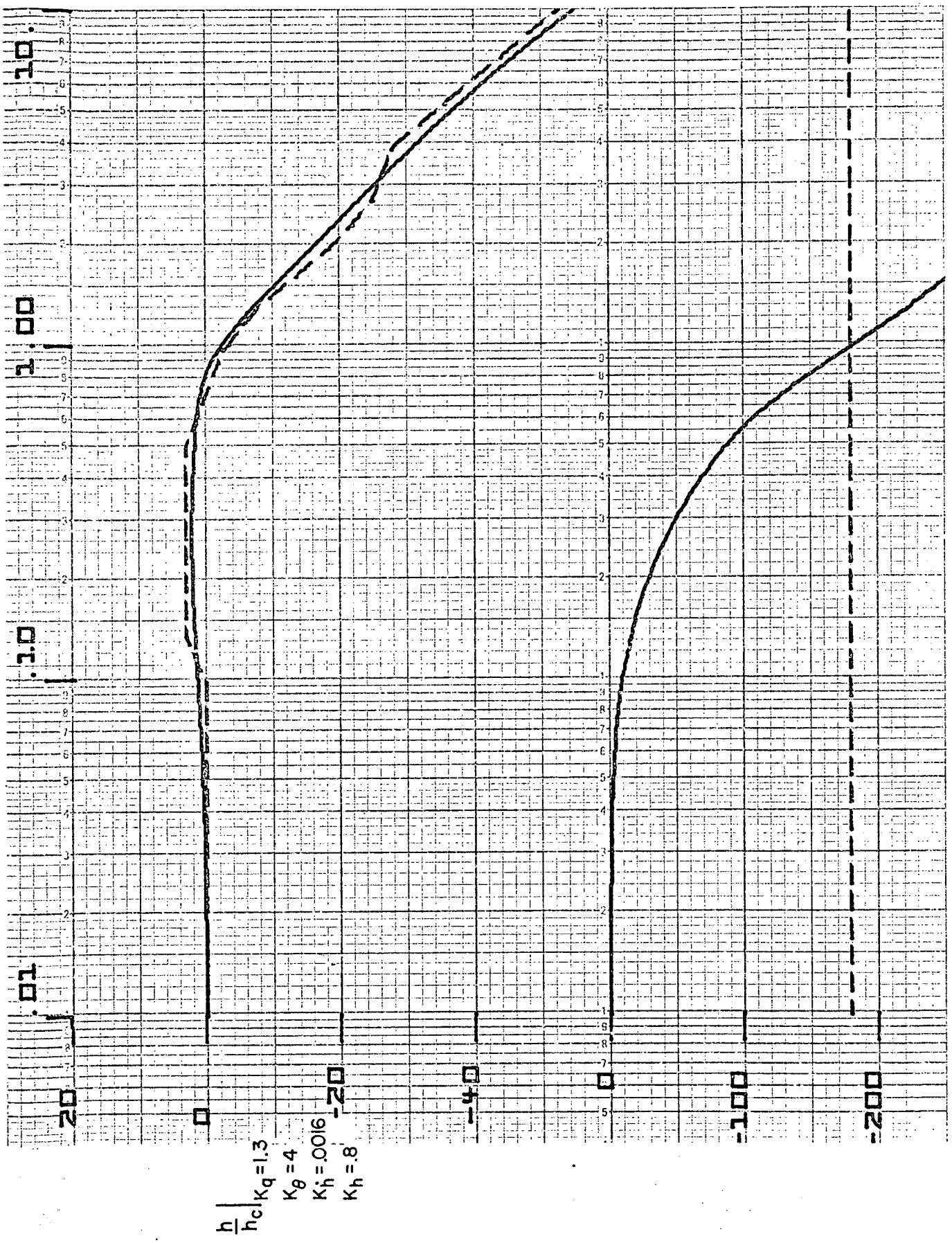

Figure 5. h/h_c for Closed-Loop System

TABLE 4

DIMENSIONAL DERIVATIVES FOR PREFLARE FLIGHT CONDITION

$X_u = -0.0206$ 1/sec	$Z_{\delta_e} = -242.$ ft/sec^2/rad
$X_w = -0.00654$ 1/sec	$M_u = 0$
$X_{\delta_e} = -40.7$ ft/sec^2/rad	$M_w = -0.00579$ 1/ft-sec
$Z_u = -0.126$ 1/sec	$M_q = -0.579$ 1/sec
$Z_w = -1.28$ 1/sec	$M_{\delta_e} = -3.41$ 1/sec^2

7. Calculation of RMS Dispersions Prior to Flare

The Table 4 values, and the control/guidance logic represented by the block diagrams of Fig. 3, were used in standard (e.g., Ref. 4) linearized, closed-loop perturbation equations of motion to obtain transfer functions for gust inputs. (The effect of the nominal wind condition was accounted for in the equations of motion by utilizing airspeed in the terms arising from aerodynamic forces, and ground speed in the terms arising from inertial accelerations. Although this is not a large effect, it was done to minimize the introduction of errors in the calculations.)

Using the gust spectra (given earlier) with the gust input transfer functions (given in the Appendix) leads to power spectral density expressions for each variable. Because the area under a power spectral density plot is the variance for the input considered, and because variances due to independent Gaussian inputs can be added directly, the overall rms value for any variable can easily be found by taking the square root of the sum of the variances from all of the random inputs. For our situation this becomes (using η as a generic example variable):

$$\sigma_\eta = \left[\int_o^\infty \left| \frac{\eta}{u_g} \right|^2 \Phi_{u_g u_g} d\omega + \int_o^\infty \left| \frac{\eta}{w_g} \right|^2 \Phi_{w_g w_g} d\omega \right]^{1/2} \qquad (3)$$

Expressions such as this were used to compute rms values for vehicle dispersions just prior to flare. An rms horizontal gust level of 2.04 ft/sec (which is the most probable gust level according to the given Rayleigh distribution at 1200 ft altitude) was used to compute rms dispersions in speed, sink rate, and deviation from the glide slope beam. The results are:

$$\sigma_u = 0.837 \text{ ft/sec}$$

$$\sigma_{\dot{z}} = 1.25 \text{ ft/sec}$$

$$\sigma_{h_\epsilon} = 2.47 \text{ ft}$$

Further discussion of rms dispersions is deferred until the equations for touchdown conditions have been presented.

8. Flare Control System

The flare control system used in the example calculations is a constant gain system that is switched in at the flare initiation height of 800 ft. It was possible to use a fixed-gain system because the airspeed at touchdown is sufficiently high that the $\theta_c/\dot{h}_\epsilon$ ratio remains acceptable. (However, an airspeed loop was used to effect a continuous trim change as speed bleeds off.) The outer-loop block diagram of the overall control system (including the switching required to go from the preflare system to the flare system) is given in Fig. 6a. As indicated in Fig. 6b, the landing gear is lowered as a function of sink rate at 4000 ft altitude to control the landing speed (in the presence of winds) without making large changes in the flare trajectory.

Feeding forward an open-loop pitch or pitch rate command (an early variant of the flare system) to minimize deviations from an exponential trajectory did not significantly affect touchdown performance. What was really needed was an additional pitch-up command just before touchdown to compensate for the loss of lift due to speed bleeding off. But, rather than doing this with an open-loop feedforward command, it was done via an airspeed loop closure (during flare only). Although this loop is unstable in the classical sense (because a decrease in airspeed results in an increase in pitch attitude which causes a further decrease in airspeed, etc.), in this situation touchdown occurs before the divergence has a change to build up. The airspeed loop has two

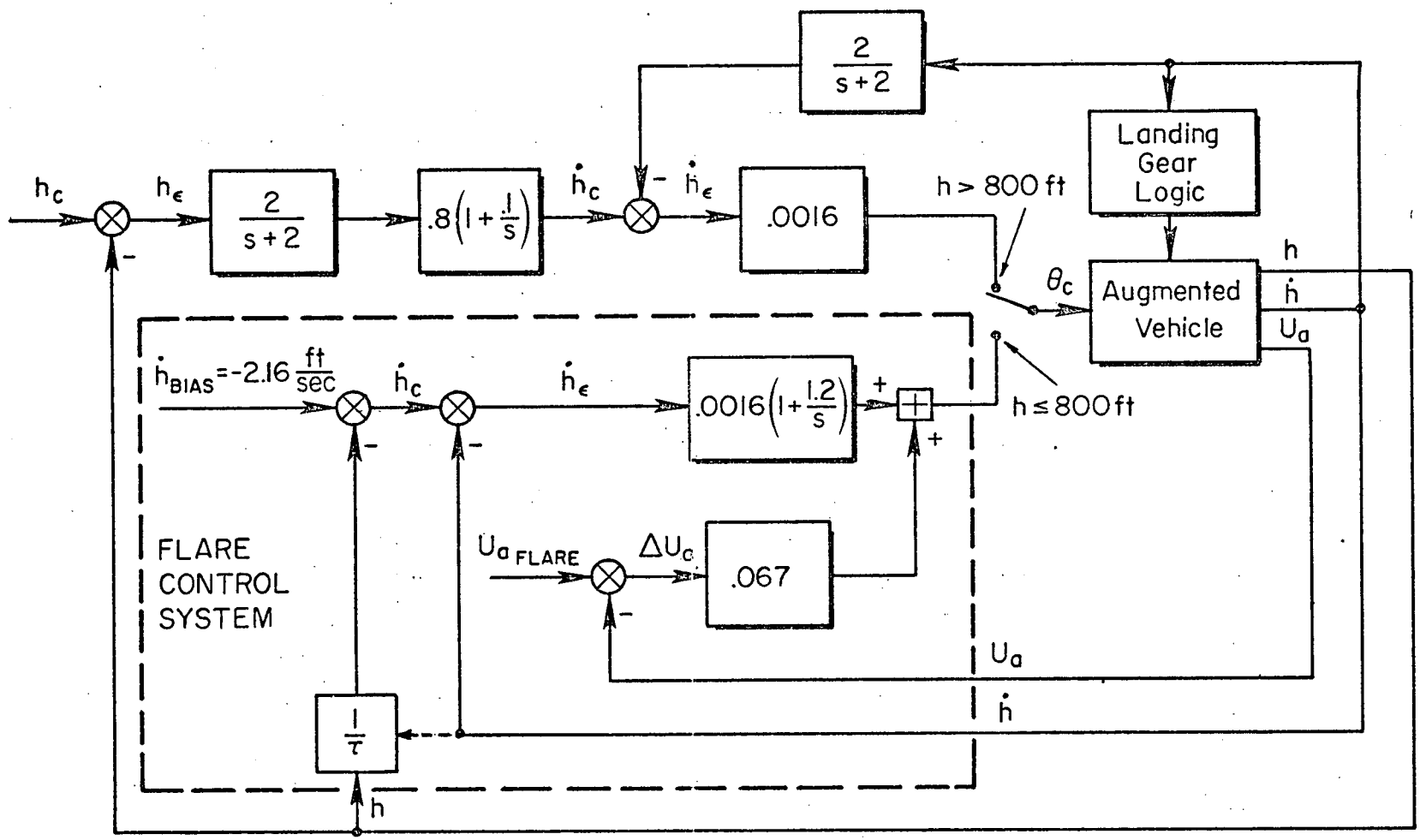

1.) $\frac{1}{\tau}$ is "adjusted" to make $\dot{h}_\epsilon = 0$ at start of flare $\left(\text{i.e., } \frac{1}{\tau} = \frac{-\dot{h}_{800ft} - 2.16 \frac{ft}{sec}}{800\,ft}\right)$

2.) $U_{a_{FLARE}}$ is airspeed at instant flare is initiated (and is held constant during flare)

3) "Landing Gear Logic" for lowering landing gear is shown in Figure 6b

Figure 6a. Outer-Loop Longitudinal Control System During Glide-Slope Tracking and Flare

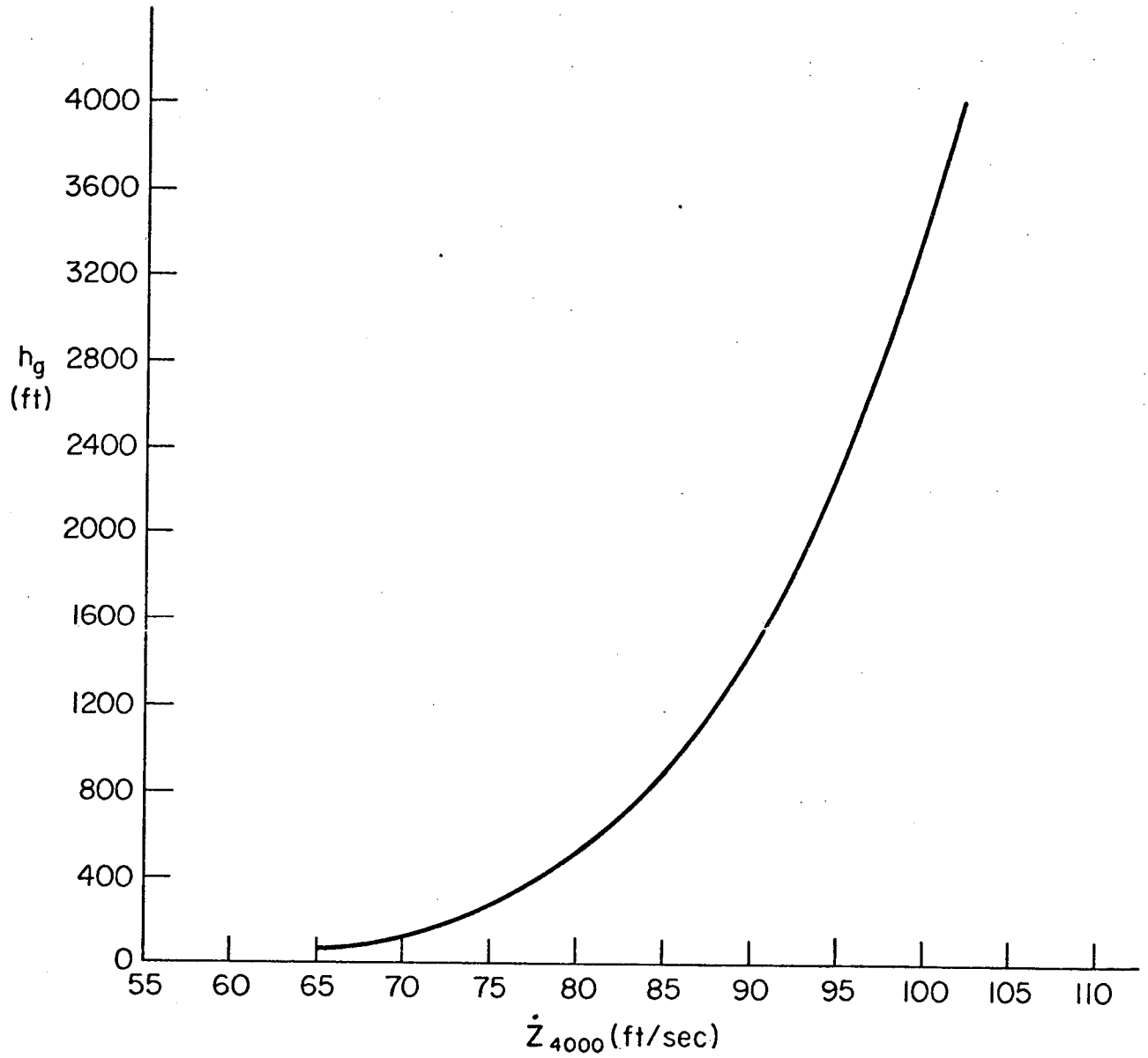

Figure 6b. Gear-Down Altitude as a Function of Sink Rate at 4000 Ft Altitude

distinct advantages. It provides the desired increase in pitch rate near touchdown (when airspeed bleedoff cancels the expected lift increment from any angle-of-attack increase demanded by the sink rate error control system), and it provides windproofing against shears that otherwise might produce hard landings. That is, if a sudden decrease in headwind occurs near touchdown, the sink rate increase (due to the airspeed decrease) is averted by pitching up to increase the angle of attack (and maintain lift) before a sink rate error can develop.

The magnitude of the gain in the airspeed feedback was determined as follows. The lift equation is

$$L = \frac{1}{2} \rho U_a^2 S C_{L_\alpha} \alpha \tag{4}$$

With lift equal to weight,

$$\alpha = \frac{2W}{\rho U_a^2 S C_{L_\alpha}} \tag{5}$$

Then,

$$\frac{d\alpha}{dU_a} = \frac{-4W}{\rho U_a^3 S C_{L_\alpha}} = \frac{-2\alpha}{U_a} \tag{6}$$

Therefore,

$$\Delta\alpha \doteq \frac{-2\alpha_o}{U_a} \Delta U_a \tag{7}$$

For relatively short times,

$$\Delta\theta \doteq \Delta\alpha \tag{8}$$

giving

$$\Delta\theta \doteq \frac{-2\alpha_o}{U_a} \Delta U_a \tag{9}$$

For our flare situation,

$$\alpha_o \doteq 11 \text{ deg} \tag{10}$$

$$U_a \doteq 330 \text{ ft/sec} \tag{11}$$

Therefore,

$$\frac{\Delta\theta}{\Delta U_a} \doteq -0.067 \frac{\text{deg}}{\text{ft/sec}} \tag{12}$$

This value of gain gave good results. A higher value was tried (to compensate for lags in pitch response) but it resulted in worse sink rate control.

B. ANALOG SIMULATION TO MAP INITIAL CONDITIONS ONTO THE GROUND

1. Equations Used

The equations mechanized on an analog computer were the "total" equations of motion, as opposed to only perturbation equations. Further, the dynamic pressure was one of the variables (rather than just using an average value). Based on the specifically applicable Ref. 5 data, the nondimensional stability derivatives were held constant during the flare. The equations that were modeled and the coordinate system definitions are presented in Fig. 7. In this figure the subscripts I, a, w, and B refer to inertial, aerodynamic, wind, and body, respectively. The rest of the symbols are standard, and are not redefined here. Figure 8 presents an analog mechanization diagram to show how each variable was computed.

2. Results of Mapping Initial Conditions (IC's) and Wind Effects

Figures 9a through 9h present the results of mapping initial conditions at the start of flare onto the ground, one at a time. Also included are the effects of wind profiles of various magnitudes (u_w is the wind speed at an altitude of 10 ft) and wind shears near the ground (Δu_g). On each plot is a linear fit to the data, and the mathematical expression for the linear fit. It can be seen that linear fits are very good approximations to the data, with the possible exception of the $\dot{Z}_{TD}$ fit for negative values of

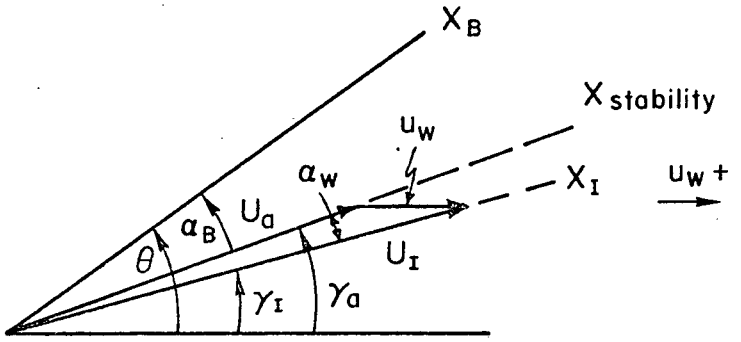

$$Q \equiv \frac{1}{2} \rho U_a^2$$

$$C_{L_1} = C_{L_o} + C_{L_\alpha} \alpha_B$$

$$C_L = C_{L_1} + C_{L_{\delta_e}} \delta_e$$

$$C_D = C_{D_o} + b_2 C_{L_1}^2 + C_{D_{\delta_e}} \delta_e + C_{D_{\delta_g}} \delta_g$$

$$C_m = C_{m_o} + C_{m_\alpha} \alpha_B + C_{m_{\delta_e}} \delta_e + \frac{\ell}{2V_a} C_{m_q} q$$

$$U_I = U_a \cos \alpha_w + u_w \cos \gamma_I \doteq U_a + u_w$$

$$\theta = \gamma_a + \alpha_B$$

$$\gamma_I = \gamma_a + \alpha_w$$

$$\alpha_w = \sin^{-1} \left(\frac{- u_w \sin \gamma_I}{U_a} \right) = \sin^{-1} \left(\frac{- u_w \sin \gamma_a}{U_I} \right) \doteq \frac{- u_w \gamma_a}{U_I}$$

$$\doteq \frac{- u_w \gamma_I}{U_a}$$

$$X = m\dot{V}_I = QS \left[- C_D \cos \alpha_w + C_L \sin \alpha_w \right] - mg \sin \gamma_I$$

$$Z = - mU_I \dot{\gamma}_I = QS \left[- C_L \cos \alpha_w - C_D \sin \alpha_w \right] + mg \cos \gamma_I$$

$$M = I_y \ddot{\theta} = QS\bar{c} C_m$$

Figure 7. Equations Modeled and Coordinate System Definitions

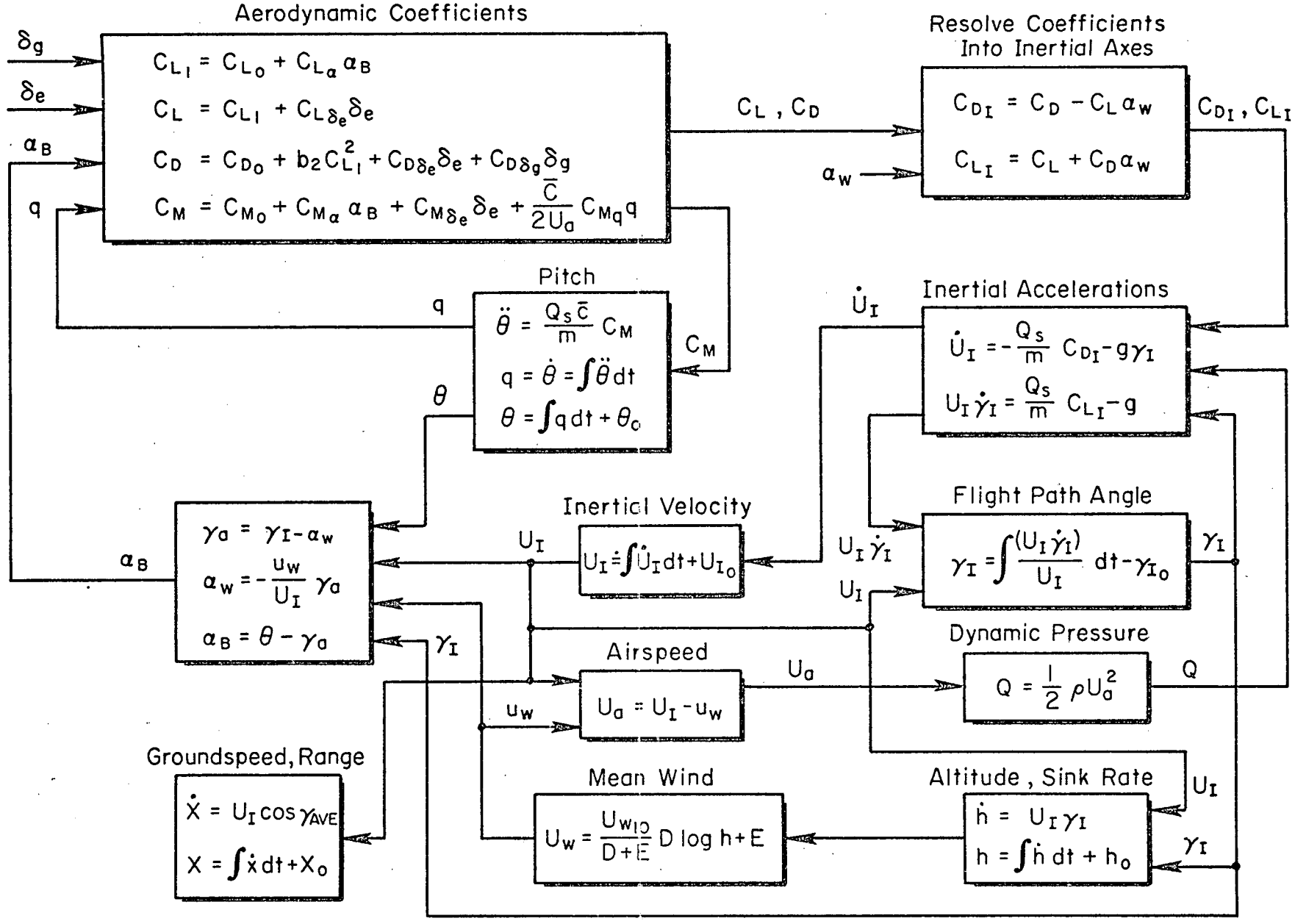

Figure 8. Analog Mechanization Diagram

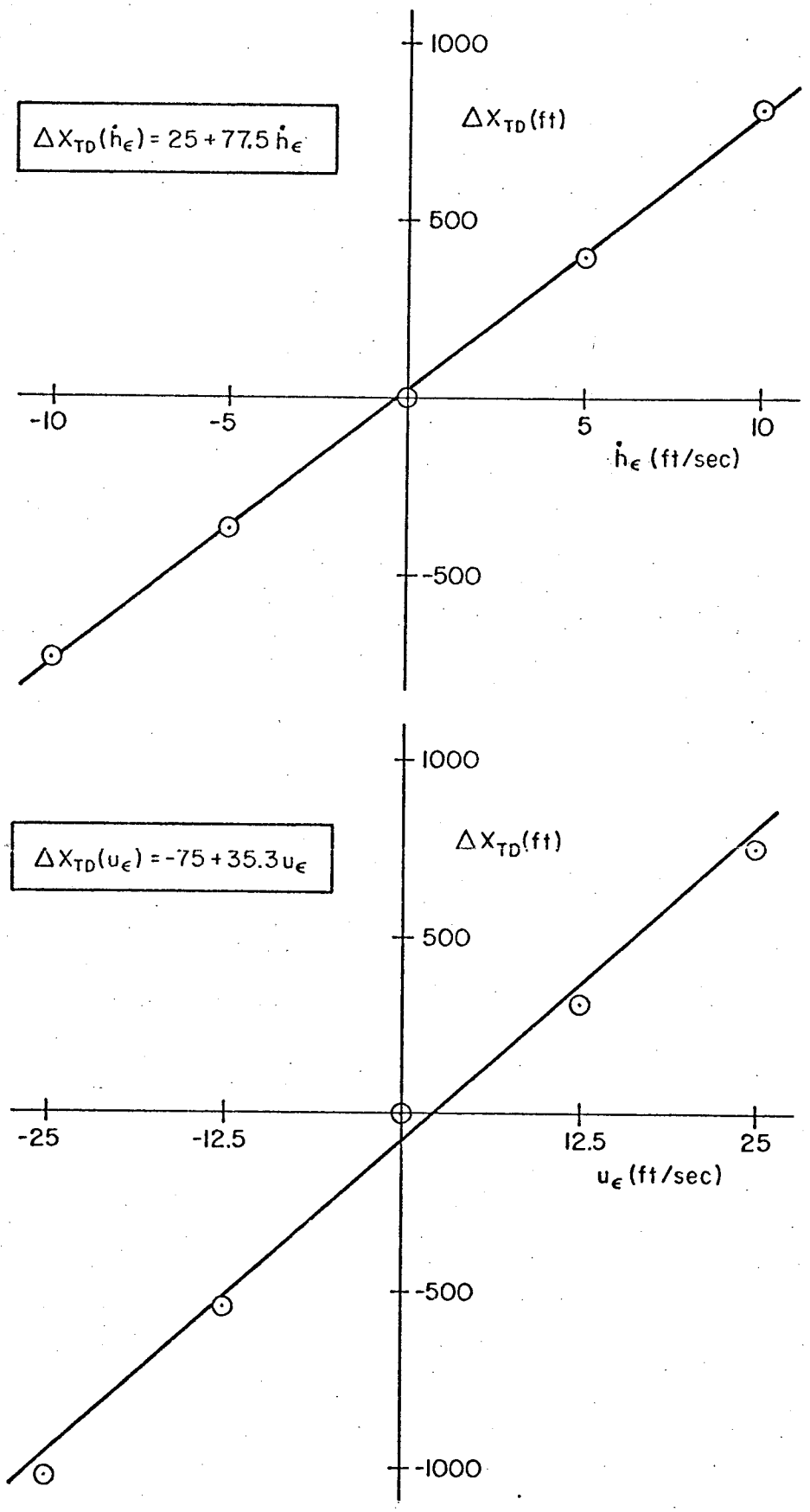

Figure 9. Mapping of Initial Conditions onto the Ground
a) ΔX_{TD} due to $\dot{h}_\epsilon$, u_ϵ

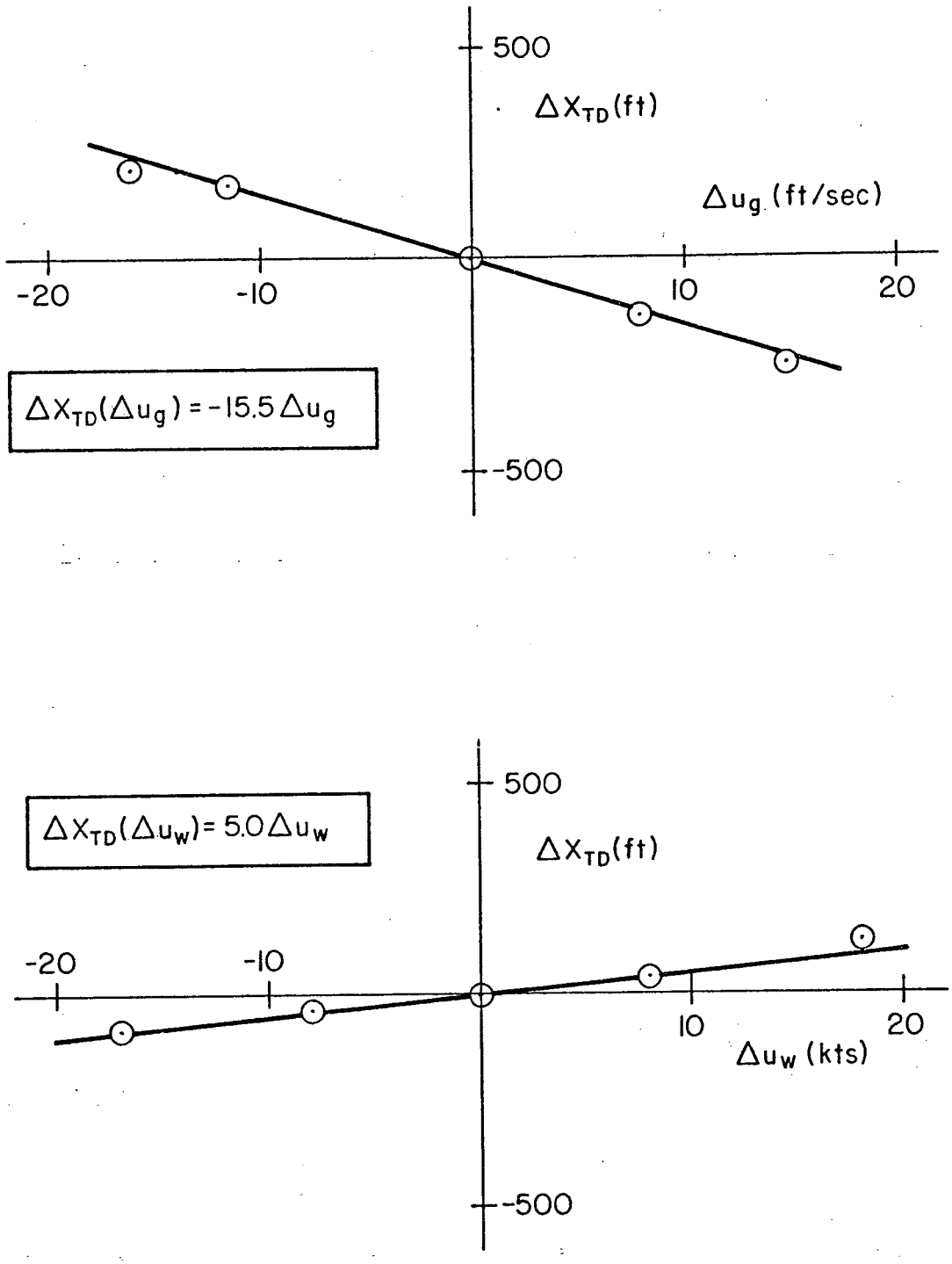

Figure 9. Mapping of Initial Conditions onto the Ground (continued)

b) ΔX_{TD} due to Δu_g, Δu_w

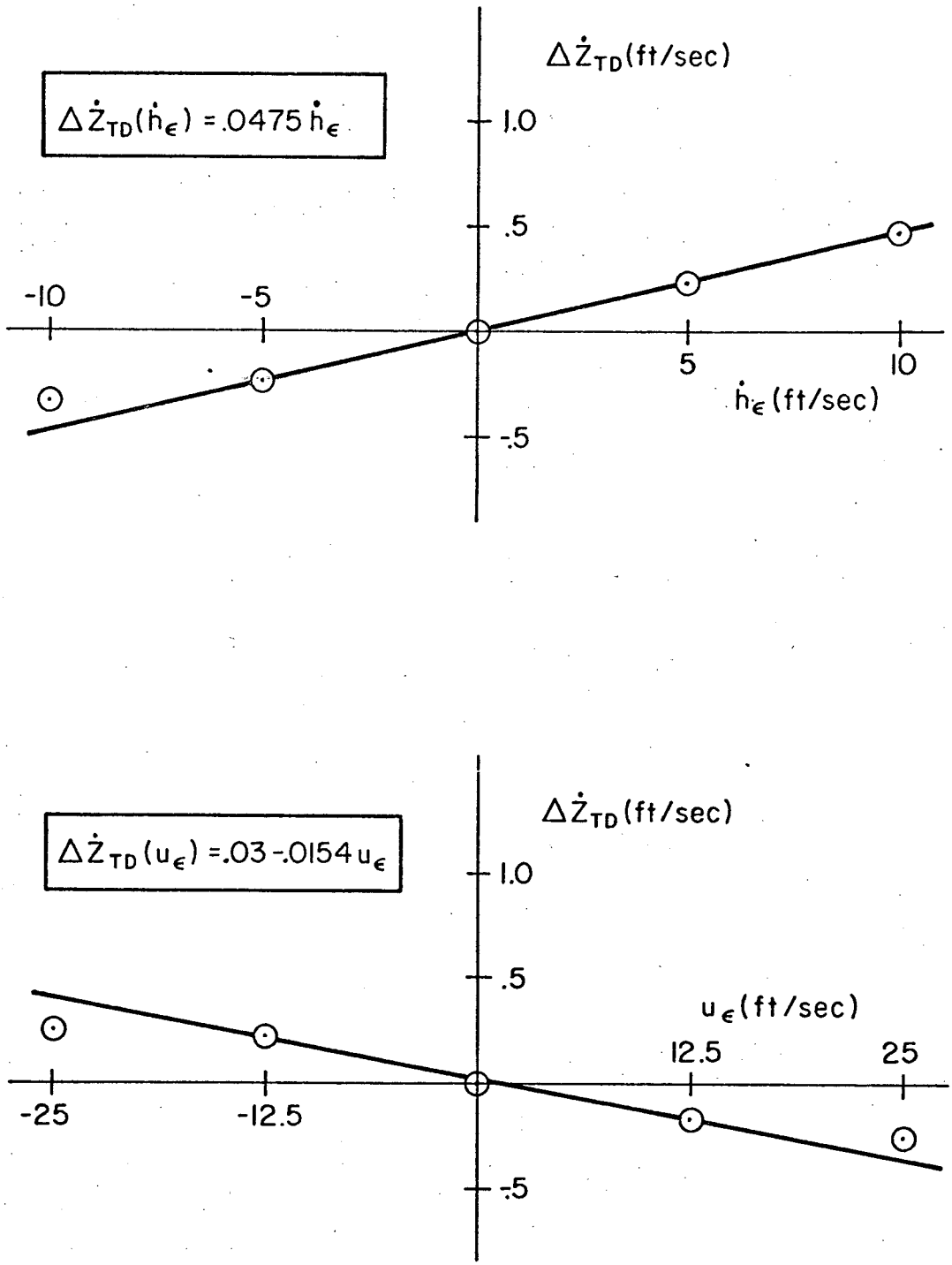

Figure 9. Mapping of Initial Conditions onto the Ground (continued)
c) $\Delta\dot{Z}_{TD}$ due to $\dot{h}_\epsilon$, u_ϵ

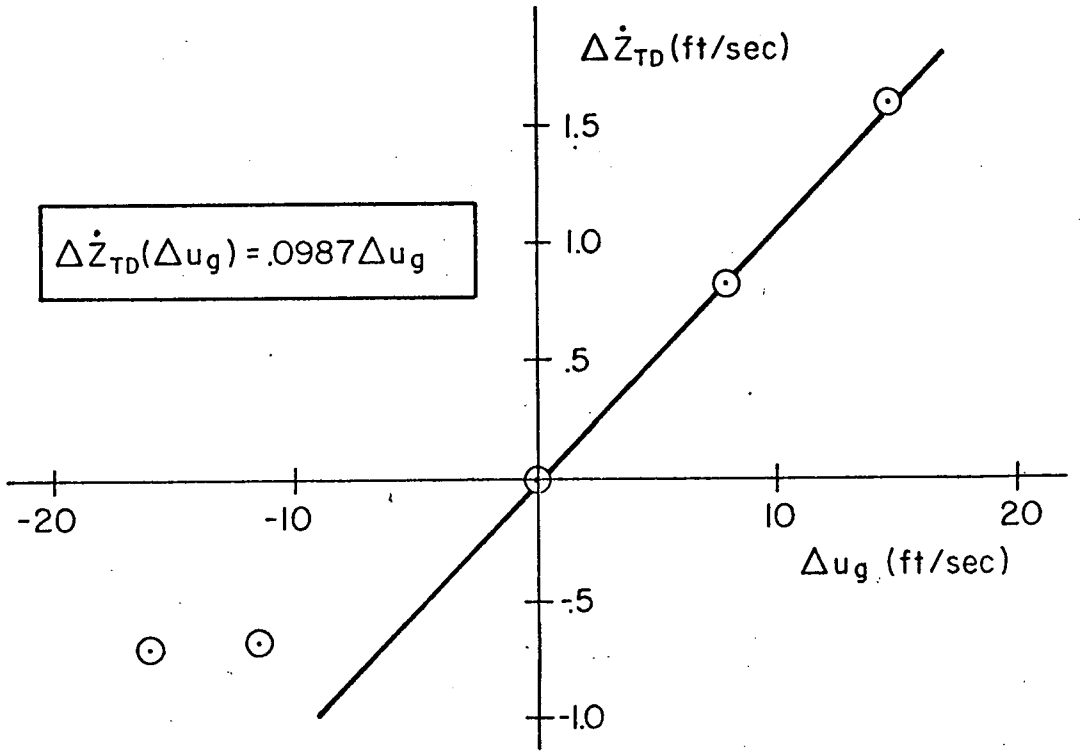

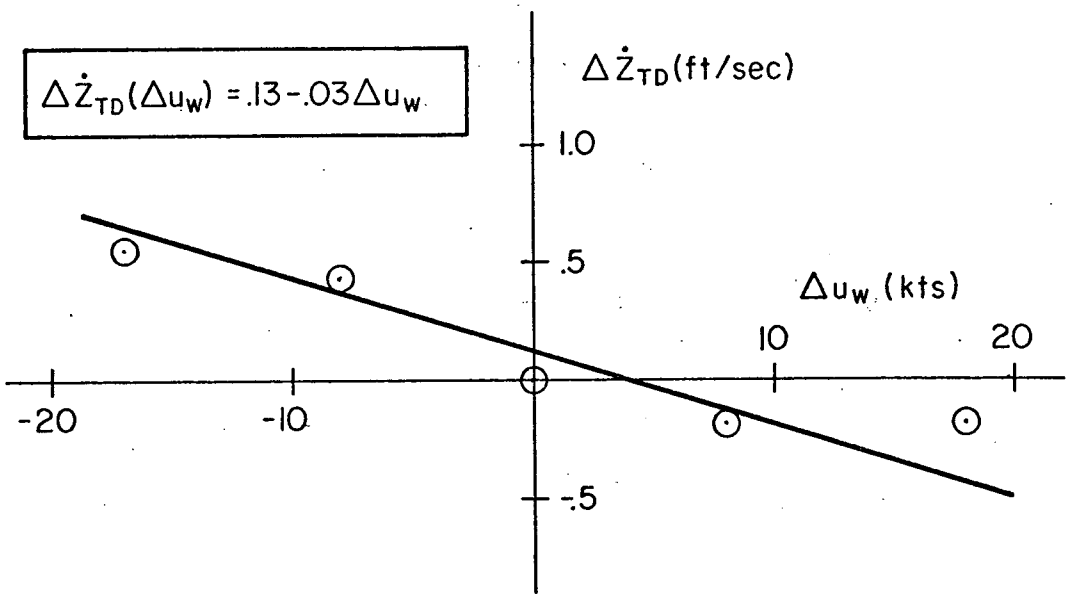

Figure 9. Mapping of Initial Conditions onto the Ground (continued)

d) $\Delta\dot{Z}_{TD}$ due to Δu_g, Δu_w

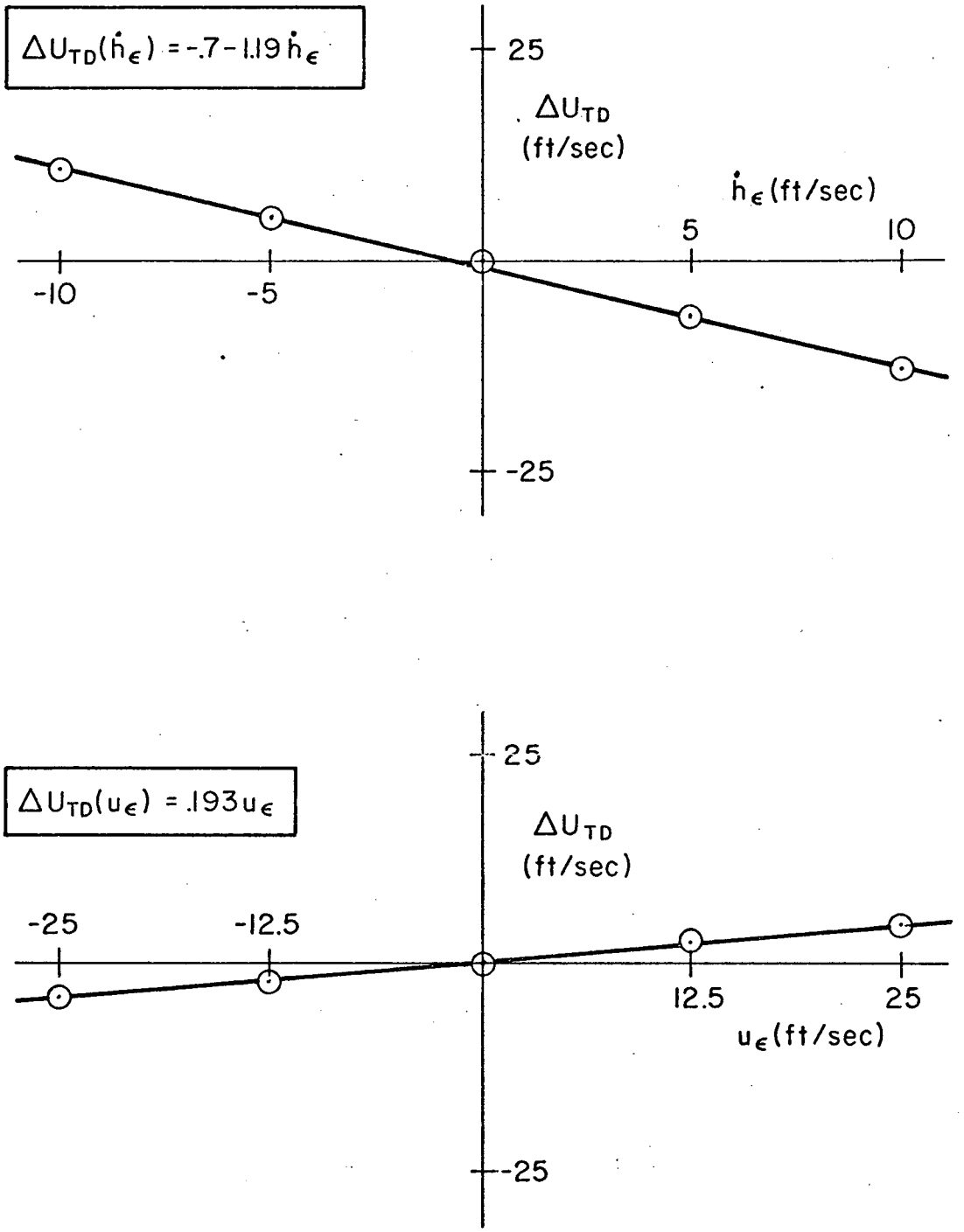

Figure 9. Mapping of Initial Conditions onto the Ground (continued)

e) ΔU_{TD} due to $\dot{h}_\epsilon$, u_ϵ .

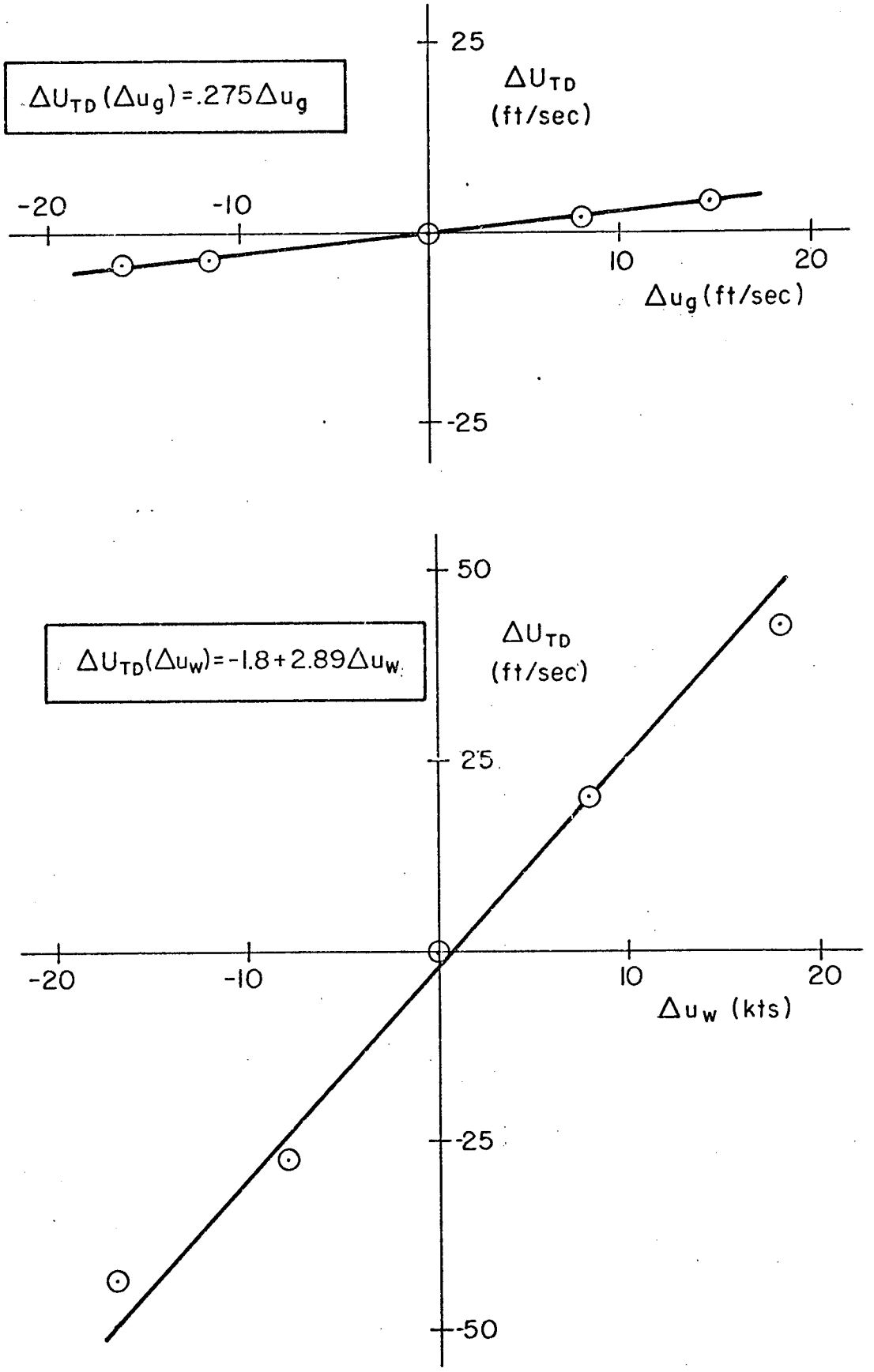

Figure 9. Mapping of Initial Conditions onto the Ground (continued)

f) ΔU_{TD} due to Δu_g, Δu_w

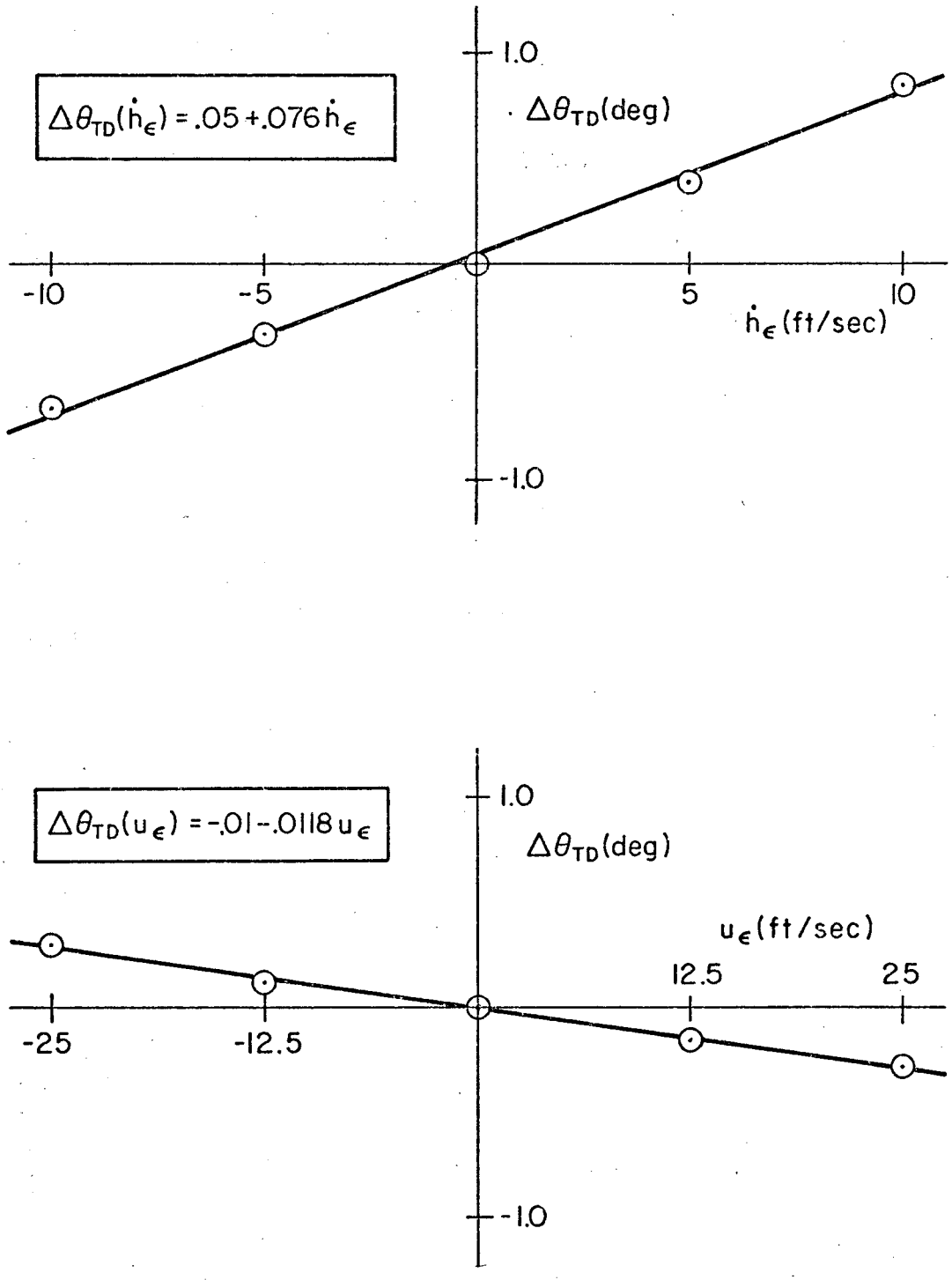

Figure 9. Mapping of Initial Conditions onto the Ground (continued)

g) $\Delta\theta_{TD}$ due to $\dot{h}_\epsilon$, u_ϵ

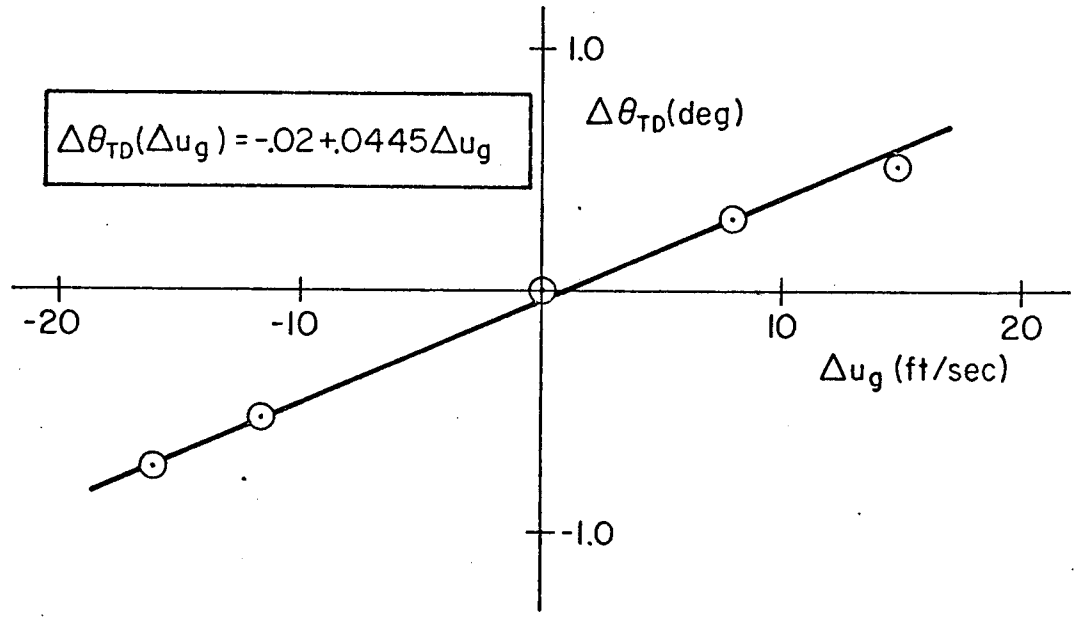

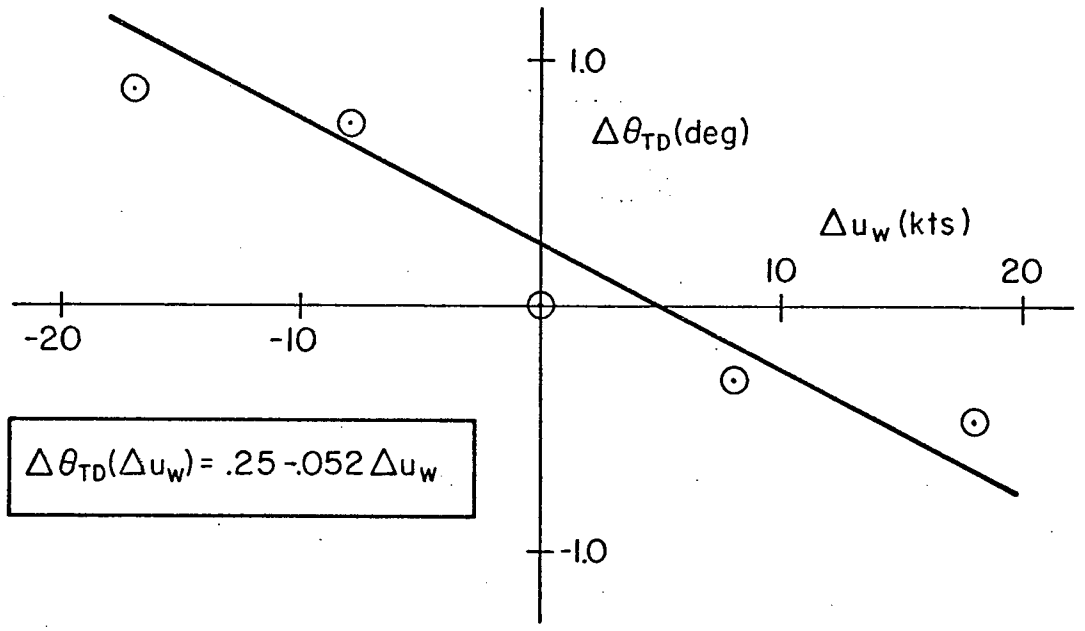

Figure 9. Mapping of Initial Conditions onto the Ground (concluded)
h) $\Delta\theta_{TD}$ due to Δu_g, Δu_w

Δu_g. However, this side of the curve is not of great significance because it doesn't tend to produce hard landings. Superposition of the effects of several inputs was verified as being valid. A summary of these linear fits is presented in Table 5 (which gives equations for the touchdown conditions as functions of the initial conditions and winds). Also included is the expression for stopping distance (X_{stop}). For the system considered, beam deviation (height) errors at the start of flare (h_ϵ) have an effect only on X_{TD} and X_{stop}. The effect is a translation in X by an amount equal to $h_\epsilon \cot \gamma$ (because there is no height error at the start of flare — only an X error).

TABLE 5

TOUCHDOWN DISPERSION EQUATIONS

$$X_{TD} = 1550 + 5.0\Delta u_w + 5.67h_\epsilon + 35.3u_\epsilon + 77.5\dot{h}_\epsilon - 15.5\Delta u_g$$

$$\dot{Z}_{TD} = 2.83 - 0.03\Delta u_w - 0.0154u_\epsilon + 0.0475\dot{h}_\epsilon + 0.0987\Delta u_g$$

$$U_{TD} = 297.5 + 2.89\Delta u_w + 0.193u_\epsilon - 1.19\dot{h}_\epsilon + 0.275\Delta u_g$$

$$\theta_{TD} = 11.86 - 0.052\Delta u_w - 0.0118u_\epsilon + 0.076\dot{h}_\epsilon + 0.0445\Delta u_g$$

$$X_{stop} = 7000 + \Delta X_{TD} + 33.25^{*}\Delta U_{TD}$$

$$= 7000 + 101\Delta u_w + 5.67h_\epsilon + 41.7u_\epsilon + 37.9\dot{h}_\epsilon - 6.4\Delta u_g$$

Units:	Δu_w,	kt	X_{TD},	ft
	u_ϵ,	ft/sec	$\dot{Z}_{TD}$,	ft/sec
	$\dot{h}_\epsilon$,	ft/sec	U_{TD},	ft/sec
	h_ϵ,	ft	θ_{TD},	deg
	Δu_g,	ft/sec	X_{stop},	ft

*This number is based on the assumption of a constant deceleration of 10 ft/sec^2 beginning 3.5 sec after touchdown.

3. Determination of Important Touchdown Variables

Now that the equations for the touchdown conditions have been determined, we need to find out which touchdown variables are important and which (if any) may be ignored. This is done by checking the variables (if any) in Table 5 that remain well within their respective acceptable regions when a worst-case input is applied. The worst-case input is approximated by the maximum wind magnitude and a 3σ gust level. RMS values for the touchdown variables are found via a technique described in the next subsection. The results are:

$$\sigma_{X_{TD}} \doteq 324 \text{ ft}$$

$$\sigma_{\dot{Z}_{TD}} \doteq 0.85 \text{ ft/sec}$$

$$\sigma_{\theta_{TD}} \doteq 0.47 \text{ deg}$$

$$X_{stop} \doteq 183 \text{ ft}$$

In Table 1 the limiting acceptable values for each variable were given. Combining these with the nominal values from Table 5 gives a margin for each variable. These are

$$M_{X_{TD}} = 750 \text{ ft}$$

$$M_{\dot{Z}_{TD}} = 3.2 \text{ ft/sec}$$

$$M_{\theta_{TD}} = 3.1 \text{ deg}$$

$$M_{X_{stop}} = 2200 \text{ ft}$$

Decreasing these margins to account for the effect of $\Delta u_w = \pm 18$ kt, and then dividing the modified margins by the rms values leads to a rough idea of the likelihood of each variable exceeding its margin (for the given worst-case input). Thus,

$$\frac{M'_{X_{TD}}}{\sigma_{X_{TD}}} \doteq \frac{660}{324} \doteq 2.0$$

$$\frac{M'_{\dot{Z}_{TD}}}{\sigma_{\dot{Z}_{TD}}} \doteq \frac{2.7}{0.85} \doteq 3.2$$

$$\frac{M'_{\theta_{TD}}}{\sigma_{\theta_{TD}}} \doteq \frac{2.2}{0.47} \doteq 4.7$$

$$\frac{M'_{X_{stop}}}{\sigma_{X_{stop}}} \doteq \frac{382}{183} \doteq 2.1$$

For a Gaussian distribution (which applies to this case because it has a given u_w and σ_{u_g}) the probability of exceeding the margin when $M'/\sigma = 2$ is about 0.046. For $M'/\sigma = 3$ the probability drops to about 0.0027; and for $M'/\sigma = 4$ it drops to about 0.00006. Thus the probability of the pitch attitude at touchdown exceeding its maximum acceptable value is insignificant compared with the probability of X_{TD} being outside the ±750 ft acceptable window.

Although all of the probabilities may be small, here we are only concerned with relative likelihoods. We are merely determining which variables to consider further. Based on the above results, the conclusion is to consider X_{TD}, $\dot{Z}_{TD}$, and X_S.

C. COMPUTATION PROCEDURE

The computations are best explained by considering an example case. For the example chosen (X_{TD}), the dispersion equation given in Table 5 is of the form,

$$X_{TD} = X_{TD_o} + A\Delta u_w + Bh_\epsilon + Cu_\epsilon + D\dot{h}_\epsilon + E\Delta u_g \qquad (13)$$

where A, B, C, D, E are known constants. The right side of this equation can be broken into three parts using the following definitions.

$$X_{TD_1} \equiv X_{TD_o} + A\Delta u_w \qquad (14)$$

and,

$$h_1 \equiv Bh_\epsilon + Cu_\epsilon + D\dot{h}_\epsilon \qquad (15)$$

Thus,

$$X_{TD} = X_{TD_1} + h_1 + E\Delta u_g \tag{16}$$

The logic behind grouping the terms this way is simple. For a given wind profile, X_{TD_1} is a constant. For a given Gaussian gust environment, both h_1 and $E\Delta u_g$ are Gaussian (with zero means) and independent. Further, both h_1 and $E\Delta u_g$ have rms values* that are proportional to σ_g.† Therefore, for a given wind profile and rms gust level, X_{TD} has a Gaussian distribution with a mean given by

$$\mu_{X_{TD}} = X_{TD_1} \tag{17}$$

and an rms value given by

$$\sigma_{X_{TD}} = \sqrt{\sigma_{h_1}^2 + E^2\sigma_{\Delta u_g}^2} \tag{18}$$

or,

$$\sigma_{X_{TD}} = B_2\sigma_g \tag{19}$$

With the wind profile and gust level specified, the distribution of X_{TD} is actually a conditional distribution. As noted above, this conditional distribution is Gaussian. However, as will be shown later, the overall distribution of X_{TD} is not Gaussian. This is pointed out here to emphasize the fact that Gaussian gusts and a set of linearized touchdown relations do not necessarily produce a Gaussian distribution for touchdown dispersions. One reason for this is that the rms gust level is not a constant, but is itself a random variable (with a Rayleigh distribution).

With a Gaussian conditional probability density distribution for X_{TD}, it is a simple matter to compute the conditional probability of a successful touchdown. The unshaded area in Fig. 10 represents this conditional

---

*Because h_1 is a linear sum of perturbation variables, an auxiliary equation can be used in the matrix of perturbation equations of motion to obtain transfer functions for h_1 to u_g and w_g inputs directly. Then σ_{h_1} can be found (for a given σ_{u_g}) via the technique described earlier.

†In this derivation σ_{u_g} will be called σ_g to simplify the notation.

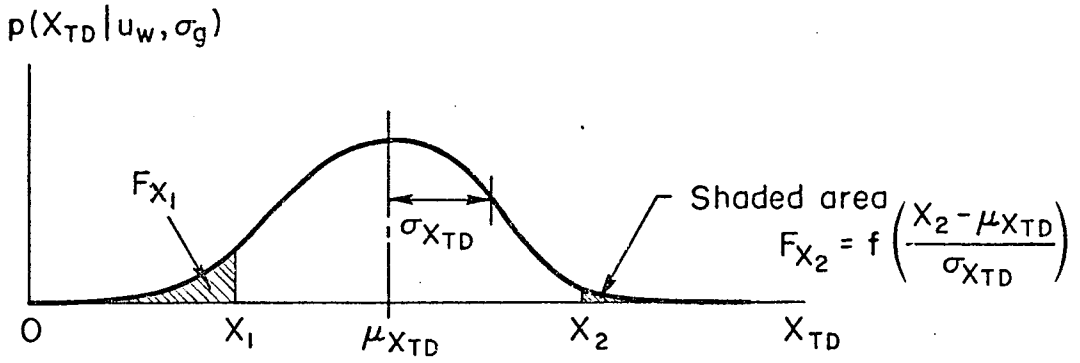

Figure 10. Conditional Probability Density Distribution for X_{TD}

probability. Thus the conditional probability of a successful touchdown (given u_w and σ_g) is:*

$$P(X_{TD} \in X_S | u_w, \sigma_g) = 1 - F_{X_1} - F_{X_2} \tag{20}$$

This conditional probability can be multiplied by the probability density distribution of u_w, and integrated over all u_w to give another conditional probability; one that depends only on σ_g. (A rough plot of the probability density distribution of u_w was given in Fig. 2.) Thus the conditional probability of a successful touchdown (given σ_g) is,

$$P(X_{TD} \in X_S | \sigma_g) = \int_{-\infty}^{\infty} P(X_{TD} \in X_S | u_w, \sigma_g) p(u_w) du_w \tag{21}$$

With the conditional probability a function of only one variable (σ_g) it can be plotted to show the effect gust level has on touchdown conditions. Such a plot looks like that shown in Fig. 11.

*The notation used in this equation is read as follows. "The Probability of X_{TD} belonging to the successful range of X_{TD}, given u_w and σ_g, is $1 - F_{X_1} - F_{X_2}$." The symbol X_S is used to denote the successful range of X_{TD}.

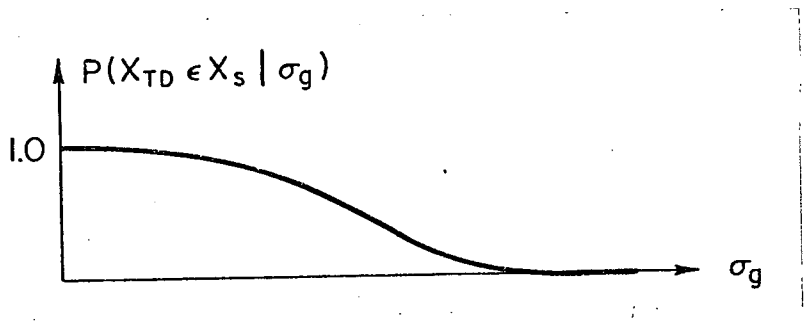

Figure 11. Conditional Probability of a Successful Touchdown as a Function of RMS Gust Level

It remains now only to multiply this conditional probability by the probability density distribution of σ_g, and integrate over all σ_g to obtain a number for the overall probability of a successful touchdown (i.e., be within X_{TD} limits). This is shown in the next equation.

$$\underbrace{P(X_{TD} \in X_S)}_{\substack{\text{Probability of} \\ \text{a successful} \\ \text{touchdown}}} = \int_0^\infty P(X_{TD} \in X_S \mid \sigma_g) p(\sigma_g) d\sigma_g \qquad (22)$$

The above explanation considers only one way to carry out the required calculations. It is also possible to carry out the various integrations in a different order to end up with the last integration over X. Then the overall probability density distribution of X_{TD} becomes available (rather than a conditional version) as shown in Fig. 12, and discussed below.

D. TOUCHDOWN DISTRIBUTIONS

Figure 12 shows a plot of the overall probability density distribution for X_{TD}. The cumulative area under the curve (integrating from right to left) represents the probability of exceeding any given value of X_{TD}. This exceedance probability is shown plotted on probability paper in Fig. 13 to show that the distribution of X_{TD} is not Gaussian. Gaussian distributions plot as straight lines on probability paper. In particular, it can be seen in Fig. 13 that a Gaussian distribution would underestimate the probability

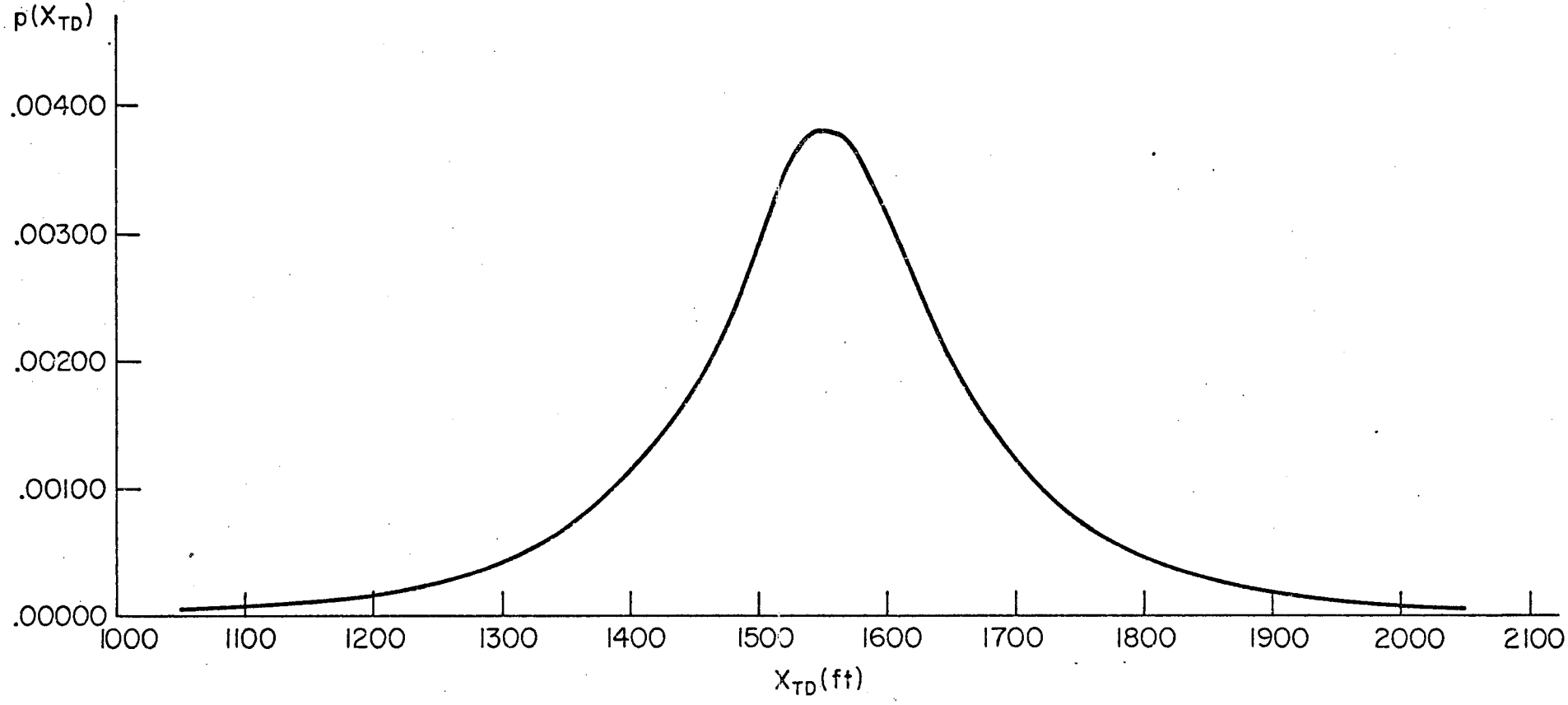

Figure 12. Probability Density Distribution for X_{TD}

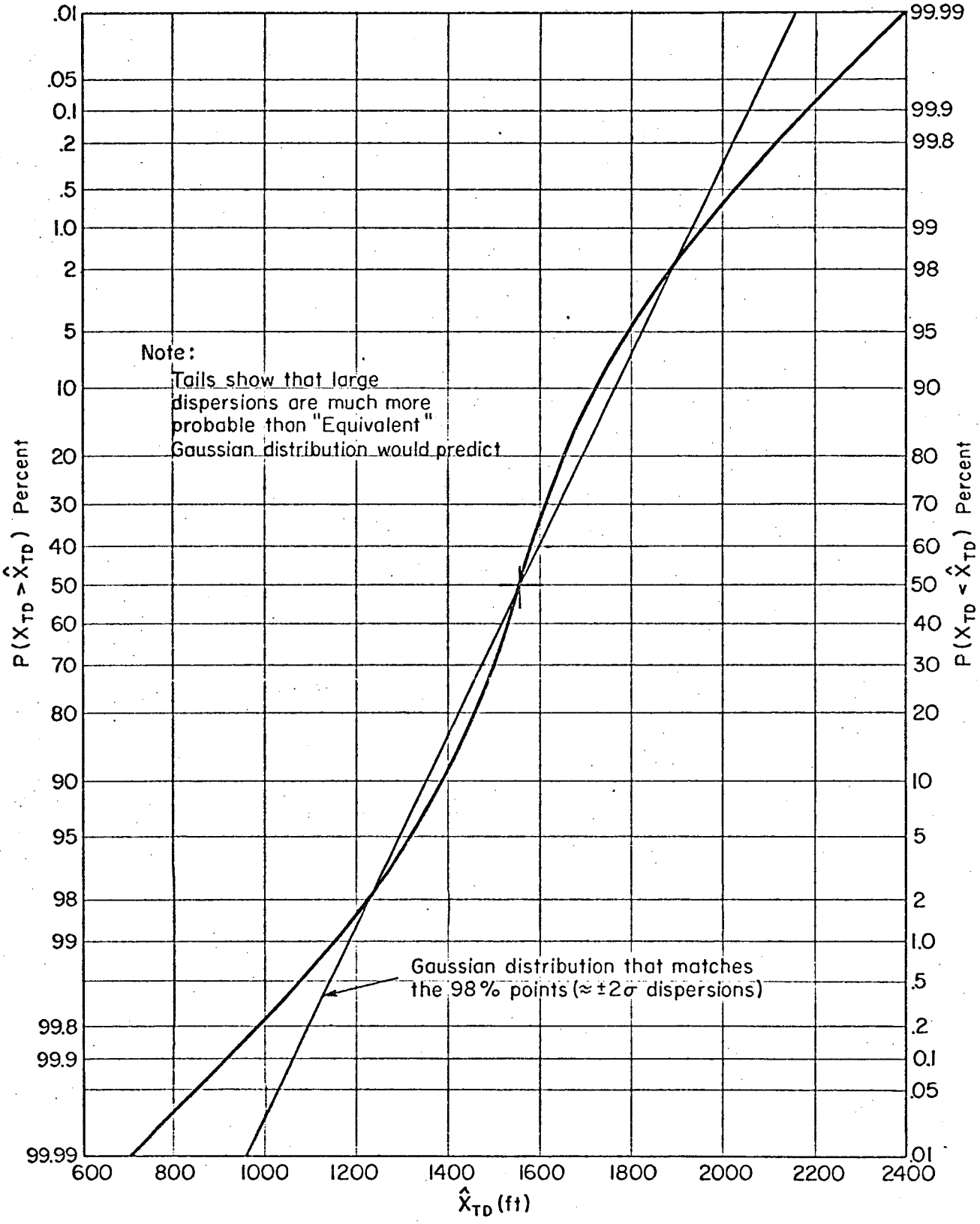

Figure 13. Exceedance Probability of X_{TD}

of very large dispersions from the mean. This is an encouraging result because measured data commonly give more large dispersions from the mean than would be predicted by a Gaussian distribution that matches the mean and variance.

A plot of the probability density distribution for sink rate at touchdown is presented in Fig. 14, and the associated exceedance probability is in Fig. 15. Plots of stopping distance (X_{stop}) probabilities are not included because the probabilities turned out to be significantly smaller than those for X_{TD} and $\dot{Z}_{TD}$. This was a surprise since the value of M'/σ was not large. It turns out that the computed value of M'/σ is misleading because the probability of the 18 kt Δu_w that was used is nil. Had a 0.3 percent value of Δu_w been used, then M'/σ would have been about 4.3, which is a more accurate representation of the relative importance of X_{stop}. In any event, this points out the fact that X_{stop} is sensitive to tailwinds for the example system.

E. PROBABILITIES OF EXCEEDING TOUCHDOWN WINDOWS

From the distributions of touchdown conditions it is found that the acceptable touchdown windows are large compared to the expected touchdown dispersions. Clearly, this is desirable for an acceptable system. From Fig. 13 the probability of exceeding the allowable X_{TD} window is found to be:

$$P(X_{TD} < 800 \text{ ft}) + P(X_{TD} > 2300 \text{ ft}) \doteq 600 \times 10^{-6}$$

The probability of exceeding the touchdown sink rate limit of 6 ft/sec does not fall within the bounds of the plot in Fig. 15. However, the probability was computed to be:

$$P(\dot{Z}_{TD} > 6 \text{ ft/sec}) \doteq 3 \times 10^{-6}$$

These numbers make it obvious that short and long landings are much more likely than a hard landing for the example system. Therefore, a system improvement could be made by reducing the X_{TD} exceedances at the expense of larger $\dot{Z}_{TD}$ dispersions.

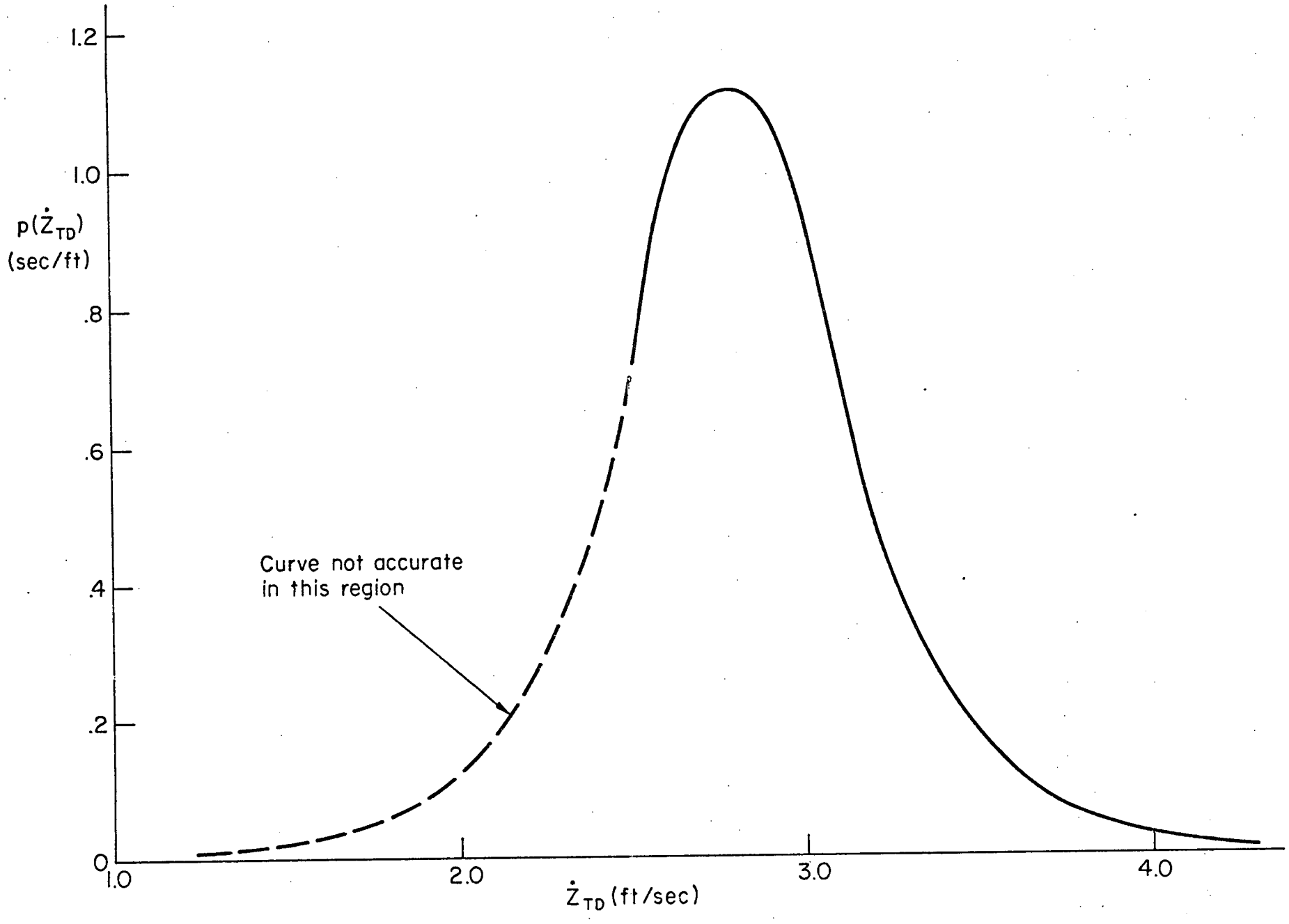

Figure 14. Probability Density Distribution for Sink Rate at Touchdown

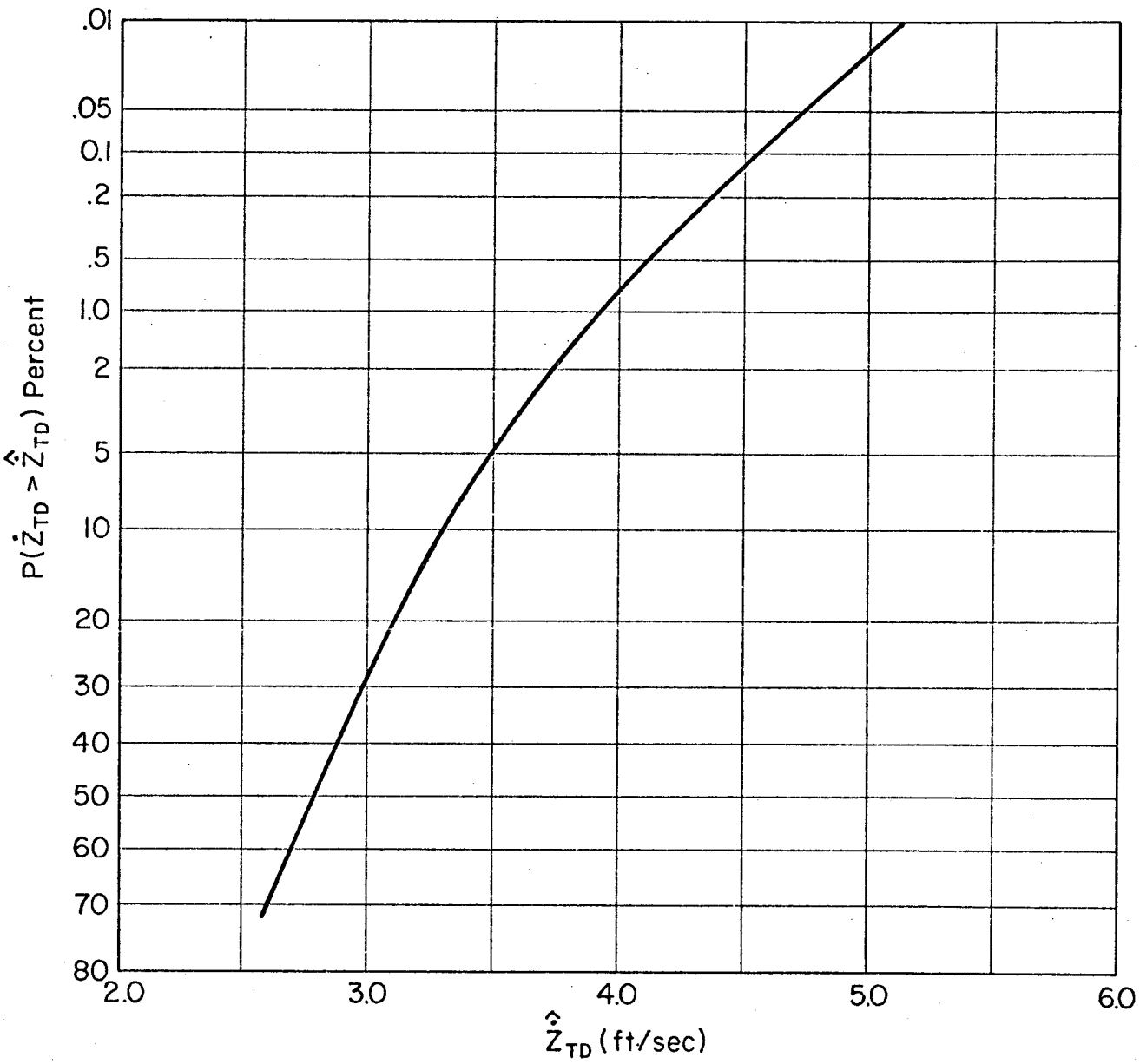

Figure 15. Exceedance Probability for $\dot{Z}_{TD}$

A few comments on the primary causes of the touchdown dispersions are pertinent here. Using the equations in Table 5 and the computed vehicle dispersions at the start of flare indicates that $\Delta\dot{Z}_{TD}$ comes mainly from Δu_g, while ΔX_{TD} depends strongly on sink rate at the start of flare, and does <u>not</u> depend very strongly on Δu_g. Thus, in addition to defining the main sources of dispersion, this shows that the important touchdown dispersions will be largely uncorrelated.

F. COMMENTS AND CONCLUSIONS REGARDING ONE-STEP FLARE EXAMPLE

- Although not mentioned earlier, it was found that the speed during preflare glide must be considerably higher than the speed for maximum L/D in order to provide an adequate margin for increasing L/D when a large headwind is present. In terms of flight path angle, our preliminary calculations indicate a descent angle of at least 9 deg is required.

- To achieve reasonable touchdown conditions in the presence of winds, some form of speed control is required. Varying the height for lowering the landing gear as a function of expected speed error at touchdown (similar to what was done for the example system) is a simple way to reduce speed errors to acceptable values.

- The variables that had the most effect on touchdown conditions for our example system were head- and tailwinds, and speed and sink rate prior to flare.

- The computed distributions of touchdown conditions showed the tails to be significantly larger than those of equivalent Gaussian distributions. As a consequence, equivalent Gaussian distributions would appreciably underestimate the probability of large disperions from the mean.

- For large tailwinds, the probability of running off the far end of the runway goes up very rapidly. The reason the computed probability of exceeding the acceptable stopping distance was not large is that the given wind model provides a negligible probability for tailwinds over about 8 kt.

- By simulating the entire nonlinear situation on the analog computer, and then using the empirical (measured) results in the way discussed, it was possible to make use of very powerful linear analysis techniques that otherwise would not have been applicable.

SECTION IV

TWO-STEP FLARE APPLICATION

This section presents the results of an analysis of Bell Aerospace Corporation's two-step flare and decrab control system for the North American Rockwell high cross-range space shuttle orbiter vehicle. Figure 16 presents a side view of the two-step flare trajectory, showing the initial flare (from an equilibrium glide), the constant flight-path angle glide phase, and the final flare to touchdown. With a sufficiently long glide phase (of the order of 15 sec or more) it is not necessary to consider the effects of the initial flare on the distributions at the start of final flare (because all transients have had time to die out). This is the case with Bell's guidance strategy. Thus we need only consider the glide and final flare flight segments in our analysis (except when determining the effects due to various mean wind profiles). This reduces the two-step flare analysis to an effective one-step flare. Therefore, rather than repeating a description of all the steps in the analysis, only the results will be presented.

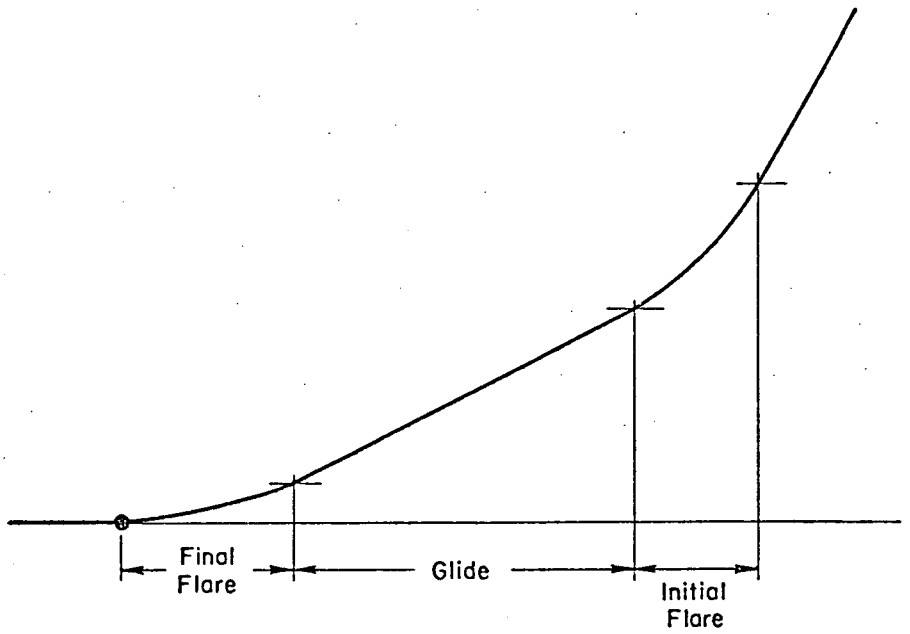

Figure 16. Side View of Two-Step Flare Trajectory

Included as Fig. 17 are the longitudinal and lateral block diagrams for Bell's control system (Ref. 6). Figure 18 then presents the results of mapping the conditions just prior to final flare onto the ground. Discussion of Figs. 17 and 18 is limited to only the following two comments because the results are the same as were found previously for the one-step flare. First, it is pointed out that linear fits to the touchdown conditions are very good representations of system sensitivities. And second, the variable Δh_{FF} is included to show the effect of perturbations in the altitude at which final flare is initiated. One further comment should be made here. This is that Bell ran their Monte Carlo runs in two separate series; one with a scanning beam landing guidance system, and the other with a tracking radar for landing guidance information. In most variables both systems gave essentially the same results. For these variables we took the liberty of combining the separate results to obtain a single combined result. However, for those variables that showed a significant difference for the two systems, we accordingly made separate comparisons.

The primary results to be discussed in this section are the comparisons of Bell's and STI's distributions of pertinent variables just before final flare, just before decrab, and at touchdown. It was decided to apply the approach and landing model at these discrete points so that any significant differences in touchdown distributions (<u>if</u> they occurred) might be traced back up the approach trajectory to determine their origin and causes. However, our preliminary calculations showed no great differences with Bell's results. Thus, the primary purpose of the multiple-point comparisons had been obviated. As a consequence, we expended only a limited effort on the computations of the distributions <u>prior</u> to touchdown, which resulted in some of the variables being compared via plots of the distributions, and others being compared on the basis of the rms values of the dispersions.

A. COMPARISONS JUST PRIOR TO FINAL FLARE

X_{FF}

On Bell's Monte Carlo runs a one-second sampling time was used for printing out the pertinent variables. Because the ground speed just prior to final flare is about 325 ft/sec, a one-second sampling time introduces a

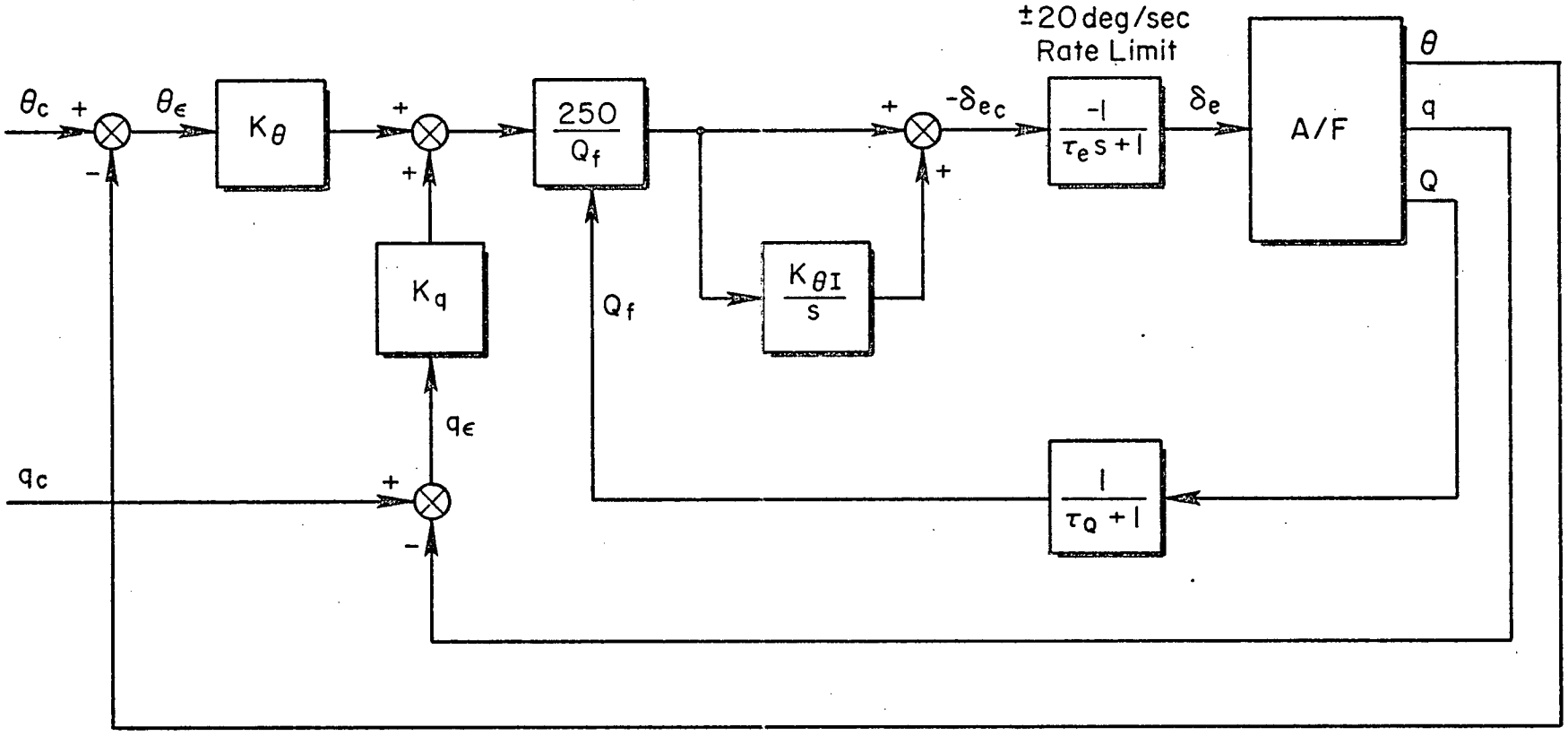

Note: Elevon hard and soft position limits are omitted in this model

PARAMETERS

K_θ = 3.0
K_q = 1.2 sec
K_{QI} = .2/sec
τ_Q = 2.5 sec
τ_e = 0.05 sec

Figure 17a. Bell Pitch Control System and Elevon Actuator Model

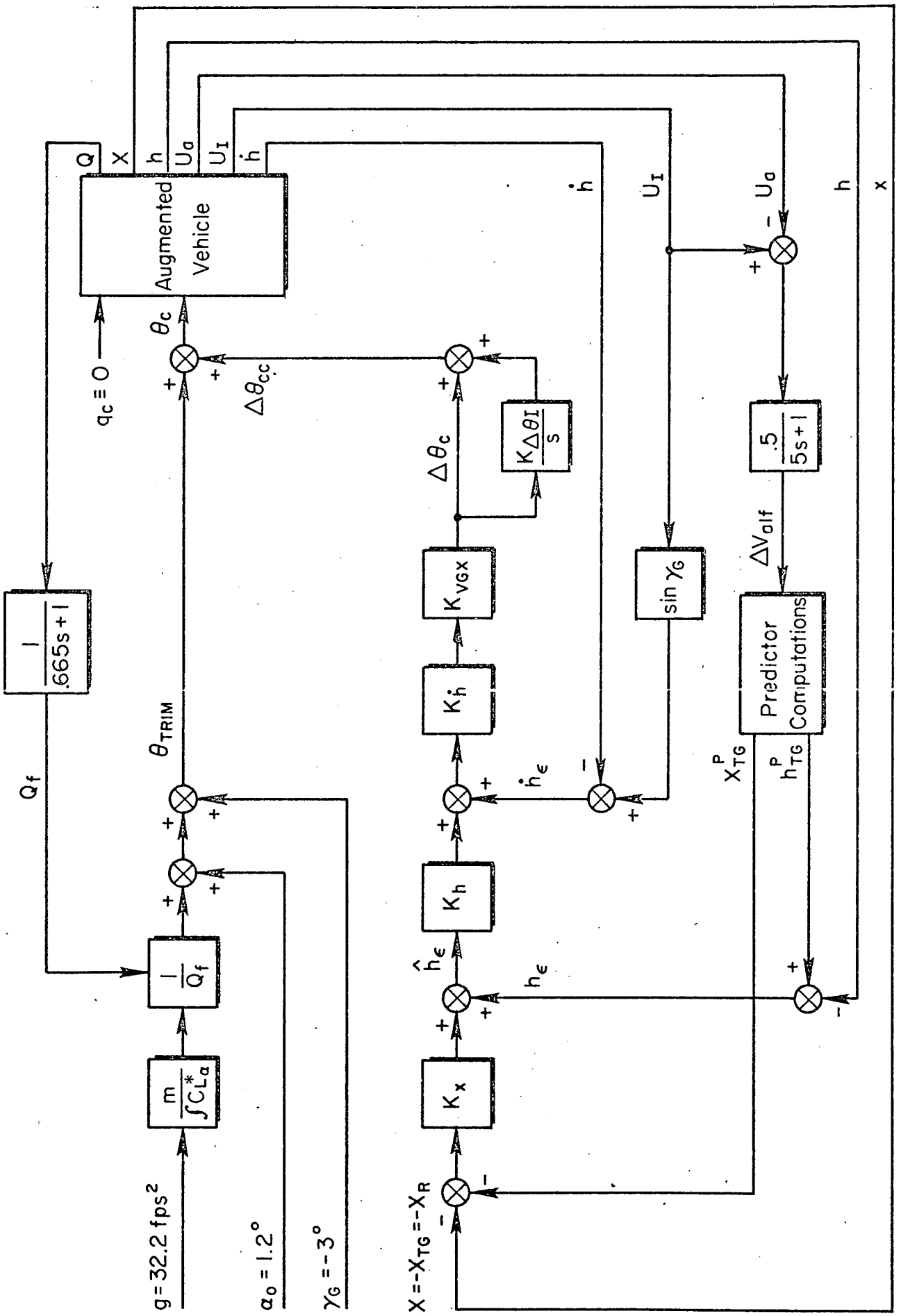

Figure 17b. Bell Shallow-Glide Guidance Model

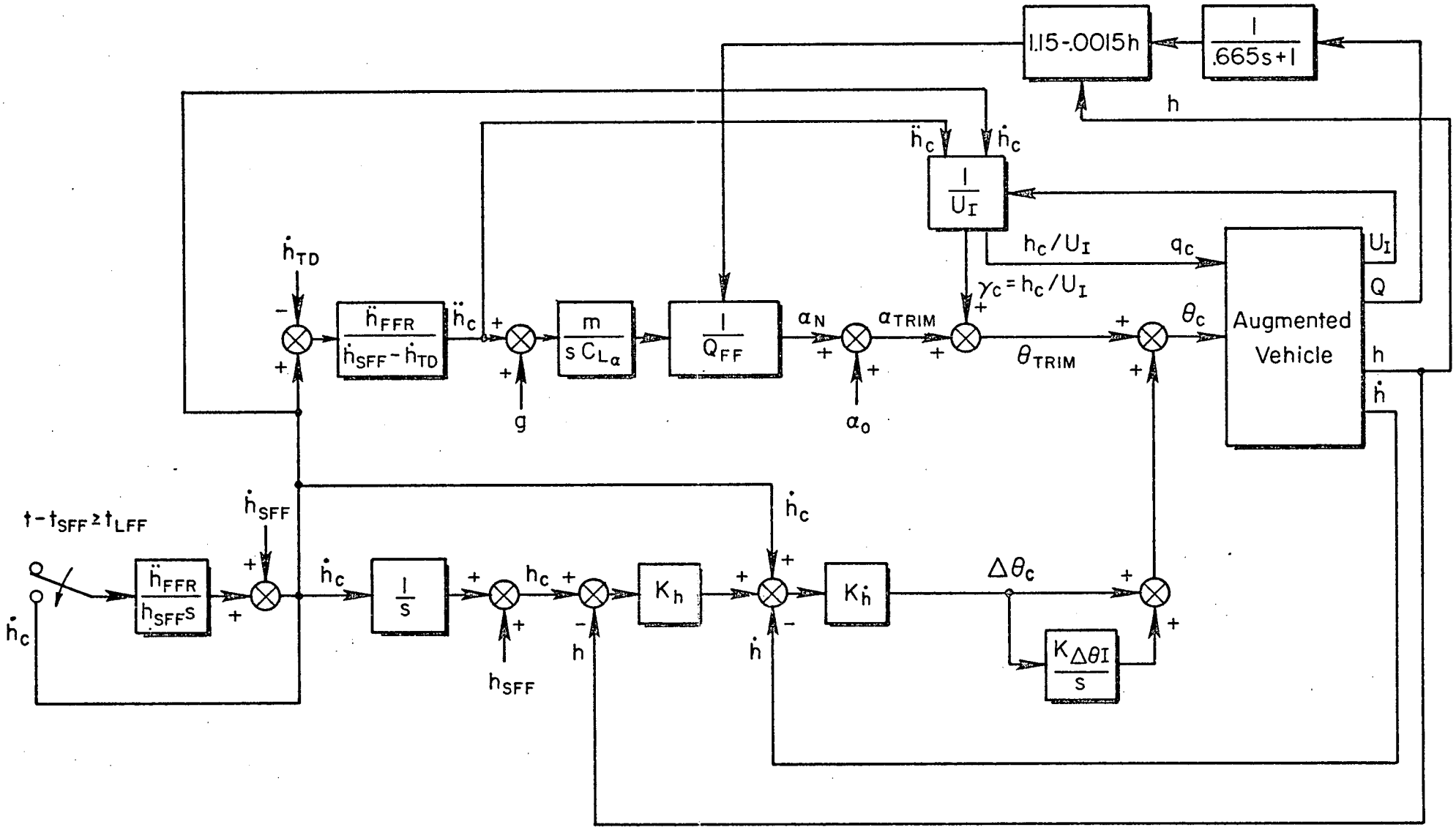

PARAMETERS

$g = 32.2\ ft/sec^2$ $\quad C_{L_\alpha} = .026/deg$

$m = 6630\ Slugs$ $\quad \alpha_o = 2.2\ deg$

$s = 6084\ ft^2$ $\quad \dot{h}_{TD} = -3.0\ ft/sec$

$K_h = 1.5/sec$, $K_{\dot{h}} = .133\ deg/ft/sec$, $K_{\Delta\theta I} = .01/sec$

AT-FLARE-FROZEN PARAMETERS

(Nominal Case Values)

$t_{LFF} = 1.0\ sec$ $\quad \dot{h}_{SFF} = -17.4\ ft/sec = \dot{h}_o$

$h_{SFF} = 101.55\ ft = h_o$ $\quad \ddot{h}_{FFR} = 3.0\ ft/sec^2$

Figure 17c. Bell Flare Guidance System Model

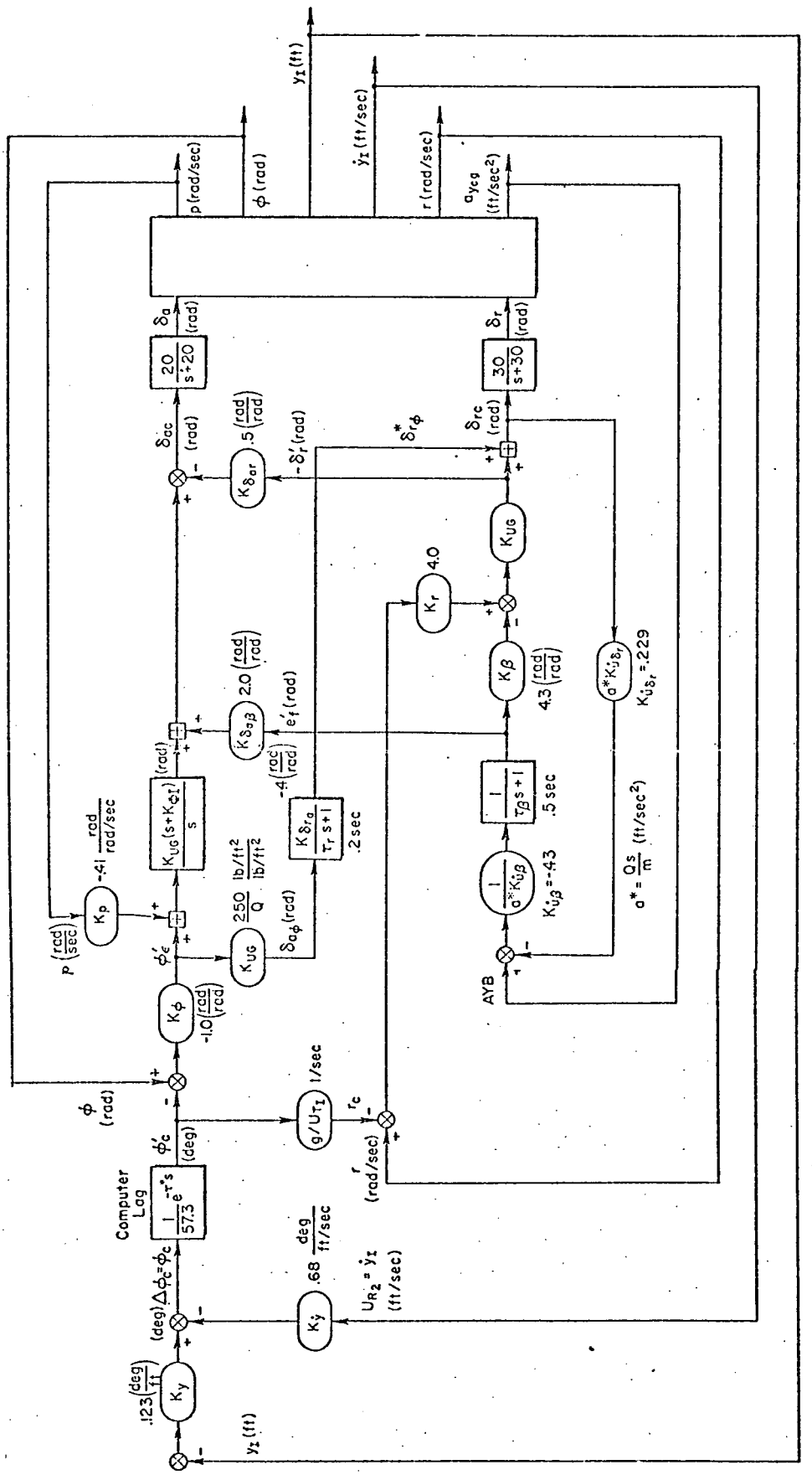

Figure 17d. Bell Lateral Control System (Prior to Decrab)

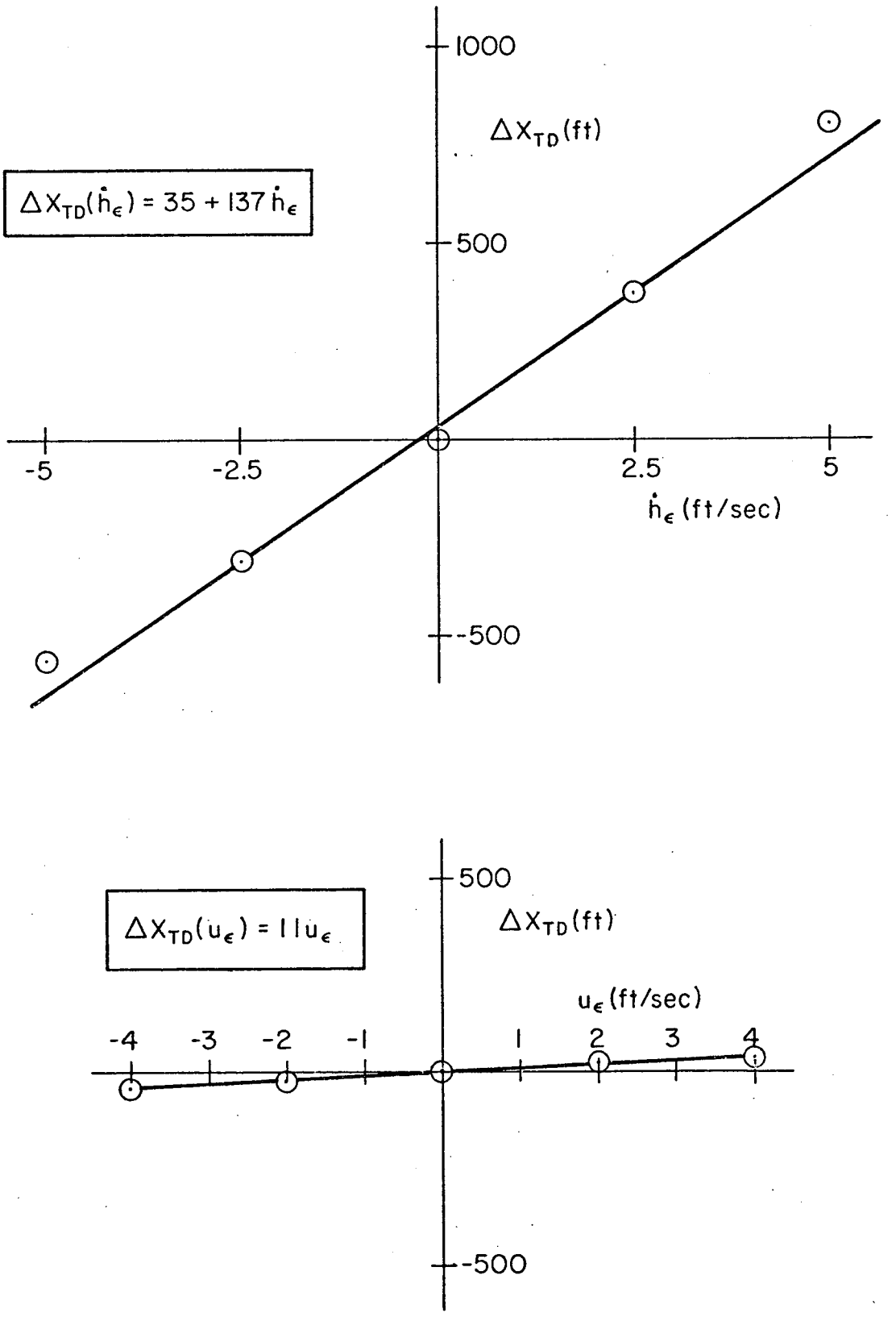

Figure 18. Mapping of Initial Conditions onto the Ground

a) ΔX_{TD} Due to $\dot{h}_\epsilon$, u_ϵ

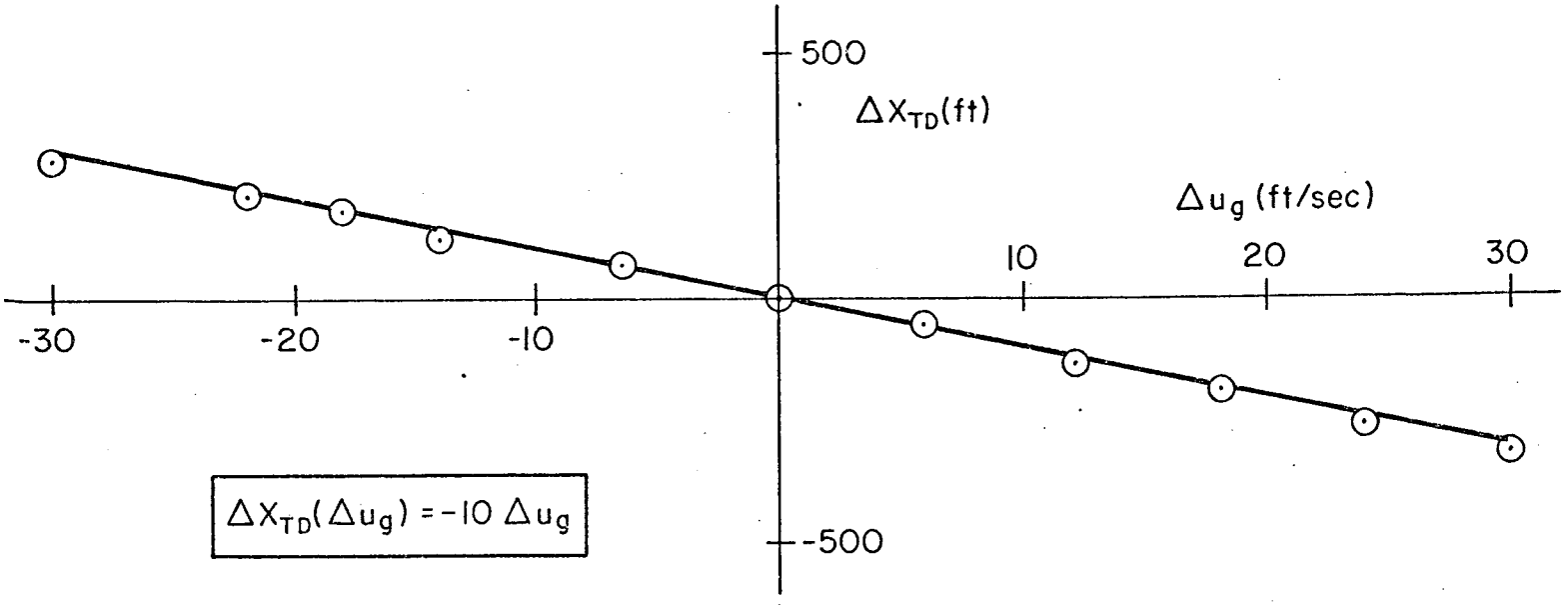

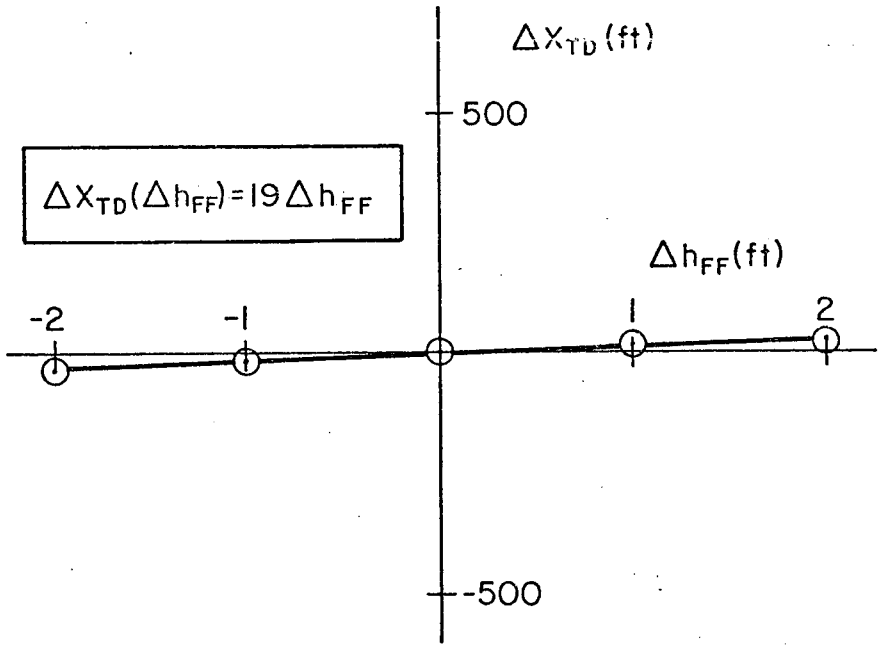

Figure 18. Mapping of Initial Conditions onto the Ground (continued)

b) ΔX_{TD} due to Δu_g, Δh_{FF}

C.2

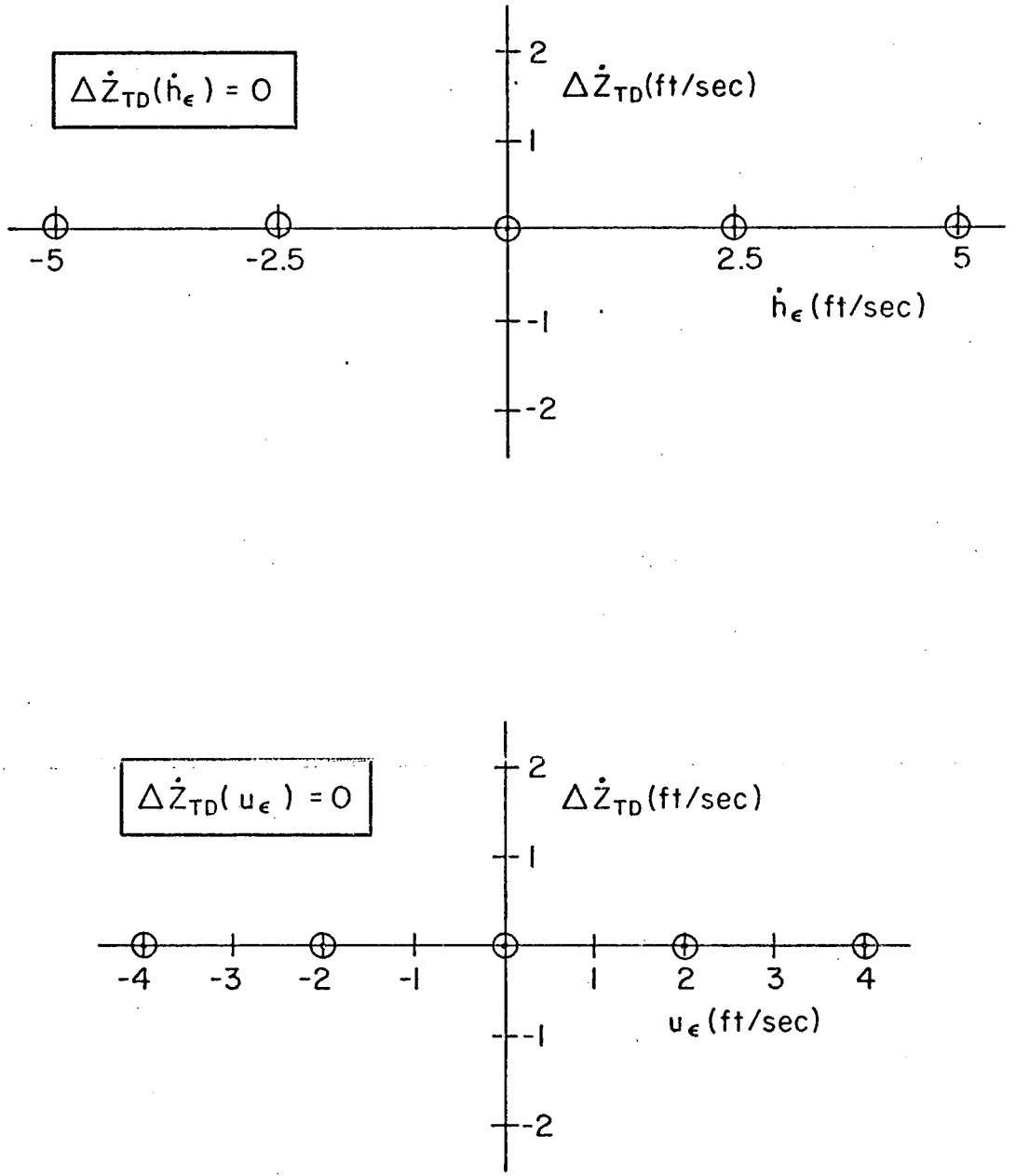

Figure 18. Mapping of Initial Conditions onto the Ground (continued)
c) $\Delta\dot{Z}_{TD}$ due to $\dot{h}_\epsilon$, u_ϵ

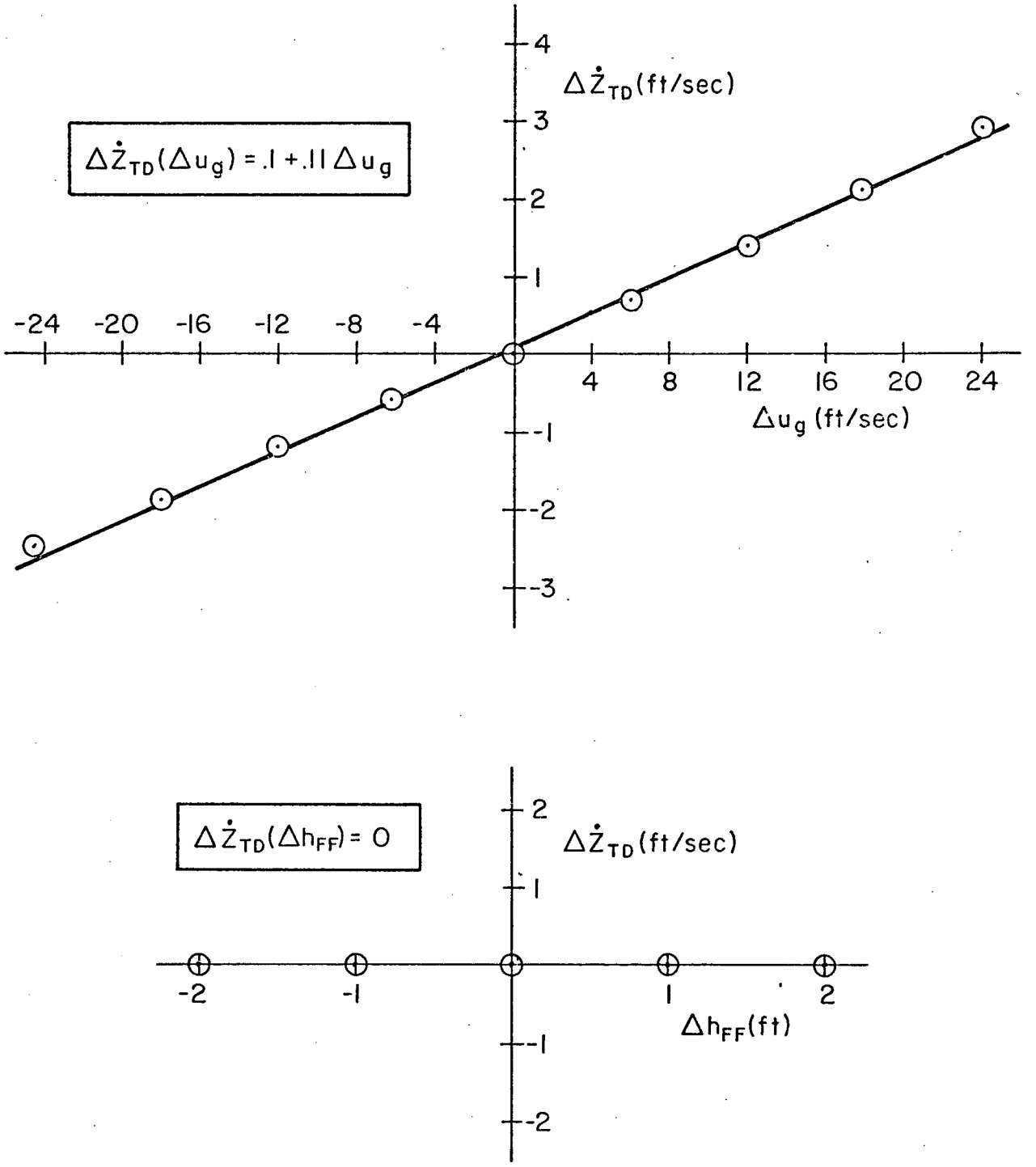

Figure 18. Mapping of Initial Conditions onto the Ground (continued)
d) $\Delta\dot{Z}_{TD}$ due to Δu_g, Δh_{FF}

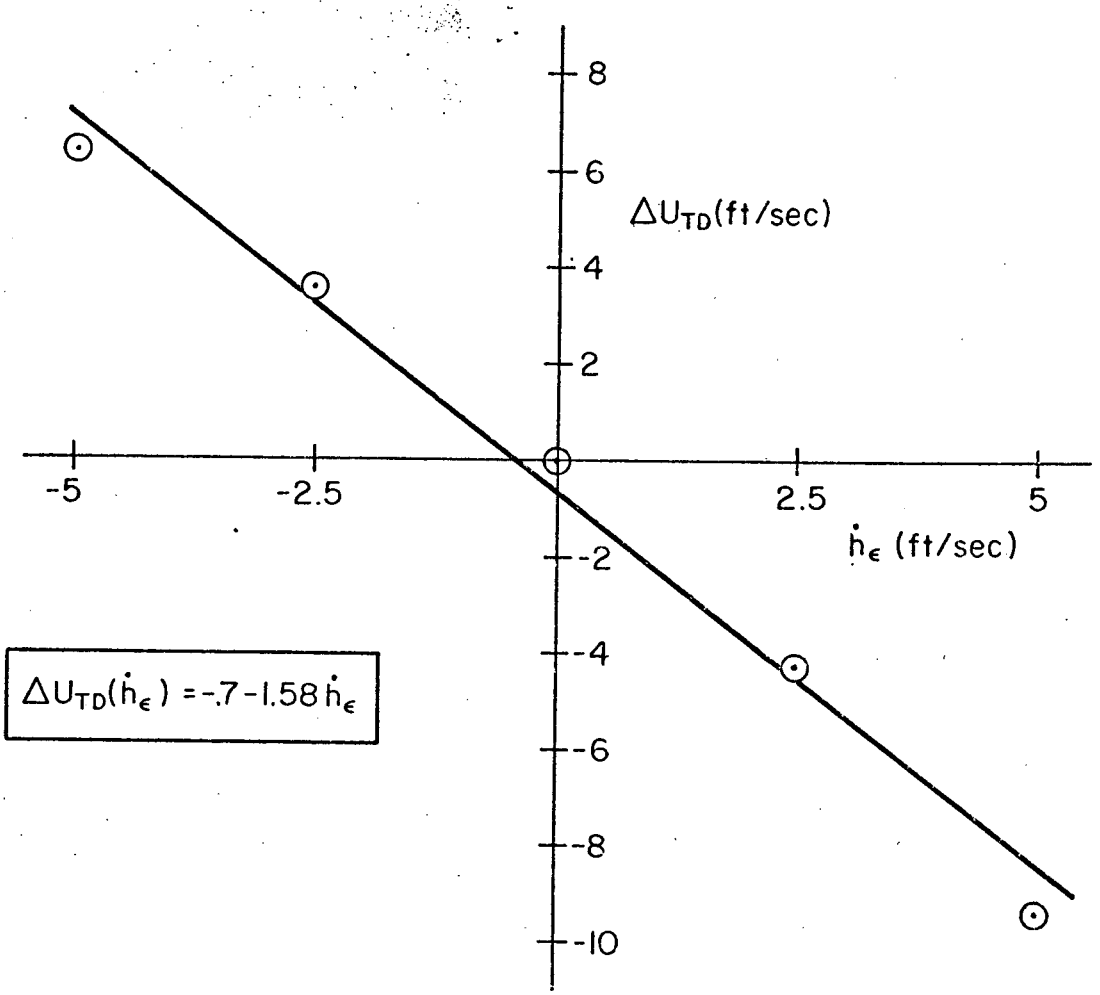

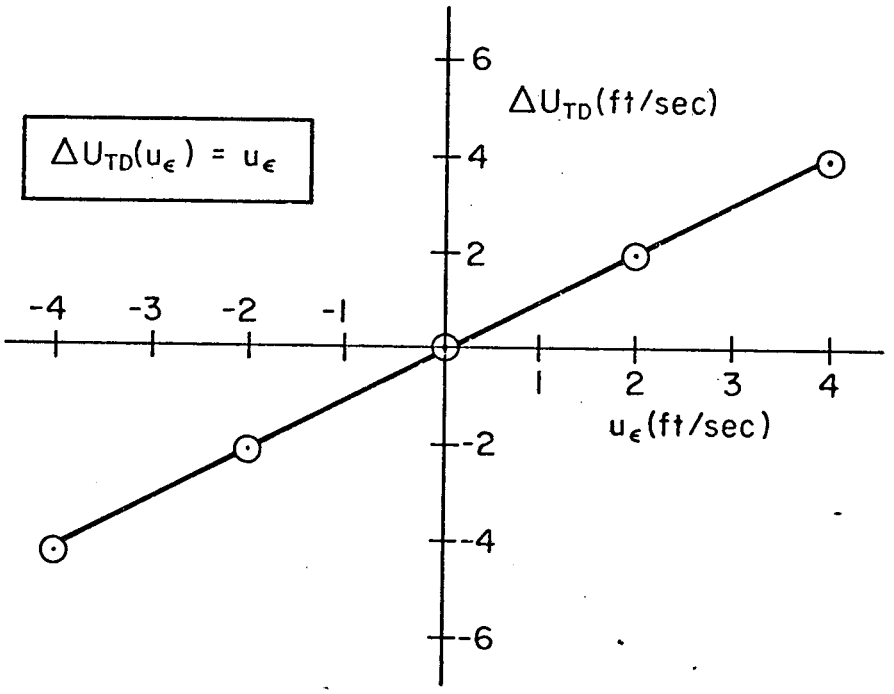

Figure 18. Mapping of Initial Conditions onto the Ground (continued)

e) ΔU_{TD} due to $\dot{h}_\epsilon$, u_ϵ

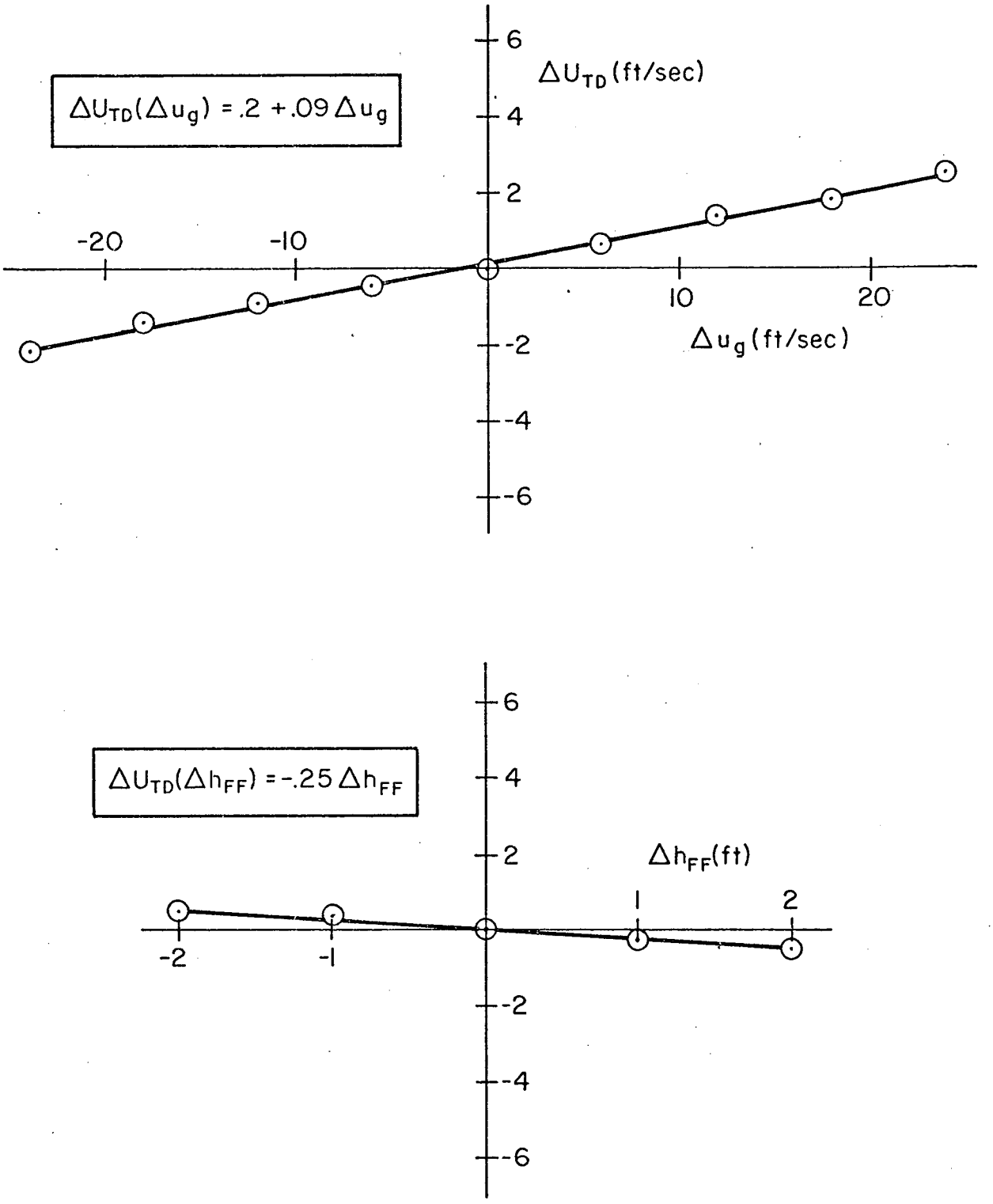

Figure 18. Mapping of Initial Conditions onto the Ground (concluded)

f) ΔU_{TD} due to Δu_g, Δh_{FF}

dispersion in the printed-out values of X_{FF} that can be up to about ±162 ft ($\doteq \pm 1/2 \times 325$). For a uniform distribution of sampling times (about the nominal), an rms X_{ERROR} of about 95 ft is thereby introduced into the distribution supplied to us. (Actual X-errors are produced by equipment imperfections, random gusts and mean wind variations, and by beam bias and noise).

In spite of this situation, we can obtain a rough estimate of the size of the measured X_{FF} dispersions by using a root-sum-square (RSS) calculation to combine the rms sampling errors with our estimate of the actual rms X_{FF} dispersions. This calculation gave us rms values of 181 ft and 167 ft, respectively, for the scanning beam and tracking radar systems, which compare very favorably with the rms values of 196 ft and 183 ft supplied to us from Bell's data.

U_{FF}

The distribution of inertial speeds just before final flare is due almost entirely to the variation in the mean wind. Thus, we can easily make an estimate of the expected distribution. According to Bell's prediction scheme (indicated in Fig. 17b and detailed in Ref. 6), the ground speed at the start of final flare is modified by an amount equal to half of the mean wind speed. Therefore, our estimate of the effect of the mean wind on U_{FF} is as shown in Fig. 19. Also shown in Fig. 19 is a combined histogram of Bell's measured distributions. As seen in the figure, the comparison is quite good.

$\dot{Z}_{FF}$

Here is another case wherein a significant contribution is due to mean winds. Our computed dispersion due to random gusts has an rms value of about 0.6 ft/sec. The effect of mean wind variations has been estimated at 0.86 ft/sec rms. (This estimate is based on the assumption that the ratio of $\sigma_{\dot{Z}_{FF}}$ to $\mu_{\dot{Z}_{FF}}$, due to mean winds, is the same as the ratio of $\sigma_{u_{wFF}}$ to $\mu_{u_{FF}}$.) The combined RSS value for these two dispersion sources is 1.05 ft/sec, which compares very favorably with the 1.15 ft/sec average for Bell's two systems.

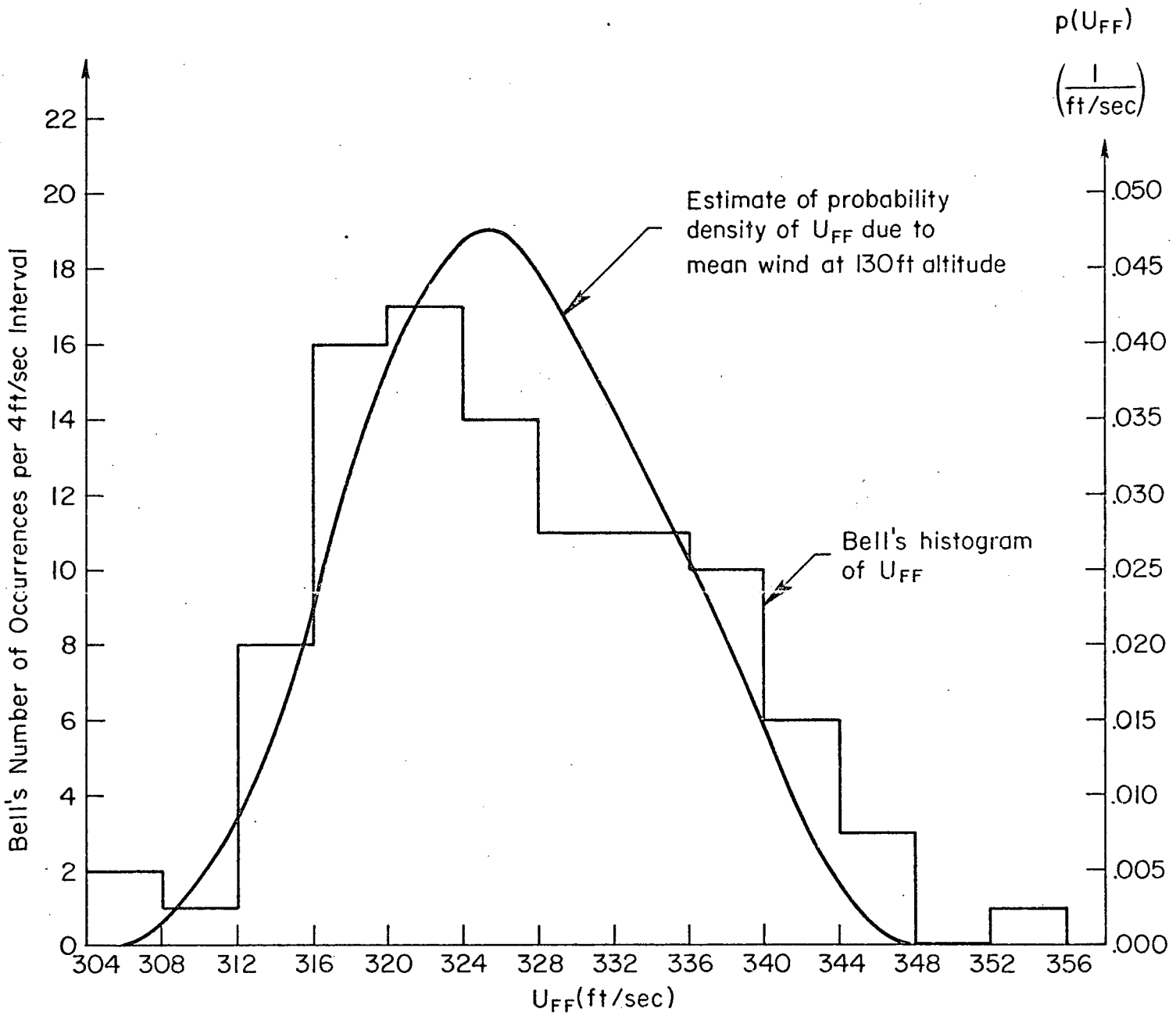

Figure 19. Comparison of Bell Distribution of Inertial Speed at Final Flare with Estimated Inertial Speed Due to Mean Wind Only

y_{FF}

A comparison of rms levels of y_{FF} can also be made by RSS'ing our separate results. For this variable the primary contribution is due to beam bias errors. Thus, separate comparisons for each guidance system are appropriate here. When the RSS calculations are made, we get 7.5 ft for an estimate of the rms y_{FF} for a scanning beam, and 4.8 ft for a tracking radar. Bell's corresponding values are 7.7 ft and 4.0 ft, respectively. Thus, a very good comparison is again obtained.

It is noted that the effects of mean winds on the lateral position (and rate) distribution(s) just prior to final flare are much less significant than they are for the longitudinal variables discussed earlier.

$\dot{y}_{FF}$

Our calculations show that the distribution of lateral position rate is relatively insignificantly affected by mean winds and equipment errors. Thus, we expect the major contribution to $\dot{y}_{FF}$ to be from random gusts. Figure 20 shows a comparison of our computed distribution of $\dot{y}_{FF}$ (due to gusts alone) with Bell's histogram of $\dot{y}_{FF}$ (due to all disturbance sources). In the figure it can be seen that the comparison is excellent, indicating that the major source of $\dot{y}_{FF}$ dispersions is indeed from random gusts.

Φ_{FF}

A comparison of Bell's and our computed bank angle distributions just before final flare was also obtained, and is shown in Fig. 21. It is seen that the comparison is again exceptionally good.

B. COMPARISONS AT DECRAB

The comparisons of lateral variables just prior to decrab are almost identical to those presented above. Therefore, we will not repeat the presentation, but rather we will go directly to the touchdown comparisons.

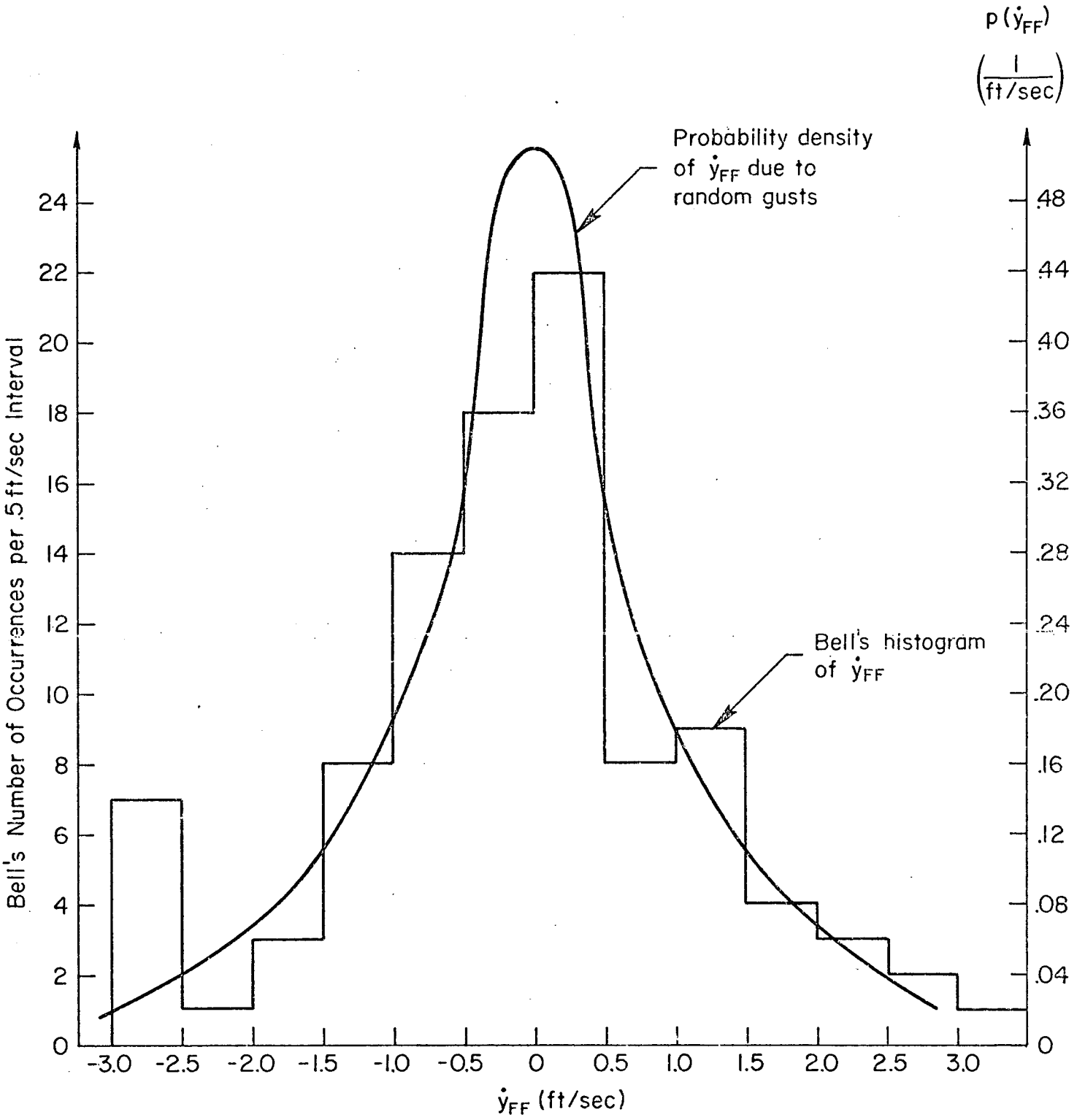

Figure 20. Comparison of Bell Distribution of $\dot{y}$ at Final Flare with Computed $\dot{y}_{FF}$ Due to Random Gusts

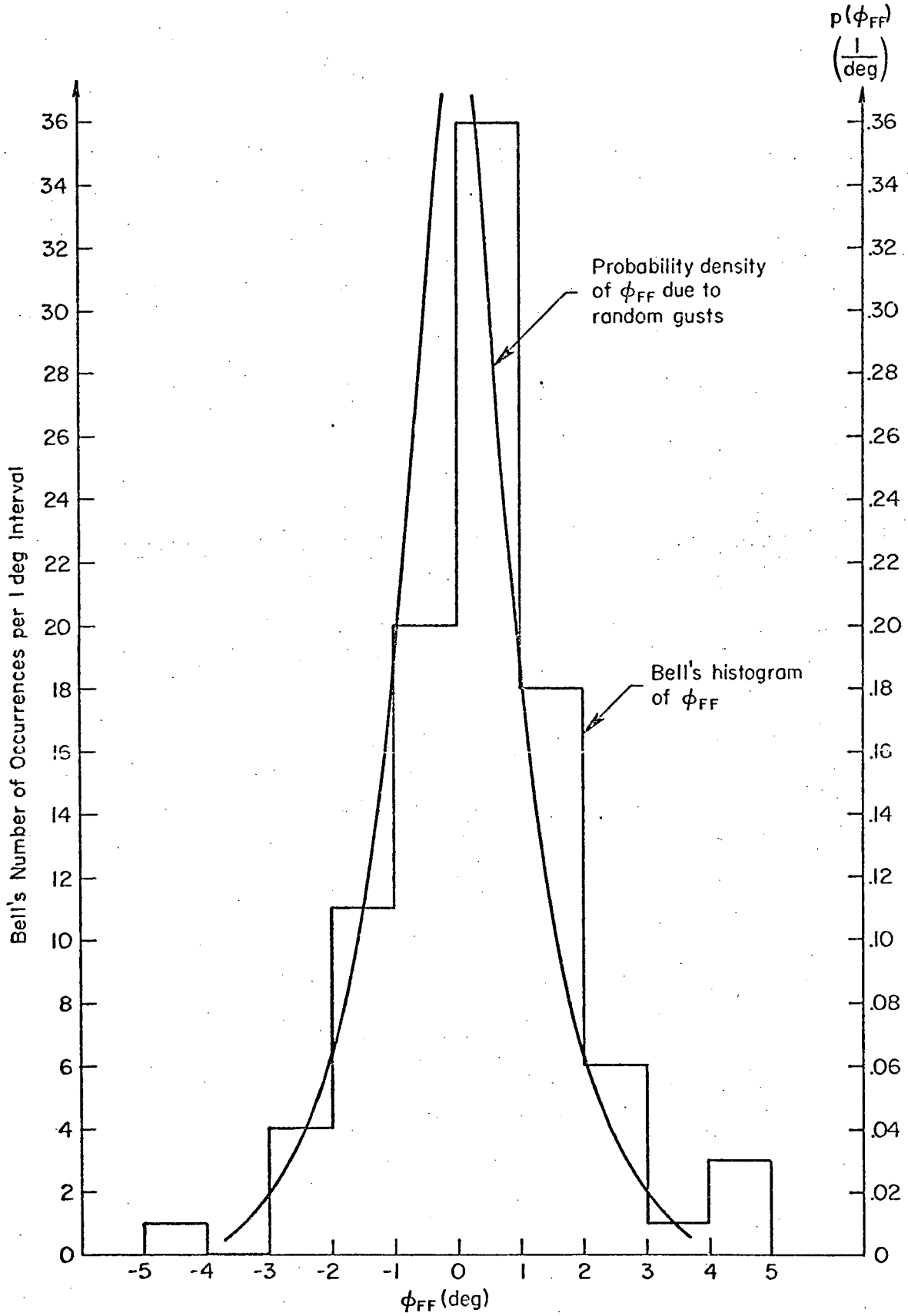

Figure 21. Comparison of Bell Distribution of φ at Final Flare with Computed φ_{FF} Due to Random Gusts

C. COMPARISONS AT TOUCHDOWN

X_{TD}

Because the scanning beam and tracking radar systems give rms touchdown dispersions that are noticeably different, we have made separate comparisons in Fig. 22, as well as a combined comparison in Fig. 23. Excellent correspondence is evident (separately and combined). Figure 24 presents a comparison of cumulative distributions of X_{TD} which indicates that the calculated distribution is the same as Bell's, except that it is shifted about 70 ft down the runway. The reason for the shift is not known at this time. However, it could be caused by any number of things, such as a difference between c.g. and glide slope antenna locations, or by an equipment bias of about 8 in. (corresponding to the change in c.g. height due to landing gear compression).

U_{TD}

The comparison of touchdown speed distributions is shown in Fig. 25. Again, excellent agreement is found between Bell's Monte Carlo results and the analytical-empirical results. As an item of interest, it is noted that the double peaking in the computed distribution is believed to be a result of the particular model used for the mean wind variations. Figure 26 shows that Bell's histogram for the scanning beam guidance system also exhibits such a characteristic.

$\dot{Z}_{TD}$

The distribution of sink rates at touchdown is the only area in which any difference was found between Bell's and the calculated results. Although this difference is small, Fig. 27 does show that Bell obtained a slightly wider distribution than we computed for sink rate at touchdown. All in all, the fit is actually pretty good, but we mention the difference because it is the only one we encountered in all of our comparisons.

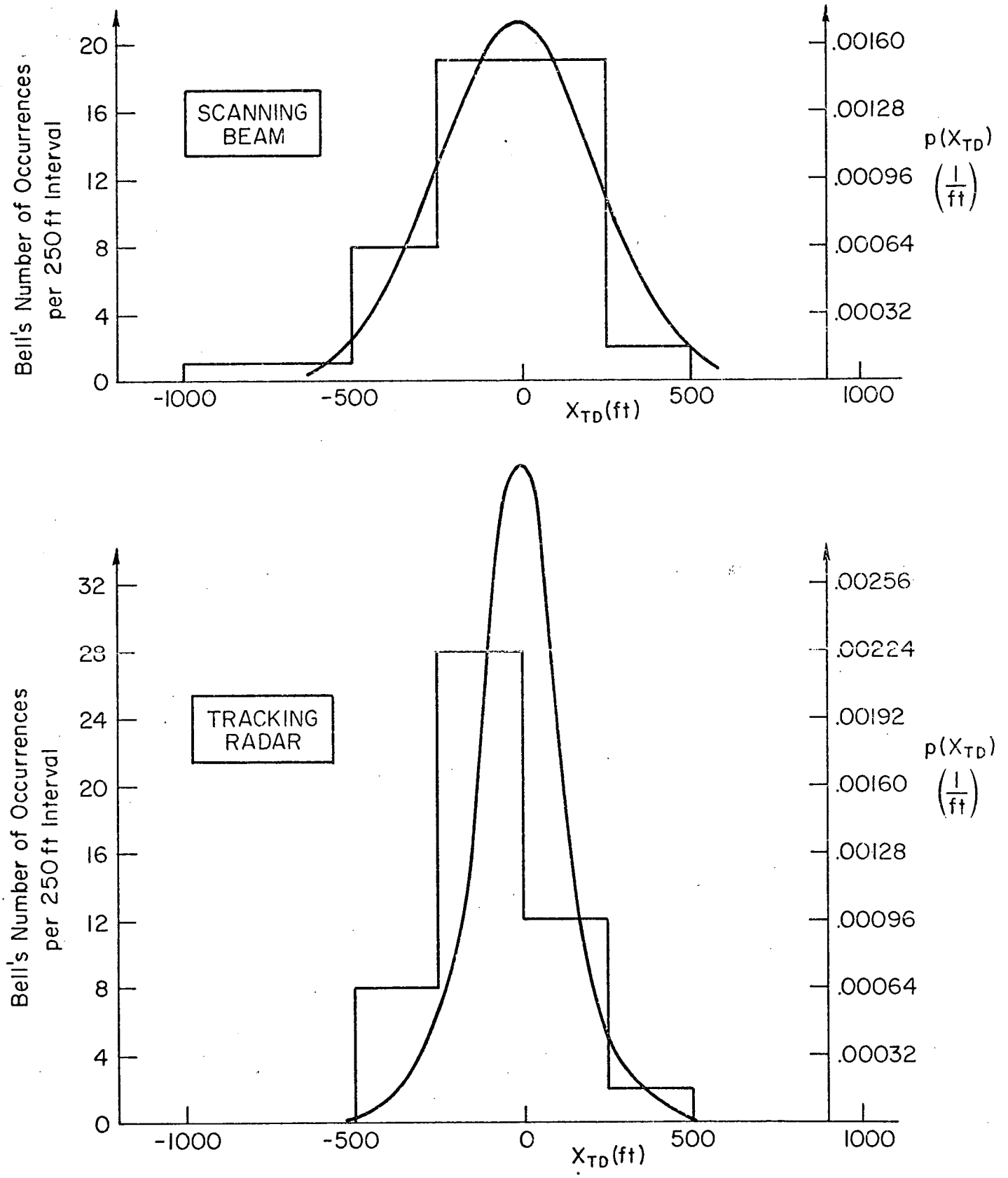

Figure 22. Comparison of Bell's Monte Carlo Generated Histograms of X_{TD} with Computed Distributions (for Two Guidance Systems)

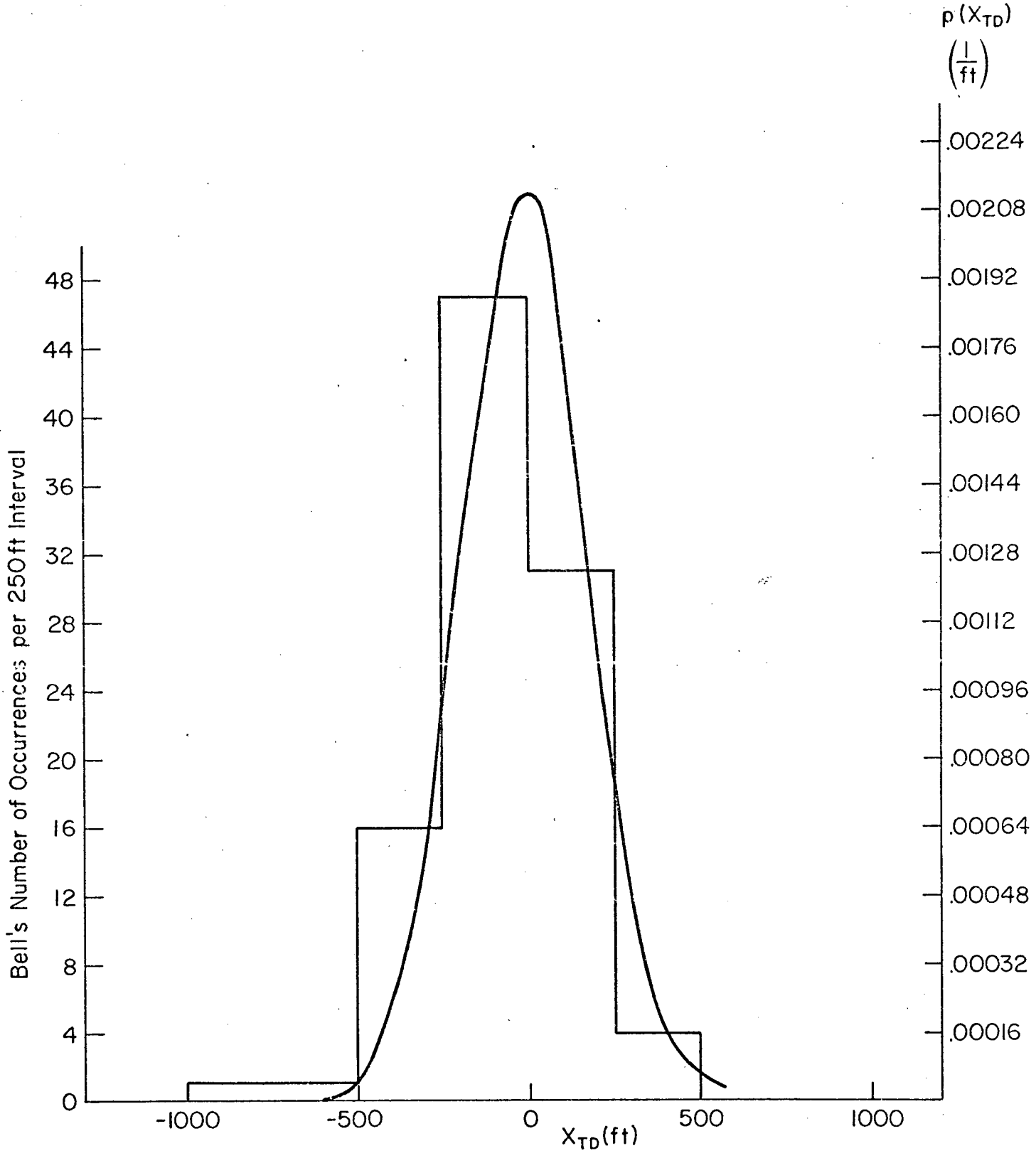

Figure 23. Comparison of Bell's Monte Carlo Generated Histogram of X_{TD} with Computed Distribution (with Data for Both Guidance Systems Combined)

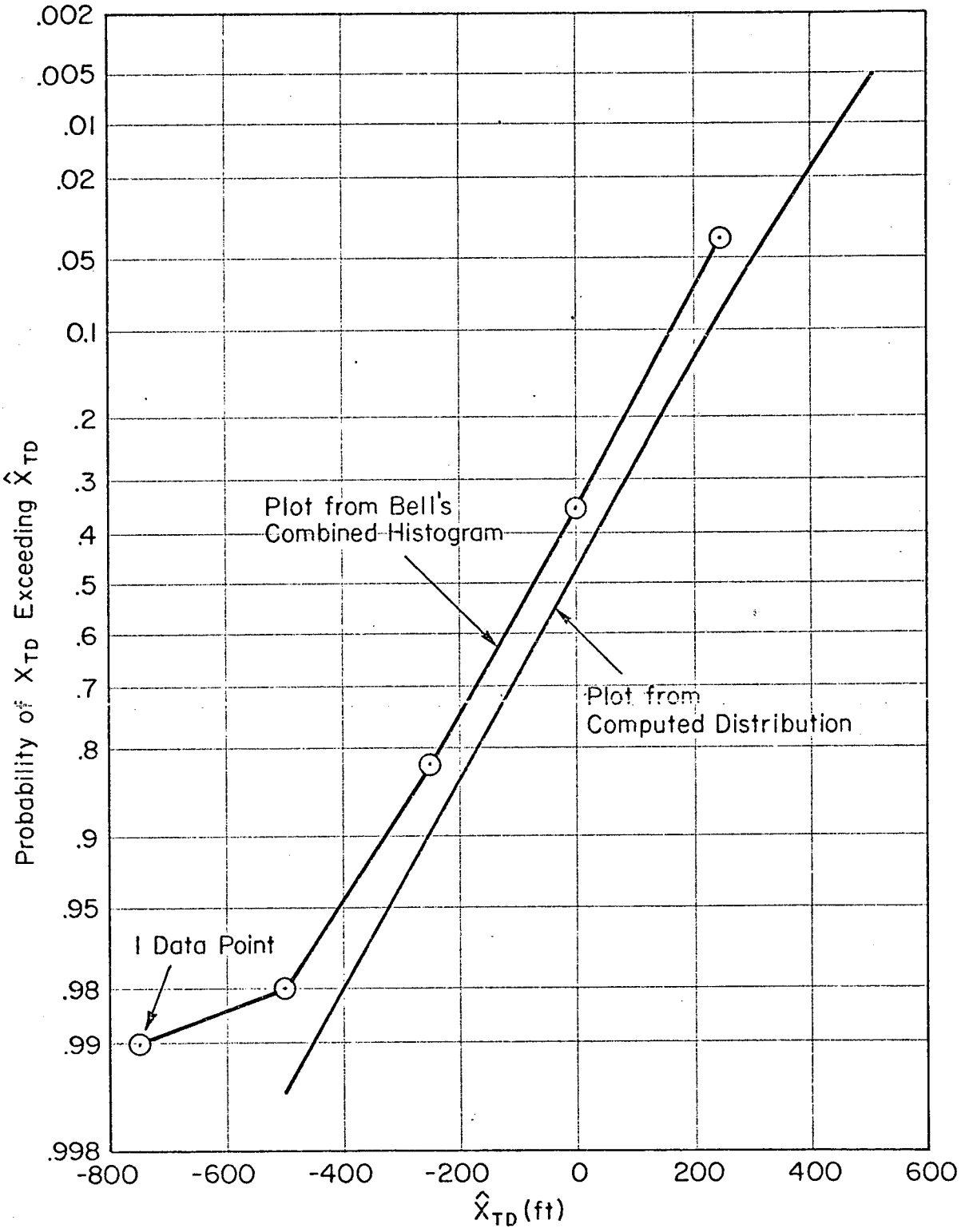

Figure 24. Comparison of Cumulative Distributions of X_{TD}

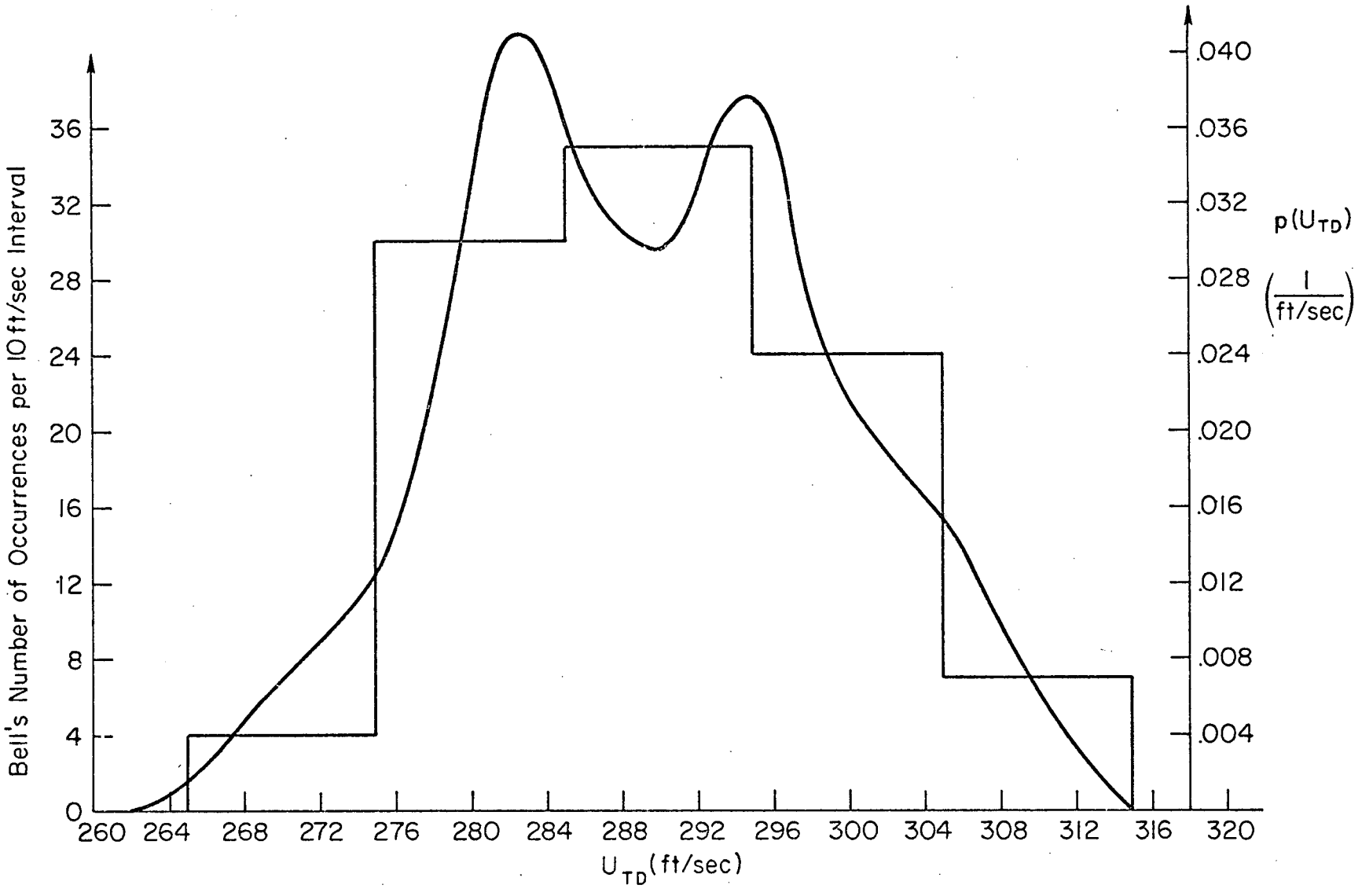

Figure 25. Comparison of Bell's Monte Carlo Generated Histogram of U_{TD} with the Computed Distribution (with Data for Both Guidance Systems Combined)

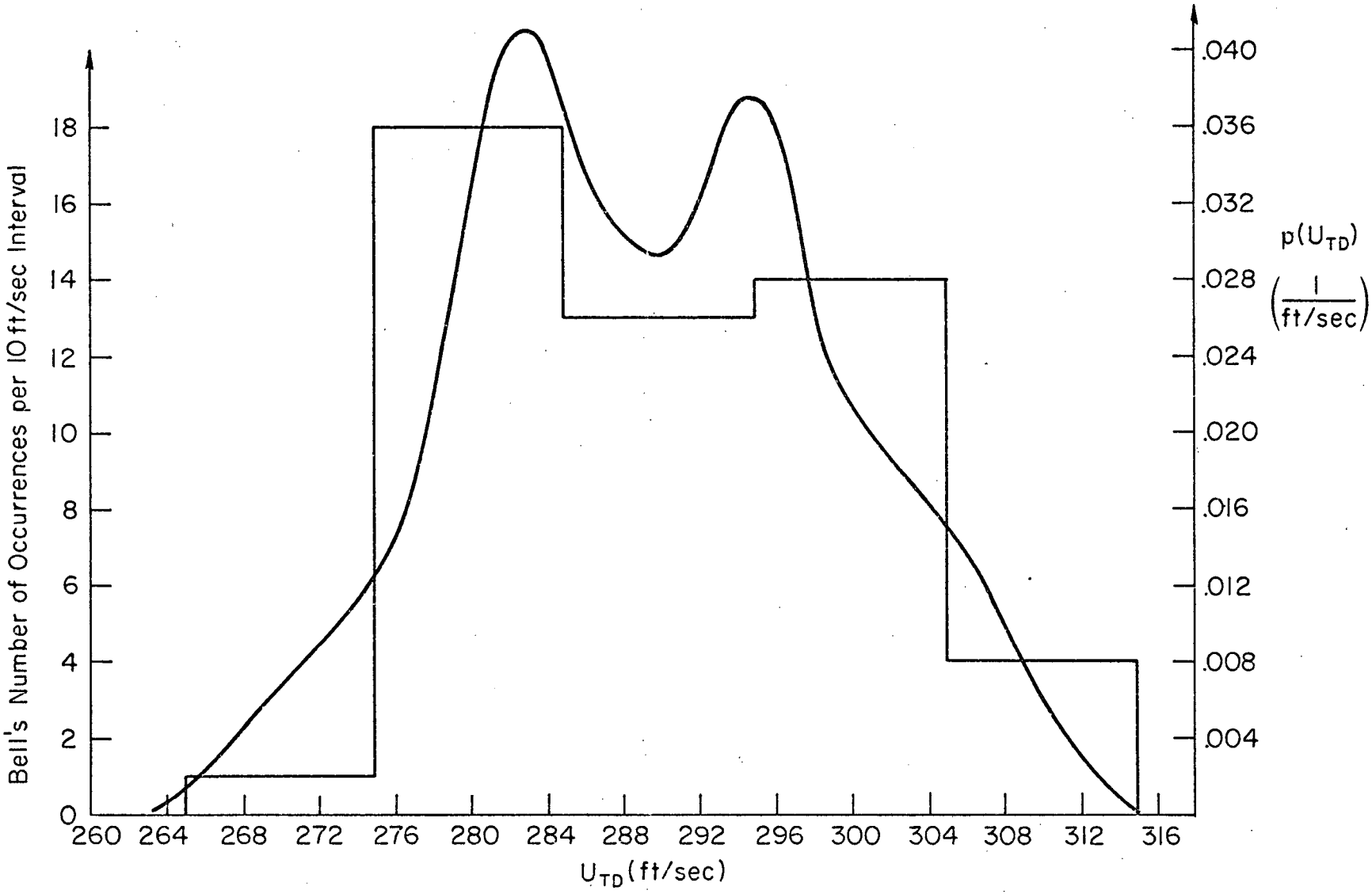

Figure 26. Comparison of Bell's Monte Carlo Generated Histogram of U_{TD} with the Computed Distribution (Using Data for Scanning Beam Guidance System)

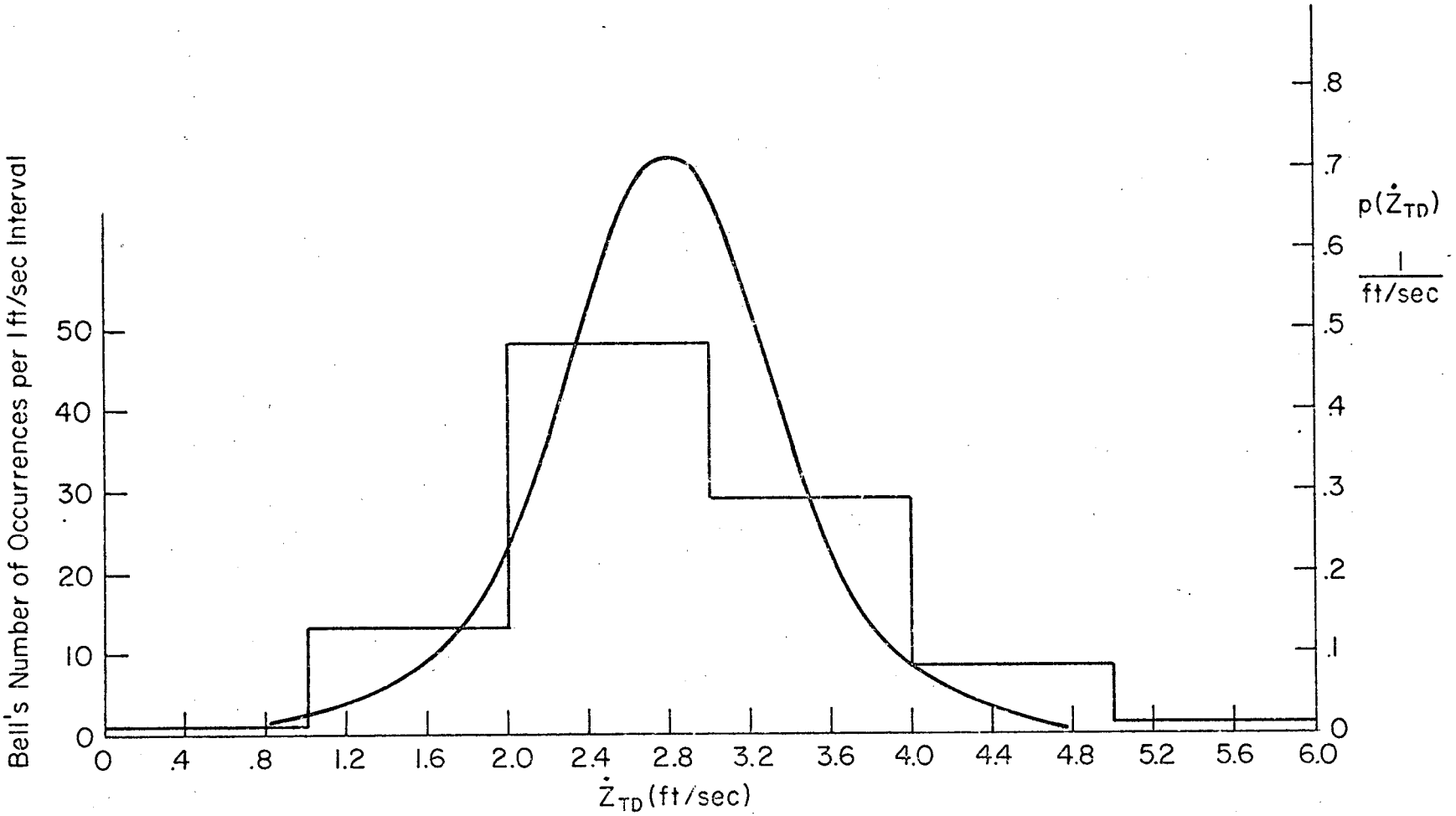

Figure 27. Comparison of Bell's Monte Carlo Generated Histogram of $\dot{Z}_{TD}$ with the Computed Distribution (with Data for Both Guidance Systems Combined)

y_{TD} and $\dot{y}_{TD}$

For large crosswinds, Bell's decrab system causes the vehicle to finish its alignment maneuver several seconds prior to touchdown. This leads to rather large drift rates and lateral offsets at touchdown, as evidenced in Bell's touchdown distributions. However, our original model was not designed to include such long decrab times. Therefore, a modification to the model would be required to cover this unanticipated situation. But, considering the tradeoffs involved in making the required changes, it was decided not to expend the effort to modify our calculation technique to cover this situation. As a result, we did not compute touchdown distributions of y and $\dot{y}$ to compare with Bell's histograms. The very good matchings at final flare and decrab were considered adequate validations of computations of distributions for these variables.

φ_{TD}

With Bell's control system, φ_{TD} is not sensitive to the above mentioned drift situation that develops after decrabbing in a large crosswind. Therefore, we were able to obtain a meaningful comparison of bank angle distributions at touchdown. This comparison is shown in Fig. 28, where another excellent match is evident.

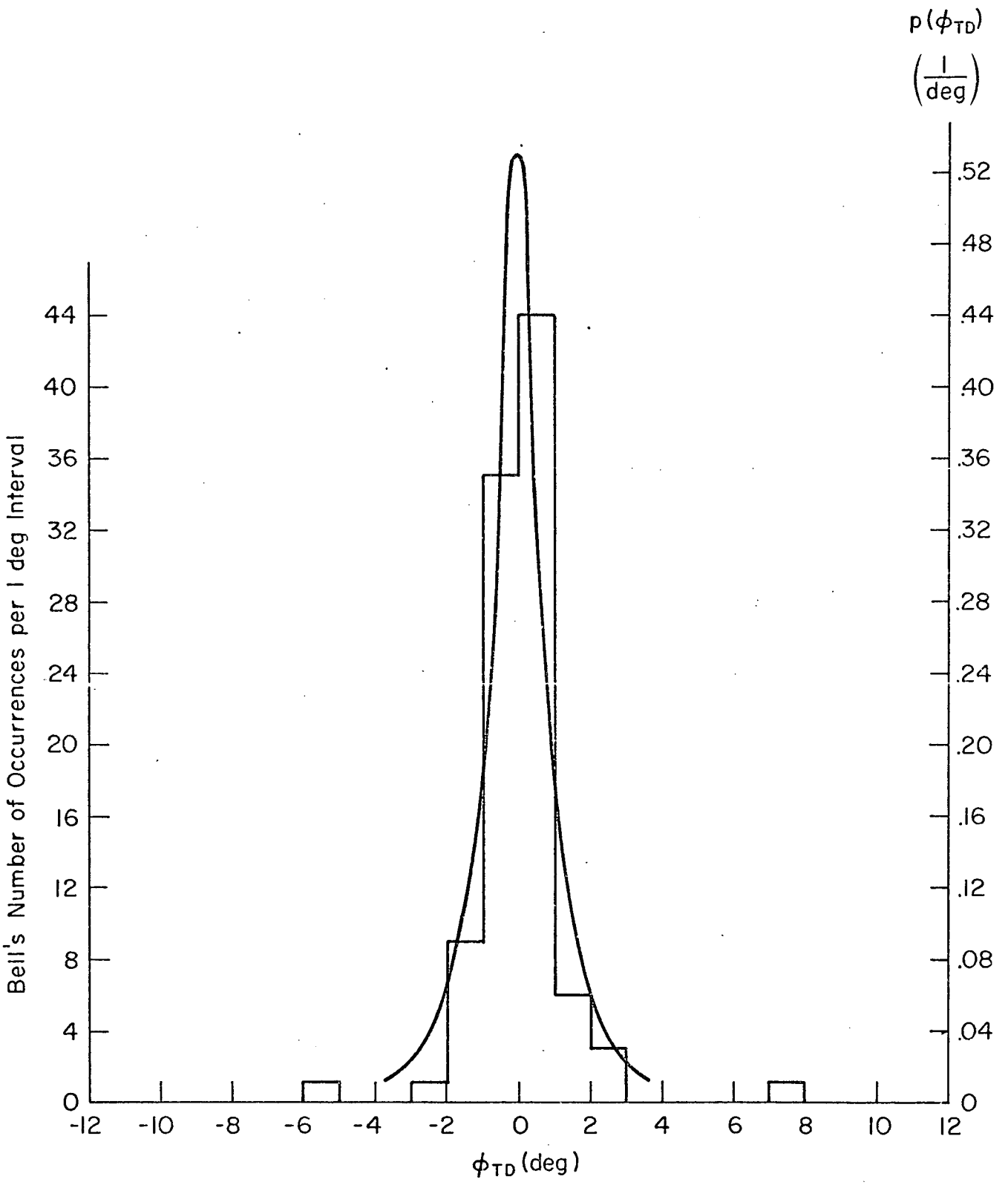

Figure 28. Comparison of Bell's Monte Carlo Generated Histogram of φ_{TD} with the Computed Distribution (with Data for Both Guidance Systems Combined)

SECTION V

CONCLUSIONS AND COMMENTS

A. CONCLUSIONS

The computed probability distributions were found to be extremely good fits to Bell's Monte Carlo generated histograms for pertinent longitudinal and lateral variables at two "points" along the vehicle's final approach trajectory. This validates the assumption that the longitudinal and lateral situations can be analyzed separately. As a further consequence of this good matching of results, it is apparent that (for the situation considered) the approximation technique has been validated as an alternative to a Monte Carlo simulation for obtaining distributions of pertinent variables through final approach and touchdown. However, due to the limited number of Monte Carlo runs available, this validation does not cover the extreme tails of the (computed) distributions. A significantly greater number of Monte Carlo runs would be required to validate computed points in the extreme tails of the distribution. However, as a practical matter, the analysis technique is most useful as a design tool in the region that has been validated. Besides, the extreme tails of any "real" distribution are governed by factors that are not amenable to accurate representation anyway — either due to unknown inputs or to unknown extreme details of the distributions of known inputs.

B. COMMENTS

The principal advantage of the system model over a Monte Carlo alternative is its inherent flexibility. A Monte Carlo simulation will provide probability distributions, but system sensitivities are <u>not</u> direct outputs of such a simulation. If some aspect of the overall situation is modified, then a repeat of all the Monte Carlo runs is required to determine the effect of the modification. This is not only expensive, but it also fails to provide any insight into the fundamental interactions and tradeoffs that are present within any system. Such is not the case with the analysis technique and associated approach and landing system model. Touchdown sensitivities are an intermediate calculation to the estimated touchdown distributions. As a

consequence, the model, as used, is a highly practical analysis tool which obviates the need for a more expensive Monte Carlo simulation, previously required to obtain distributions or exceedance probabilities.

It is pertinent to note here that several of the more detailed aspects of the analysis technique were not described in this report. Some of these aspects were omitted because they entail more or less standard mathematical procedures. Others were omitted because they were not used in the example applications presented. It is felt that some of these aspects deserve mention, if only to point out their existence. One area wherein several detailed facets of the analysis technique were omitted involves an appropriate representation of effects of random gusts after the start of flare. For example, it is possible to compute (and make use of) a time-varying rms value for dispersions during flare. Another point concerns the choice of flight path angle to be used in calculating the X_{TD} sensitivity to h_ϵ at the start of flare. For low flare heights this isn't a critical matter. But for the higher flare heights (usually associated with one-step flares) the appropriate flight path angle appears to be that attained about 5 sec prior to touchdown, rather than that during equilibrium glide. In addition, there are probably other detailed considerations where specific applications might require modification of the specific procedures presented here.

REFERENCES

1. Johnson, Walter A., and Duane T. McRuer, Development of a Category II Approach System Model, Systems Technology, Inc., Tech. Rept. No. 182-2, Oct. 1970 (forthcoming NASA CR-2022).

2. Wind Model for Space Shuttle Simulations, NASA Ames Research Center, circa 1970.

3. Neuman, Frank, and John D. Foster, Investigation of a Digital Automatic Aircraft Landing System in Turbulence, NASA TN D-6066, Oct. 1970.

4. McRuer, Duane, Irving Ashkenas, and Dunstan Graham, Aircraft Dynamics and Automatic Control, Princeton University Press, 1972.

5. Aero Data Book for High Cross Range 134C Configuration, North American Rockwell.

6. Cockayne, William, and Walter Rusnak, Study of Automatic Flare and Decrab Guidance and Control System for the Space Shuttle Vehicle, NASA CR-114436.

APPENDIX

GUST INPUT TRANSFER FUNCTIONS JUST PRIOR TO FLARE (ONE-STEP FLARE)*

$$\frac{u}{u_g} = \frac{.0206(.0972)(1.140)(14.73)[.847,\ .206][.715,\ 1.131][.751,\ 4.32]}{(.0311)(.1039)(.1493)(.458)(1.295)(14.10)[.523,\ .928][.943,\ 3.91]}$$

$$\frac{u}{w_g} = \frac{.00148(.993)(7.91)(-846.)[.999,\ .1054][-.0986,\ .726][.921,\ 1.398]}{\text{same denominator}}$$

$$\frac{h}{u_g} = \frac{-.1278(0)(.0361)(.0771)(.925)(2.00)(14.69)[.724,\ 3.79]}{\text{same denominator}}$$

$$\frac{h}{w_g} = \frac{-1.262(0)(.0292)(.1026)(1.060)(2.00)(10.92)[.453,\ 3.08]}{\text{same denominator}}$$

$$\frac{\dot{z}}{(\ )_g} = \frac{sh}{(\ )_g}$$

---

*The notation used here is defined as follows:

$$\frac{K(s + a)}{(s + b)[s^2 + 2\zeta\omega s + \omega^2]} \text{ becomes } \frac{K(a)}{(b)[\zeta,\ \omega]}$$